THE DARKSIDE-50 EXPERIMENT: ELECTRON RECOIL CALIBRATIONS AND A GLOBAL ENERGY VARIABLE

A DISSERTATION SUBMITTED TO THE GRADUATE DIVISION OF THE
UNIVERSITY OF HAWAIʻI AT MĀNOA IN PARTIAL FULFILLMENT
OF THE REQUIREMENTS FOR THE DEGREE OF

DOCTOR OF PHILOSOPHY

IN

PHYSICS

DECEMBER 2017

By

Brianne R. Hackett

Dissertation Committee:

Jelena Maricic, Chairperson
John Learned
Jason Kumar
Sven Vahsen
Joshua Barnes

Keywords: dissertations, dark matter, DarkSide-50, calibrations, energy variable

To my family:

to my friends, Erin and Katherine, you are my sisters,

to Jesse, my big little brother, for always making me laugh,

to my sister, Shanna, for being there no matter what and encouraging me through everything,

to my mom, I love you,

and to my daddy, you are my hero and I miss you more than I could ever say.

ACKNOWLEDGMENTS

ABSTRACT

Over the course of decades, there has been mounting astronomical evidence for non-baryonic dark matter, yet its precise nature remains elusive. A favored candidate for dark matter is the Weakly Interacting Massive Particle (WIMP) which arises naturally out of extensions to the Standard Model. WIMPs are expected to occasionally interact with particles of normal matter through nuclear recoils. DarkSide-50 aims to detect this type of particle through the use of a two-phase liquid argon time projection chamber. To make a claim of discovery, an accurate understanding of the background and WIMP search region is imperative. Knowledge of the backgrounds is done through extensive studies of DarkSide-50's response to electron and nuclear recoils.

The CALibration Insertion System (CALIS) was designed and built for the purpose of introducing radioactive sources into or near the detector in a joint effort between Fermi National Laboratory (FNAL) and the University of Hawai'i at Mānoa. This work describes the testing, installation, and commissioning of CALIS at the Laboratori Nazionali del Gran Sasso. CALIS has been used in multiple calibration campaigns with both neutron and γ sources. In this work, DarkSide-50's response to electron recoils, which are important for background estimations, was studied through the use of γ calibration sources by constructing a global energy variable which takes into account the anti-correlation between scintillation and ionization signals produced by interactions in the liquid argon. Accurately reconstructing the event energy correlates directly with quantitatively understanding the WIMP sensitivity in DarkSide-50.

This work also validates the theoretically predicted β decay spectrum of ^{39}Ar against ^{39}Ar β decay data collected in the early days of DarkSide-50 while it was filled with atmospheric argon; a validation of this type is not readily found in the literature. Finally, we show how well the constructed energy variable can predict energy spectra for the calibration sources and for ^{39}Ar.

TABLE OF CONTENTS

LIST OF TABLES

LIST OF FIGURES

CHAPTER 1
DARK MATTER

1.1 Evidence for Dark Matter

The genesis of the search for dark matter began decades ago with the first observational evidence in the 1930s. The exact nature of this non-radiative, gravitationally interacting dark matter is yet to be known even with the accumulation of astronomical and observational evidence. The discovery/detection of dark matter has become the ultimate prize for high energy physicists with many technologies employed in the search. In this chapter, the evidence for dark matter at galactic and cosmological scales will be discussed.

1.1.1 Galaxy Clusters

The term dark matter was first coined in 1933 by Fritz Zwicky, an astrophysicist from the California Institute of Technology. Zwicky studied the velocities of galaxies within several galaxy clusters. Of note is the Coma cluster for which he studied its dispersion of velocities. Under the assumption that the Coma Cluster has reached a stationary state and using the galaxy velocities, Zwicky applied the virial theorem

$$\bar{T} = -\frac{1}{2}\bar{V}$$

to the cluster. The virial theorem relates the average kinetic energy of bodies within a system that are gravitationally bound to the average gravitational potential energy of the system. The gravitational potential energy is a function of the mass of the system and by utilizing the virial theorem one can estimate the total mass of the galaxy cluster. Zwicky found that to obtain the average velocity found in the Coma Cluster, the mass would have to be 400 times greater than what was measured from visible matter [1].

1.1.2 Gravitational Lensing

In general relativity, massive objects curve spacetime in their vicinity, which changes the path of photons as they move in this space. When massive bodies are located in the line of sight of more distant star and galaxies, the images of these background stars become distorted. The effect, known as gravitational lensing, has three types. The most extreme type is called strong lensing. In this case, the body bending the light is very massive and the background source of light is close to the massive body, producing the most apparent effect, creating multiple images of the background source. Weak lensing, the second type, is not strong enough to produce multiple images. Instead, the source is distorted, seen as though stretched and magnified at the level of a few percent. The

third type of gravitational lensing is microlensing whereby the temporary, apparent brightening of the background source is seen as a foreground body passes in front. Of the three types of gravitational lensing, weak lensing has been the most useful in terms of dark matter evidence.

Figure 1.1: A composite image of the Bullet Cluster; the hot x-ray emitting gas is shown in pink and the regions of highest mass concentration are shown in blue. Image Credit: X-ray: NASA/CXC/CfA/M.Markevitch et al.; Lensing Map: NASA/STScI; ESO WFI; Magellan/U.Arizona/D.Clowe et al.; Optical: NASA/STScI; Magellan/U.Arizona/D.Clowe et al.

The most famous example of weak lensing is the Bullet Cluster. This cluster is the result of a merger of sub-clusters. The stars of the galaxies, seen in visible light, were gravitationally slowed but otherwise remained undisturbed during the merger, simply passing through. The hot gases of the colliding clusters, seen in X-rays, interact electromagnetically; they represent most of the ordinary (baryonic) matter in the merger. There is a third component to the composite Bullet Cluster image (Fig. 1.1) which represents the location of the bulk of the matter in the clusters as revealed by gravitational lensing. Gravitational lensing shows that the center of mass is near the visible galaxies, not coincident with the location of the ordinary matter (i.e. the hot gases). This supports the idea of the majority of the matter in the cluster pair is in the form of dark matter – dark matter that passed through the collision without interacting and is non-radiative. Its existence is seen by its effect on the spacetime around it [2].

1.1.3 Rotational Curves

In the 1970s and early 1980s, Vera Rubin and Ken Ford were the first to show conclusive evidence that there is non-luminous matter at large radii from the centers of galaxies. Galaxy rotation curves demonstrate the velocity of stars and gas as they rotate as a function of radial distance from the galactic center. By using the Doppler shift of spectral lines, one can construct the rotation curves. The 21-cm line from hydrogen is used most often as hydrogen extends much farther out radially than does the visible stellar disk, allowing for galactic orbital velocity measurements beyond the radius of visible stars. From Newtonian mechanics one can write the orbital speed of a body by

$$v(r) = \sqrt{\frac{GM(r)}{r}}$$

where M is the mass contained within the radius r. For luminous matter, one expects the velocity to fall off with increasing radius as $1/\sqrt{r}$, as seen with planets in a solar system. However, rotational curves of typical galaxies are shown to slowly rise or to flatten out as the radius increases. This implies that the mass of the galaxy increases linearly with radius, M(r) $\propto$ r [3][4]. Before Rubin and Ford, similar measurements were made but did not cite non-luminous matter as the cause [5].

1.1.4 The Cosmos

The results showing the presence of unseen matter from galactic rotation curves and gravitational lensing, while substantial, are not enough to make a convincing argument for the existence of an as yet undetermined new type of matter. It could be argued that this unseen matter is simply large numbers of asteroids, planets, stellar remnants that do not emit enough (if any) light to be observed and these objects are dispersed enough to have negligible interactions in cluster collisions. There have been extensive searches of MACHOs, but with no positive evidence. Therefore, one must look to other evidentiary parameters. At the cosmological scale there have been multiple supporting measurements which demonstrate that this non-luminous matter is, indeed, of a new type.

Big Bang Nucleosynthesis

Big Bang Nucleosynthesis (BBN) describes the production of the lightest elements (D, ^{3}He, ^{4}He, ^{7}Li) from hydrogen from $\sim$ 10 seconds to 20 minutes after the Big Bang. BBN, therefore, provides us with a measure of the amount of baryonic matter in the universe. After about 20 minutes, the universe was no longer in a hot, dense state, it had cooled and expanded to the point that nuclear fusion had stopped leaving behind the elements which would form the earliest stars [6]. The abundances of the lightest elements at this point in the formation of the universe depend on the baryon to photon ratio of which D/H is the most informative. The deuterium that is produced in stars is converted to ^{4}He as is any deuterium used in the process of stellar formation. Any deuterium not accounted for from stars/stellar production is thus from the time of BBN and can

be used as a lower limit on its original abundance. From the ratio of D to H in far distant regions, before there could have been substantial conversion of D to ^{4}He, one can get a measure of the baryon density [7]

$$\Omega_b h^2 = 0.02202 \pm 0.00046$$

giving a mass-energy density for baryonic matter of less than 5%.

The Cosmic Microwave Background

When the universe was 380,000 years old, photons began to move freely for the first time. Prior to that time, the universe was too hot and dense for electrons to combine with the existing baryonic elements; photons would scatter easily off free electrons creating an environment that is opaque to radiation. Then as the universe cooled and expanded, the free electrons combined with nuclei to form neutral hydrogen and the universe became transparent to radiation – the photons interact very weakly with neutral hydrogen allowing them to travel along a straight path. The CMB is known as "the surface of last scattering" since it was at that time (380,000 years after the Big Bang) that the CMB photons directly scattered off matter.

The CMB has an average temperature of 2.725 K; variations in the temperature (seen in Fig. 1.2) occur at the level of 10^{-4}. These anisotropies give a look into the early universe as they represent differences in the densities of structure at that time. At the largest scales, areas of higher density are seen as slightly cooler regions in the CMB, the photons lost energy in escaping from the larger gravitational potentials. On smaller scales, local overdense regions would cause the baryon-photon plasma to be compressed. This compression would increase the pressure until it forced the region to expand. In expanding, the pressure would then decrease until the gravitational attraction would cause the region to collapse inward. These fluctuations, known as Baryonic Acoustic Oscillations can be used to determine the relative abundance of baryons. The results

$$\Omega_b h^2 = 0.02226 \pm 0.00023$$

agree with those from BBN [8]. From BBN and the CMB, baryonic matter only accounts for less than 5% of the mass-energy of the universe while the fraction of total matter in the universe is 30%

$$\Omega_m = 0.308 \pm 0.012$$

Therefore, the universe is made up of more than a quarter by matter that is non-baryonic.
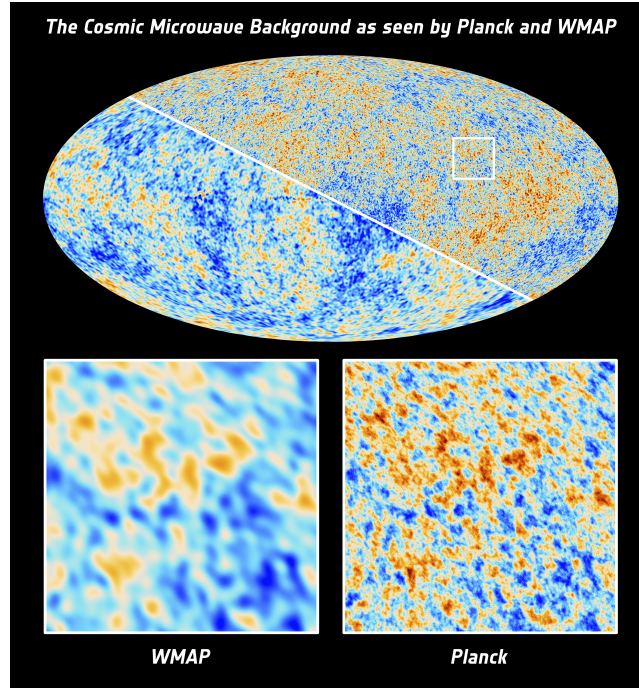
Figure 1.2: The CMB as seen by Planck and WMAP. Image credit: ESA and the Planck Collaboration; NASA/WMAP Science Team.

1.2 WIMP Dark Matter

The previous sections described evidence for the existence of a new type of matter; matter that is non-baryonic and yet makes up a quarter of the matter in the universe. It is pertinent then to begin this section with a list of properties that dark matter must possess:

- Interact gravitationally

- Electrically neutral

- Non-relativistic

- Stable

One of the more attractive models is one that includes weak scale interactions which arises from the fact that at a time in the universe when it was still hot and dense, these non-Standard Model particles would have been in thermal equilibrium. They would annihilate with each other to form lighter particles and be created through the energy of particle annihilation. At some point, as the universe cooled and expanded, there would not be enough energy for the massive dark matter particles to form leaving their number density to fall off exponentially. As time moved on, these

annihilations would effectively cease altogether leaving their relic abundance roughly the same as it is today. The relic density, dependent on the dark matter annihilation cross section, is given by:

$$\Omega_\chi \propto \frac{1}{\langle \sigma(\chi\chi \to qq)v \rangle}.$$

When $\Omega_\chi \sim 1$, the cross section is on the order of the weak nuclear force, hence the addition of weak scale interactions to the list of dark matter properties.

WIMPs (Weakly Interacting Massive Particles) are a well motivated candidate for dark matter. They arise naturally from certain extensions of the Standard Model. WIMPs are a favored candidate because they were hypothesized independently from dark matter theory and yet have all the requisite properties of dark matter. This coincidence is referred to as the "WIMP miracle".

1.2.1 Detection Methods

Dark matter has been observed through its gravitational effects at astronomical and cosmological scales. However, to detect dark matter here on Earth in a laboratory setting, we must look to different detection methods. Fig. 1.3 presents a summary of the different types of interactions one can look for in a laboratory.
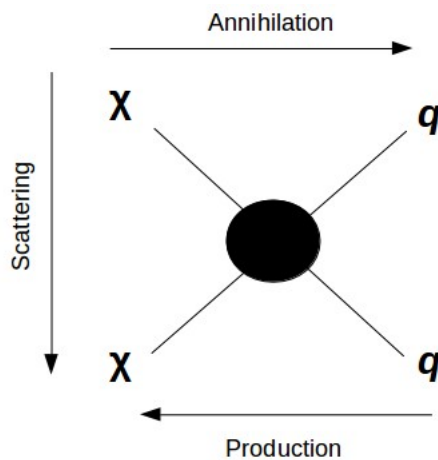
Figure 1.3: Summary of the detection methods of dark matter, χ, through its interactions with Standard Model particles, q.

Moving from left to right is annihilation where two dark matter particles, χ, annihilate with each other to form Standard Model particles, q. With dark matter annihilation, one can detect it by observing the annihilation products which include high energy photons and anti-matter particles, such as positrons and anti-protons. Indirect detection, as the signal for dark matter annihilation is known, would be seen as an excess of these types of particles. The searches for dark matter using indirect detection focus on regions where dark matter is concentrated such as the Milky Way

galactic center, the interior of the Sun, and the Earth's core [9][10].

In the figure (1.3), from right to left, two Standard Model particles will interact to produce dark matter particles. The production of dark matter can occur at particle colliders such as the LHC. Their presence would be seen as missing momentum since it will not be possible to detect dark matter particles themselves [11][10].

Finally, moving from top to bottom (in Fig. 1.3), one can directly detect dark matter by observing the elastic scattering of the dark matter particle off the nucleus of an atom (of Standard Model type). The next section will discuss the method of detection by scattering in more detail.

1.3 Direct Detection

1.3.1 WIMP Signal

From kinematics, one can write the nuclear recoil energy from the elastic scattering of WIMPs as

$$E_R = \frac{\mu^2 v^2}{m_N}(1 - \cos\theta) \tag{1.1}$$

where μ is the reduced mass of the WIMP-nucleas system ($\mu = \frac{m_N m_\chi}{m_N + m_\chi}$) and θ is the scattering angle in the center of mass frame. Following from [12] the differential scattering rate is

$$\frac{dR}{dE_R} = N_T \frac{\rho_{dm}}{m_\chi} \int_{v_{min}}^{v_{max}} d\vec{v} f(\vec{v}) v \frac{\sigma}{E_R} \tag{1.2}$$

where ρ_{dm} is the dark matter density in the galactic halo, N_T is the number of target nuclei, v and f($\vec{v}$) are the WIMP velocity and velocity distribution function, respectively. The WIMP-nucleus differential cross section is $d\sigma/dE_R$ and the WIMP mass, m_χ, are experimental observables while the other variables are input parameters derived from astronomical models. The minimum velocity, v_{min} encapsulates the detection threshold energy of the detector while v_{max} is the escape velocity in the Earth frame, taken to be 544 km/s [13].

In this scenario, $d\sigma/dE_R$ is split into two components: (1) a spin-independent coupling between the WIMP and the nucleus and (2) an effective coupling between the WIMP's spin and the total angular momentum of the nucleus:

$$\frac{\sigma}{dE_R} \propto \sigma_{SI}^0 F_{SI}^2(E_R) + \sigma_{SD}^0 F_{SD}^2(E_R) \tag{1.3}$$

where $\sigma_{SI,SD}^0$ denote the spin-independent (SI) and spin-dependent (SD) cross sections in the limit of zero momentum transfer and $F_{SI,SD}^2(E_R)$ are the nuclear form factors as a function of recoil energy.

In the spin-independent case the cross section can be written as [14]

$$\sigma_{SI}^0 = \sigma_\chi \frac{\mu_A^2}{\mu^2} \left[Zf^p + (A-Z)f^n \right]^2 \tag{1.4}$$

where $f^{p,n}$ are the coupling strengths for the protons and neutrons. In this example, $f^p = f^n$ (they equally contribute), therefore the cross section goes as A^2. The A^2 dependence causes a rate enhancement for heavier elements at low energies but as the energy increases the form factor suppression will become dominant.

The spin-dependent cross section is expressed as

$$\sigma_{SD}^0 = \frac{32}{\pi} \mu_A^2 G_F^2 \left[a_p \langle S^p \rangle + a_n \langle S^n \rangle \right]^2 \frac{J+1}{J} \tag{1.5}$$

where S^p, S^n are the expectation values of the nuclear spin for the proton (S^p) and neutron (S^n), a_p, a_n are the proton, neutron couplings, and J is the total nuclear spin [14]. For spin-dependent interactions, only unpaired nucleons will contribute. Therefore experiments who wish to detect this form of scattering must choose a target material with an uneven number of protons or neutrons.

1.3.2 Direct Detection Techniques

Due to the expected low energy WIMP-nucleon recoils and low event rate, the direct detection of dark matter requires the use of technologies with low detector thresholds and vigorous background rejection methods. Target materials will produce a detection signal in the form of phonons (crystal lattice vibration quanta), bubble nucleation, scintillation light, or ionization.

Phonons

Detectors which employ this technique measure the recoil energies deposited after collisions with nuclei and electrons in a crystal lattice. A particle recoil in a crystal lattice generates phonons (vibrations of the electrons and nuclei of the lattice). This technique requires the detector to be cooled to cryogenic temperatures. The generation of phonons causes a change in temperature of the detector. Due to the T^3-dependence of the heat capacity of dielectric crystals even a small energy deposition can cause measurable temperature changes of the material which allows these detectors to reach low energy thresholds [15].

Bubble Nucleation

Detectors which utilize bubble nucleation, called bubble chambers, use superheated fluids to detect the passage of particles. These detectors probe the spin-dependent channel through the use of targets which have uneven total angular momentum; a favored target is ^{19}F. The target material is kept just below the boiling point in a metastable state which is disrupted when energy is deposited leading to the formation of bubbles. These bubbles can be detected both acoustically and optically.

Additionally, bubble chambers have the ability to adjust their temperature and pressure such that they are only sensitive to nuclear recoil events eliminating the need for large background (in the form of βs and γs) rejection power. However, because there is a minimal energy required to induce the formation of bubbles, reconstruction of event energies below this threshold energy is not readily available. This makes these detectors only able to count the number of events above threshold [15] [14].

Scintillation

Scintillation is the light produced when a particle scatters off an atom of the target material, exciting the target and emitting light. This scintillation light is then detected by commonly used photomultiplier tubes (PMTs). Many types of materials will produce scintillation light, but to be a good candidate for use in dark matter detection the conversion of recoil energy to light must be done efficiently as well as not be reabsorbed by the target material. The de-excitation of the target atoms produces photons that have a characteristic decay time and wavelength. The scintillation photons can be collected for energy reconstruction. In general, the energy is proportional to the number of scintillation photons. Materials commonly used in dark matter experiments and that meet these requirements are inorganic crystals, such as NaI(Tl), and noble elements in their liquid state such as argon and xenon.

Ionization

Other experiments rely on ionization as a detection signal. When enough energy is transferred to the target atom, the atom will ionize, freeing electrons. The, now free, electrons can be collected through the use of a strong electric field. Dual-phase noble gas detectors use the ionization signal in addition to scintillation light. In these detectors, electrons which survive recombination are drifted towards the gaseous region by an electric field where they encounter a much stronger electric field. The electric field will accelerate the electrons producing electroluminescence which is then collected by photomultiplier tubes or another type of light sensor. Germanium detectors, when using ionization, can achieve low energy thresholds, $\sim 0.5 \text{keV}_{ee}$, which allows them to search for very low mass WIMPs, around a few GeV/c^2 [14]. Semiconductor experiments, such as CoGeNT, are not able to separate nuclear and electron recoil events. However, the energy resolution of these detectors allows them to identify background sources.

1.3.3 Direct Detection Current Status

Currently, there are many direct detection experiments involved in the search for dark matter. In particular, the DAMA collaboration has studied the annual modulation of the dark matter event rate. This experiment is composed of 250 kg of highly radiopure NaI(Tl) crystals and is located

at the undergound lab of the Gran Sasso National Laboratory (LNGS). DAMA uses the regular change in the event flux caused by the movement of the Earth through the galactic dark matter halo. It does not have the ability to discriminate β/γ events from nuclear recoil events; it only measures the total flux as a function of time. However, the model independent signature has a few defining features which allows the signal to be differentiated from variations in the background. Of note, this type of modulation is expected to have a period of one year with a max amplitude around June 2nd and a minimum around December 2nd, the modulations occur in the low energy range, and they should be only single scatter events. DAMA has reported the detection of this signal at 9.3σ C.L. over 14 annual cycles in the 2-6 keV range [16]. However, this result conflicts with those reported by CDMS and CRESST-II after detector improvements in components and analysis were made [17] [18].

The DM-Ice collaboration is attempting to either affirm or rule out the DAMA signal. The DM-Ice17 detector (the first of the program) houses the same target material as DAMA, NaI(Tl), but it is located at the South Pole under 2200 m.w.e. of glacial ice. However, currently, in results just published, the signal seen is consistent with zero modulation, but it is not yet sensitive enough to make a definitive claim [19].

The best limit to date in the search for dark matter has been set by the XENON1T experiment. XENON1T is a liquid xenon detector with 1042 ± 12 kg of fiducial mass located in the Laboratori Nazionali del Gran Sasso (LNGS). XENON1T sets an exclusion limit of 7.7 x 10^{-47} cm^2 for a WIMP mass of 35 GeV/c^2 at 90% confidence level with an exposure of 34.2 live days [20]. Current limits for other experiments are shown in Fig. 1.4. As the next generation experiments become larger they will encounter an irreducible background in the form of neutrinos, which constitutes the neutrino floor.

The ability to reject and/or minimize background events has become more important than ever since no clear WIMP signal has been found. To minimize background effects, it requires the capability to effectively discriminate between β/γ events and nuclear recoil events. Liquid argon, which allows for excellent event discrimination, is a complimentary target to xenon with the advantage of much more power in pulse shape discrimination between nuclear and electron recoils. For this reason, liquid argon is an excellent target material for future multi-tonne detectors with sensitivity two orders of magnitude smaller in the cross-section for high mass WIMPs.
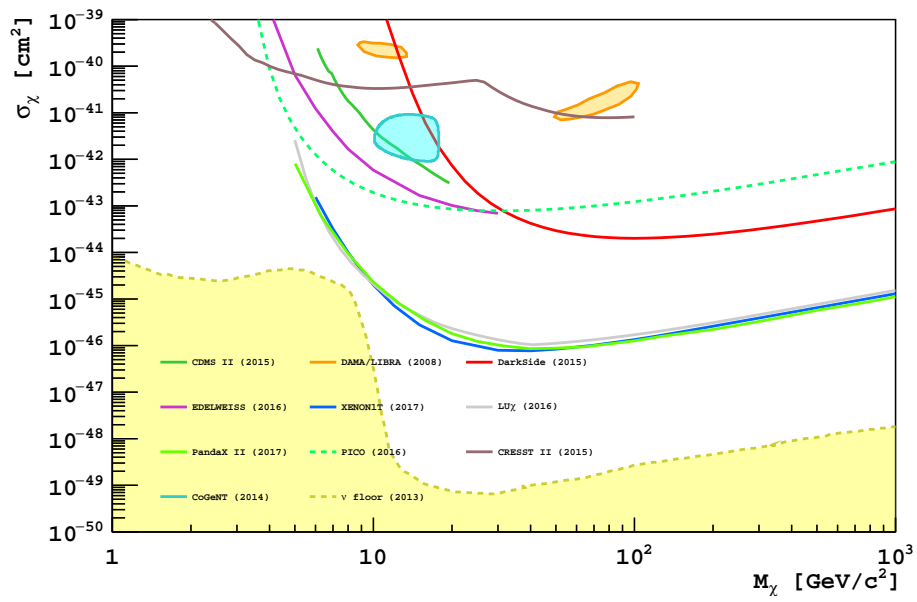
Figure 1.4: Current limits for direct dark matter detection. The DAMA/LIBRA results shown are interpreted for the WIMP model.

CHAPTER 2
THE DARKSIDE PROGRAM

DarkSide-50 is a direct detection dark matter experiment. It is part of a phased program that began with DarkSide-10 in 2010 at Princeton University [21]. DarkSide-10 was a prototype liquid argon two-phase time-projection chamber (TPC) consisting of 10 kg of liquid argon. The liquid argon was observed by two arrays of 7 PMTs at the top and bottom. DarkSide-10 demonstrated the viability of using a liquid argon TPC. DarkSide-10 was able to achieve a scintillation light yield of 9.1 pe/keV$_{ee}$ [22].

DarkSide-50 is the next phase of the DarkSide program and the first in the program with the ability for physics reach, in addition to it being a research and development tool for the continuation of the DarkSide program. DarkSide-50 consists of three nested detectors, the Water Cherenkov Muon Veto (WCV), the liquid scintillator neutron veto (LSV), and the liquid argon TPC (see Figure 2.1). It is located underground in Hall C of Laboratori Nazionali del Gran Sasso (LNGS) in Italy. In the following sections, each of the three detectors will be discussed in detail.

2.1 Outer Detector Vetoes

One of the main goals and advantages of DarkSide-50 is its potential to be background-free. This is done through active vetoing and passive shielding with the outer detectors. Background particles consist of γ-rays and neutrons from the rock, cosmogenic muons which can interact with the detector components and produce neutrons and other spallation products, (α,n) reactions in the detector materials, and radioactive decays in the detector materials [23].

2.1.1 Water Cherenkov Muon Veto

The Water Cherenkov Muon Veto (WCV) acts as a passive shield against external backgrounds, such as γ-rays and neutrons from the surrounding rock. It is also a Cherenkov muon detector. DarkSide-50 sits at a depth of 3800 meters water equivalent; at this depth, cosmic-rays are reduced from that found at the Earth's surface by $\sim 10^6$ [24]. Cosmogenic muons that do make it to DarkSide-50's location can interact in the detector or the surrounding rock and produce high energy neutrons.

The WCV, originally the Borexino Counting Test Facility, is 10 meters high by 11 meters wide. It is filled with approximately 1000 tonnes of ultra-pure water. Eighty 8-inch PMTs monitor the WCV and detect Cherenkov radiation produced by passing muons before they reach the inner detectors.
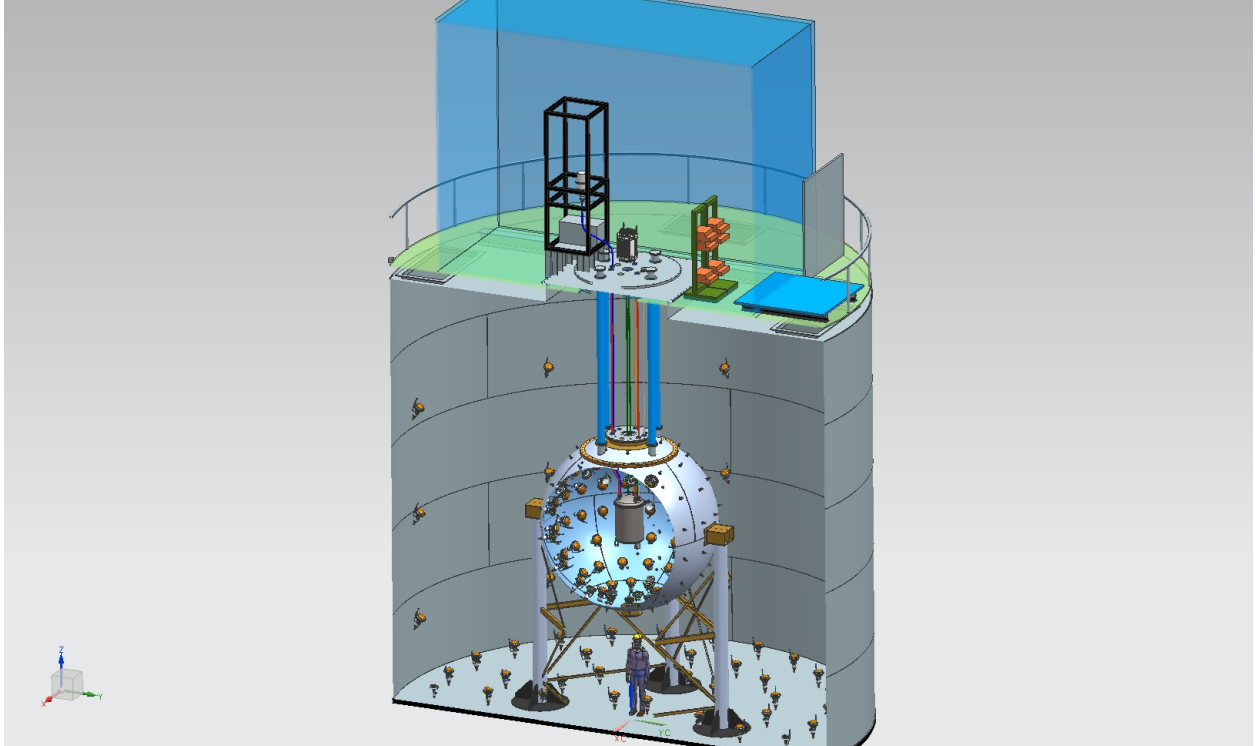
Figure 2.1: A cross-sectional view of DarkSide-50. On top is CRH, a radon free clean room, where the detector electronics are located. Below is the Water Cherenkov Muon Veto (WCV) with the Liquid Scintillator Neutron Veto (LSV) sphere housed inside. Then, in the center of the LSV is the cryostat which houses the Liquid Argon Time-Projection Chamber (LAr TPC).

2.1.2 Liquid Scintillator Neutron Veto

Housed within the WCV is the Liquid Scintillator Neutron Veto (LSV). Nuclear recoils produced by WIMP interactions with nuclei are indistinguishable from recoils produced by interactions with neutrons. Therefore, it is imperative that an accurate measurement of the neutron background is made. The LSV offers an *in situ* measurement of this background and captures 99.3% of the neutrons that reach the TPC.

The LSV is a 4 meter diameter stainless steel sphere filled with 30 tonnes of organic scintillator called pseudocumene and it is monitored by 110 PMTs. Pure pseudocumene has a mean neutron capture time of approximately 253 μs. By doping the pseudocumene with boron, the mean capture time is reduced to approximately 2.3 μs [25]. In the LSV, the scintillator is doped with 5% by volume trimethylborate (TMB). ^{10}B has the ability to capture thermal neutrons with a total cross-section of 3837 barns via two channels:

$$^{10}\text{B} + \text{n} \rightarrow \quad ^{7}\text{Li}(1015 \text{ keV}) + \alpha \ (1775 \text{ keV}) \quad (6.4\%)$$
$$^{10}\text{B} + \text{n} \rightarrow \quad ^{7}\text{Li}^{*} + \alpha \ (1471 \text{ keV}),$$
$$^{7}\text{Li}^{*} \rightarrow ^{7}\text{Li} + \gamma \ (478 \text{ keV}) \quad (93.7\%)$$
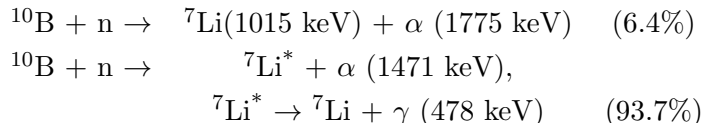
Each of the capture channels produce reactants energetic enough to be detected. The alpha only channel, in which neutrons are captured on boron only 6.4% of the time, results in the production of just an α particle. This particle is energetic, at 1775 keV, but it is heavily quenched. Therefore, detecting this α is the means for showing an efficient neutron veto.

Within the LSV, there are three fish-eye CCD cameras installed. These allow one to take pictures of the inside of the LSV for calibration purposes (See Chapter 4). The cameras provide their own light which illuminate the inside of the LSV and shine to verify the positioning of a source as a means of cross-checking the placement.

2.2 Liquid Argon TPC

The main detector of DarkSide-50 is the two-phase liquid argon time projection chamber (TPC), suspended inside the LSV (see Figure 2.2). The TPC has an active volume of 50 kg of liquid argon (150 kg total liquid argon) for the WIMP target viewed by two arrays of R11065 Hammamatsu PMTs, 19 on top and 19 on bottom in a hexagonal pattern. The PMTs are fully submerged in liquid argon (LAr). The TPC body is constructed of a solid teflon (PTFE) cylinder measuring 36 cm in diameter and 36 cm in height; it is contained by a double-walled stainless steel cryostat (see Figure 2.4). There is a 5 mm space between the inner and outer walls of the cryostat that is filled with Mylar multilayer insulation and evacuated. This helps to reduce heat losses and to keep the temperature of the LAr at approximately 87 K. Above the bottom PMTs and below the top PMTs are fused silica windows that are coated with the wavelength shifter, tetraphenyl-butadiene (TPB).

Figure 2.2: The crystat containing the LAr TPC suspended in the LSV and surrounded by the LSV PMTs.

Figure 2.3: The LAr TPC as it is about to be placed inside the cryostat.
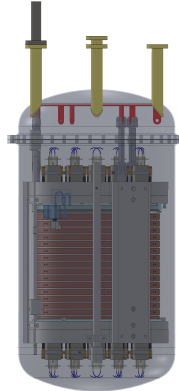
Figure 2.4: A conceptual drawing of the LAr TPC inside the cryostat

Argon light has a wavelength of 128 nm in vacuum, hence the wavelength shifter which converts the argon light to the visible at 420 nm. The wavelength shifter, TPB, is coated along all sides of the TPC.

The active region of the TPC is defined as a right cylinder of 35.6 cm in diameter and 37.1 cm in height with the last centimeter of the region filled with gaseous argon. At the bottom of the active volume is the cathode and at the top of the gaseous argon (still within the active volume) is the anode; these electrodes are formed by thin layers of indium tin oxide (ITO). A third electrode, a 95% transparent grid, is positioned just below the top of the liquid argon. A uniform electric field (nominally 200 V/cm) is established between the cathode and the grid by the presence of copper field-rings on the outside of the inner wall of the cryostat (see Figure 2.3). This is used to drift electrons to the gaseous region of the TPC where they are met by the extraction grid. Between the grid and the anode, there exists a stronger electric field (2.8 kV/cm)to extract electrons from the liquid and produce secondary scintillation light (See Chapter 3).

CHAPTER 3
LIQUID ARGON TIME PROJECTION CHAMBER

3.1 Scintillation Mechanism

The mechanism of scintillation in liquid argon is described by the recoil of an argon atom. The recoil energy of a given argon atom is split into three channels: excitation, ionization, and heat. In the case of heat, this energy is not visible and is therefore considered lost. For excitation, an excited argon atom combines with a ground state argon atom to produce an excited dimer (excimer, Ar_2^*) in either the singlet ($^1\Sigma_u^+$) or triplet state ($^3\Sigma_u^+$). The excited dimer will then relax with the emission of a VUV photon at 128 nm. The decay times of the singlet and triplet states of the exited dimer differ greatly: the lifetime of the singlet state is 7 ns whereas the triplet state decays after $1.6\mu s$. In the case of ionization, an ionized dimer (Ar_2^+) will form. The ionized dimer will exist in this state until eventual electron recombination which results in an excited dimer state. From this point, the process follows that of the excitation path with the emission of a VUV photon. This process is illustrated in 3.1.

In the case of recoil events caused by the scattering of electrons or photons, excimers are created preferentially in the long-lived triplet state. They are also more likely to ionize the argon atom. For nuclear recoil events, like those produced by neutrons, alpha particles, or WIMPs, excimers are created in the short-lived singlet state with less ionization. The difference in decay lifetimes of the singlet and triplet states coupled with the preferential creation difference of excimers allows for event discrimination at the level of 10^7 in argon from the scintillation signal alone [26].

3.2 Energy Transfer

The energy given to the argon target, neglecting energy lost as heat, can be written as

$$E_0 = N_i E_i + N_{ex} E_{ex} \tag{3.1}$$

where N_i and N_{ex} are the numbers of ions and excitons produced by an ionizing particle and E_i and E_{ex} are the ionization and excitation energies, respectively. The maximum number of scintillation photons produced, assuming that each excited or ionized particle will produce one scintillation photon is given by [27]

$$N_{ph} = N_i + N_{ex} = N_i(1 + \frac{N_{ex}}{N_i}) = \frac{E_0}{W}(1 + \frac{N_{ex}}{N_i}). \tag{3.2}$$
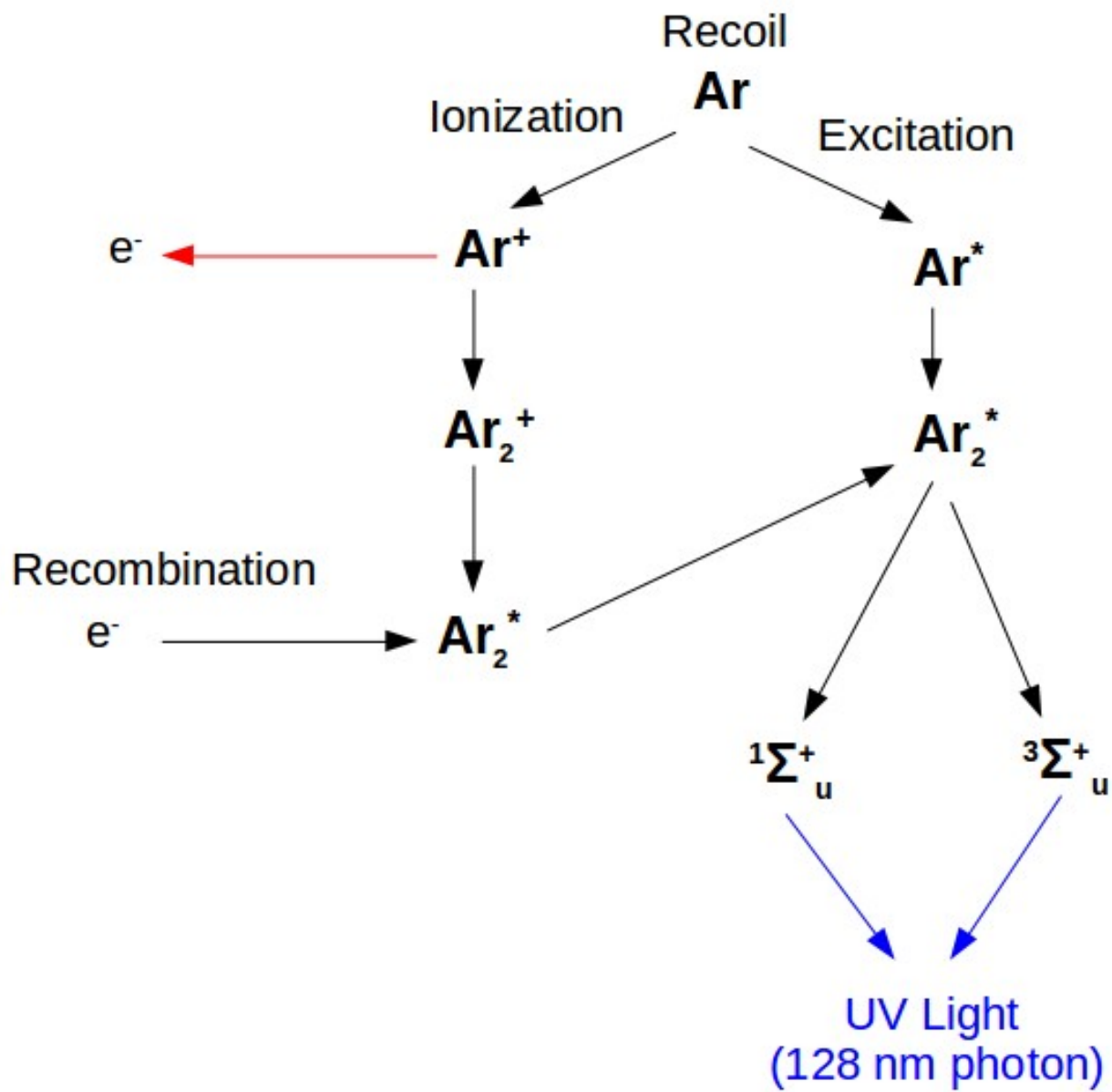
Figure 3.1: Illustration of the scintillation process in argon.

where $W \equiv E_0/N_i$ is the average energy needed to produce an electron-ion pair. One can then write the average energy for the production of one scintillation photon as

$$W_{ph} = \frac{W}{1 + \dfrac{N_{ex}}{N_i}}.$$

(3.3)

W	23.6 ± 0.3 eV
N_{ex}/N_i	0.21
W_{ph}	19.5 eV

Table 3.1: Measured values of W and N_{ex}/N_i with the calculated value for W_{ph} for electron recoils in liquid argon. [28] [29] [30]

.

W and N_{ex}/N_i have been found experimentally allowing for the calculation of W_{ph}. The values for electron recoils in liquid argon are summarized in Table 3.1.

An incoming particle will scatter off many argon atoms depositing energy in a track of excited and ionized argon. The length and density of this track, measured in terms of the linear energy transfer (LET), is dependent on the type of particle. The intensity ratio of the singlet to triplet state shows a greater singlet state formation for higher deposited energy density; for nuclear recoils this ratio is 3 and for electron recoils this ratio is 0.3 [31]. The singlet to triplet intensity ratio increases with LET. This gives rise to the event discrimination introduced in the previous section.
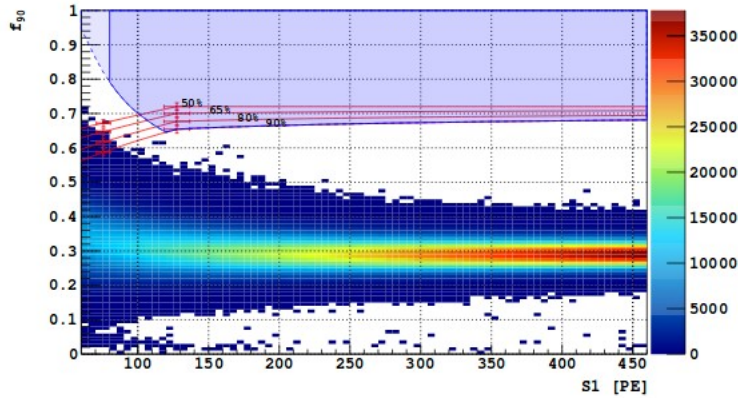
Figure 3.2: Distribution of events in the f90 vs S1 plane with the nuclear recoil acceptance curves overlaid. The events in the lower range of f90 are electron recoil events; this demonstrates the discrimination between nuclear recoils and electron recoils as nuclear recoils have a higher f90 value. [26]

The effectiveness of event discrimination is dependent on the scintillation efficiency of the target medium since the different types of excitation are directly related to the ratios of triplet to singlet states. Thus, the light yield, the number of photoelectrons detected per unit energy, sets the energy threshold for the detector and ultimately the sensitivity of the detector to nuclear recoils (WIMP recoils). For nuclear recoils, a large portion of the recoil energy is lost to heat, therefore, the light yield is expected to be less than that for electron recoils. The ratio of scintillation light yield for nuclear recoils to electron recoils is defined as L_{eff}, the scintillation efficiency. For liquid argon, L_{eff} has been measured to be 0.25 ± 0.01 for recoil energies above 20 keV [32].

3.3   Two-Phase Time Projection Chamber

DarkSide utilizes a two-phase time projection chamber (TPC) shown in Fig. 3.3. The DarkSide TPC consists of a cylindrical volume filled with liquid argon and observed by two arrays of PMTs on the top and bottom of the volume. The sensitive liquid argon volume is immersed in an applied electric field while at the top of the TPC is a thin layer of gaseous argon. When a particle enters the TPC and scatters off the liquid argon, it will deposit energy in the form of excitation and ionization as discussed in the previous section. Some ionized electrons will recombine and contribute to the primary scintillation signal, referred to as S1. The electrons that do not recombine will drift upward towards the gaseous argon due to the applied electric field. Just before these electrons reach the gaseous argon, they encounter the extraction grid. The extraction grid has a stronger electric field applied across it which accelerates the electrons out of the liquid argon and into the gaseous argon. This produces a secondary scintillation signal due to electroluminescence, known as S2 or the ionization signal since it is produced by ionized electrons.

All the interior surfaces of the TPC are coated with TPB, a wavelength shifter. Scintillation photons are absorbed by the TPB and reemitted isotropically as visible photons which can be detected by the PMTs. The, now visible, photons strike a photocathode at each PMT which produces electrons via the photoelectric effect. Each photon produces photoelectrons with a certain quantum efficiency which is common for all PMTs. The number of electrons producing the signal varies for each PMT. Therefore, the gains of each PMT must be calibrated. From the discussion in the previous section and Eq.3.2, the number of scintillation photons produced directly depends on the energy deposited, one can reconstruct the recoil energy from the S1 signal. In addition, since electron recoils tend to cause more ionization they have a larger S2 signal than do nuclear recoils. This provides another method for event discrimination, namely the S2 to S1 ratio. In two-phase TPCs, this effect is enhanced: due to the applied electric field the ionization electrons are less likely to recombine thus preventing them from contributing to the S1 signal and are therefore left to increase the S2 signal. Understanding the relationship between S1 and S2 is important in understanding the energy scale of the detector and how the detector responds to various interactions.

The S2 to S1 ratio is critically important to liquid xenon detectors which have a small difference

in the decay times between the singlet and triplet states (3 ns and 27 ns, respectively, [12]) and cannot rely on pulse shape discrimination alone. For liquid argon detectors, the rejection power based on S1 alone is sufficient for WIMP searches while S2/S1 can be used a cross-check.

3.4 Argon Extracted from Underground

The use of argon as a target for dark matter interactions has one major drawback: the presence of ^{39}Ar. ^{39}Ar, a β emitter with a half-life of 269 years, is formed in the atmosphere by cosmic ray activation. With an activity of 1 Bq/kg in atmospheric argon, ^{39}Ar puts a limit on the size and sensitivity of dark matter detectors that use atomspheric argon. Argon sourced from underground should be depleted in ^{39}Ar owing to its half-life and long time the argon was trapped underground, thousands of years. However, even argon from the subsurface of Earth could be contaminated with ^{39}Ar; it can be produced through neutron capture by ^{39}K. Therefore, it is necessary to find argon from an underground location which has a low free neutron flux [33]. The Kinder Morgan Doe CO_2 extraction facility in Cortez, Colorado provided an ideal location for sourcing underground argon. The argon sourced from underground at that facility was found to have 6.6 mBq/kg specific ^{39}Ar activity which is less than 0.65% of the ^{39}Ar activity in atmospheric argon [34]. After filling DarkSide-50 with underground argon, the residual level of ^{39}Ar has been precisely measured to be reduced by a factor of $(1.4 \pm 0.2) \times 10^3$ relative to atmospheric argon [35].
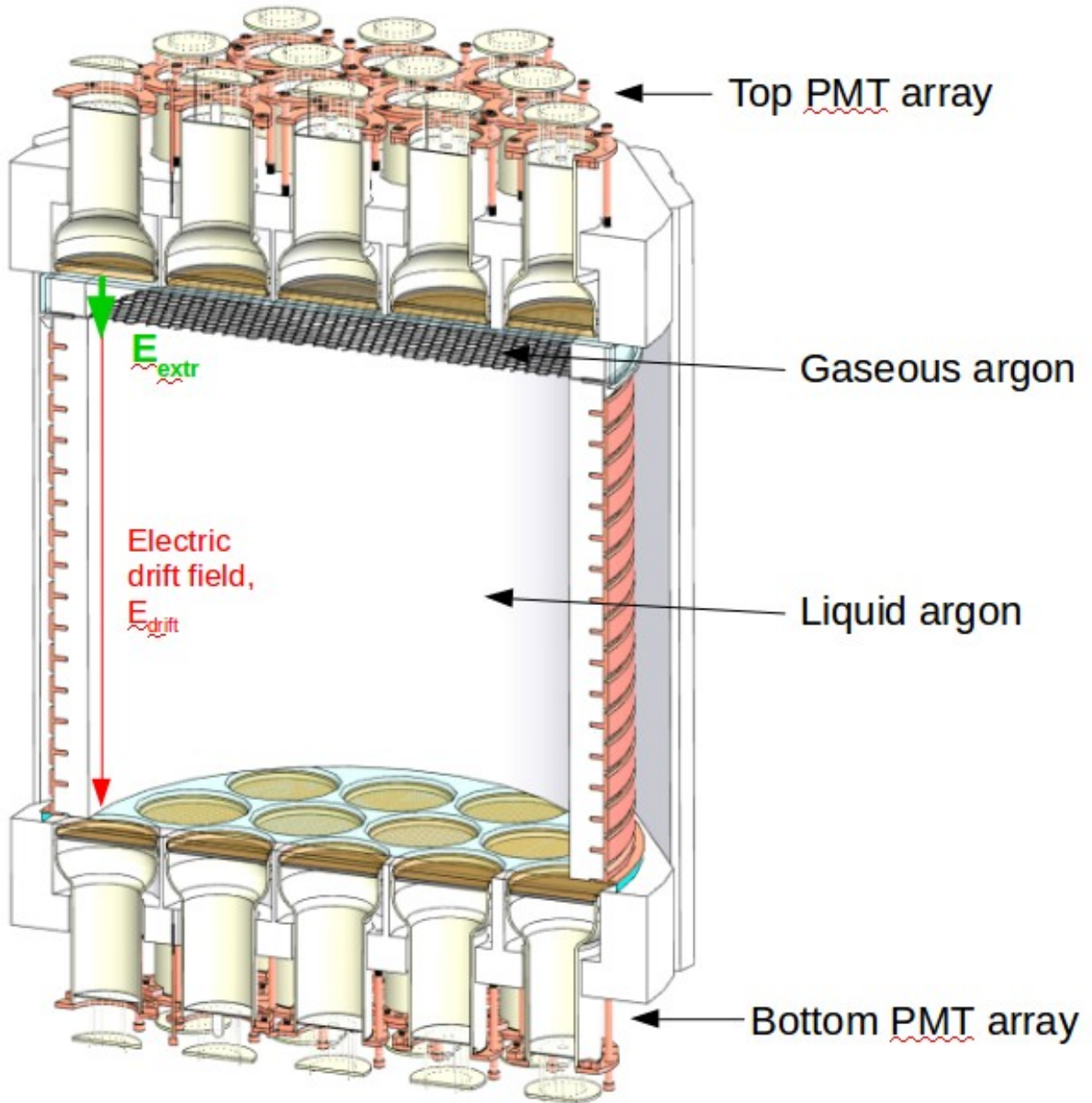
Figure 3.3: Cross-sectional view of the two-phase time projection chamber (TPC).

CHAPTER 4
CALIS - CALIBRATION INSERTION SYSTEM

Calibration of DarkSide-50 is performed for each of the three detectors (WCV, LSV, and LAr TPC). The WCV calibration requirements are limited to the SPE response of the PMTs using a dedicated laser system. The LSV and the LAr TPC each have their own laser system. Measurements using the laser system give regular updates on the PMT gain for the detectors. Knowing the neutron vetoing efficiency for the LSV is one of the requirements for DarkSide-50 toward background free running. Additionally, the LSV and the LAr TPC require their light yield to be accurately measured at a range of energies.

The light yield may be calculated using spectral features from the intrinsic background and through the use of radioactive neutron and gamma sources with known energies. In the LSV, known contaminants in the materials of the detector provide a means of determining the light yield. The most visible contaminants are ^{14}C, ^{60}Co, and ^{208}Ti. The light yield is derived from fits to the ^{14}C β^- spectrum, the two ^{60}Co γ-rays, and the ^{208}Ti γ-ray; measurements of the light yield from these sources are summarized in Table 4.1 and the full LSV spectrum is shown in Figure 4.1 [23]. Calibration using intrinsic backgrounds is complementary to calibration using introduced radioactive sources. In the TPC, ^{83m}Kr can be injected into the LAr TPC. ^{83m}Kr has a half-life of 1.83 hours; therefore, the radiation introduced into the TPC from this source decays away with no lasting implications for the detector. It produces two low energy lines at 32.1 keV and 9.4 keV separated by 154 ns. In DarkSide-50, these lines are not separable and are measured as a single peak/calibration point at 41.6 keV.

Additional needs for calibration are met by introducing radioactive neutron and gamma sources. These sources have long half-lives and must be safely inserted into the LSV, near the LAr TPC and removed. This is done by using a dedicated calibration system, CALIS (CALibration Insertion System) which is described fully in the following sections.

4.1 CALIS Requirements

The CALibration Insertion System (CALIS) for DarkSide-50 was designed and built by Cary Kendziora at Fermi National Laboratory (FNAL) and DarkSide members at the University of

Isotope	Decay Mode	Energy (keV)	Light Yield (PE/keV)
^{14}C	β^-	156 (endpoint)	0.561 ± 0.013
^{60}Co	2γ	1173,1332	0.592 ± 0.011
^{208}Ti	γ	2614	0.551 ± 0.002

Table 4.1: Summary of Light Yield Measurements for the LSV. [23]
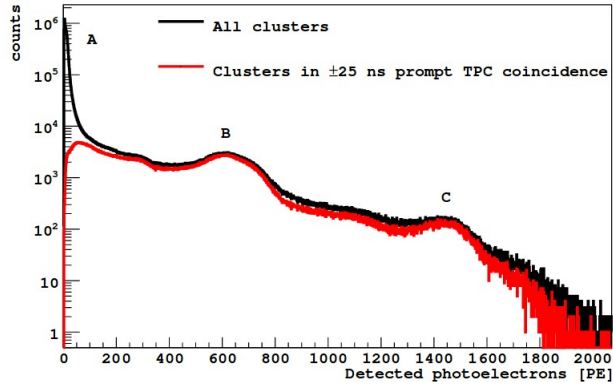
Figure 4.1: Photoelectron spectrum for the LSV. Region A consists mainly of after-pulses, Region B is the ^{60}Co peak, and Region C is the ^{208}Ti peak. [23]

Hawaii, during the spring and summer of 2014. After extensive testing and commissioning at both FNAL and LNGS by the Hawaii group, CALIS was installed atop DarkSide-50 in the fall of 2014. CALIS was mounted on a gate valve, inside CRH (a clean room on top of the WCV), which allows access to the LSV. Calibration sources are lowered into the LSV through an organ pipe where they may be placed next to the LAr TPC or rotated away from the TPC (see Figures 4.2 and 4.3).

Design and Operation CALIS is comprised of three main parts: the lower assembly, the upper assembly, and the source deployment system. The lower assembly is a cylindrical tube, the base of CALIS, and is mounted on the gate valve, Figure 4.4. The upper assembly, mounted directly on top of the lower assembly, consists of the view port which allows access to the source deployment system for source insertion and exchange. The view port is located at the bottom of the upper assembly. The top of the upper assembly houses the cable spools and the stepper motor, while the articulation wheel is located on the side of the top of the upper assembly, Figure 4.5. The source deployment device, referred to as the "PIG" (an acronym for Pipeline Insertion Gauge, in reference to a device used for the cleaning and maintenance of pipelines), consists of two conical sections (top and bottom) which hold the articulation arm, Figure 4.6. The conical sections provide weight and stability for the PIG as it is lowered into the liquid scintillator and allow for a smooth transition through the organ pipe.

The gate valve upon which CALIS is mounted is closed at all times, except during calibration campaigns. Prior to opening the gate valve, CALIS is evacuated, purged with nitrogen, and then evacuated again. This "pump and purge" process is repeated several times to remove oxygen and humidity from inside CALIS. Oxygen and humidity inside CALIS would negatively impact the quality and stability of the liquid scintillator due to their quenching effect on the scintillator and their deterioration of scintillation properties. After a calibration campaign is completed and the PIG is brought to its home position, before the opening of the
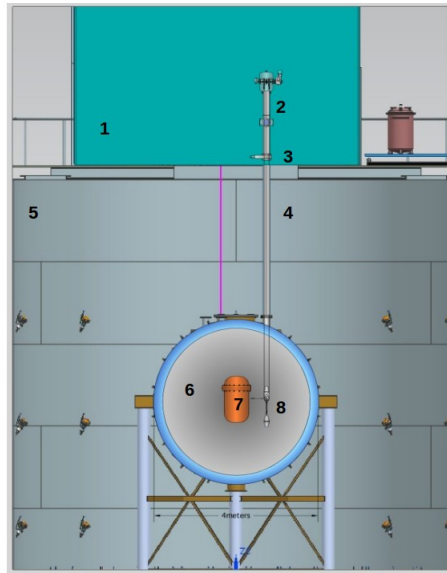
Figure 4.2: Drawing of CALIS inside the LSV next to the TPC. The numbered points correspond to: (1) CRH, the clean room; (2) CALIS; (3) the gate valve upon which CALIS is mounted; (4) organ pipe through which the source is deployed; (5) the WCV; (6) the LSV; (7) the LAr TPC; (8) the source deployment system with the source arm articulated.
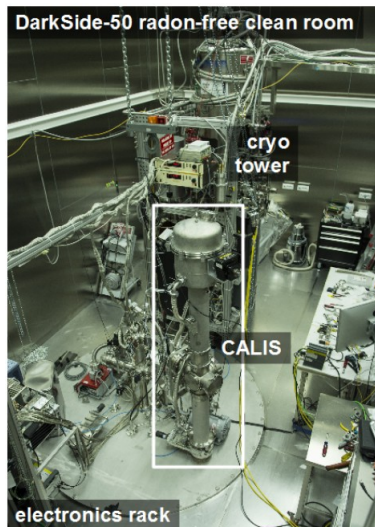
Figure 4.3: CALIS located inside CRH.
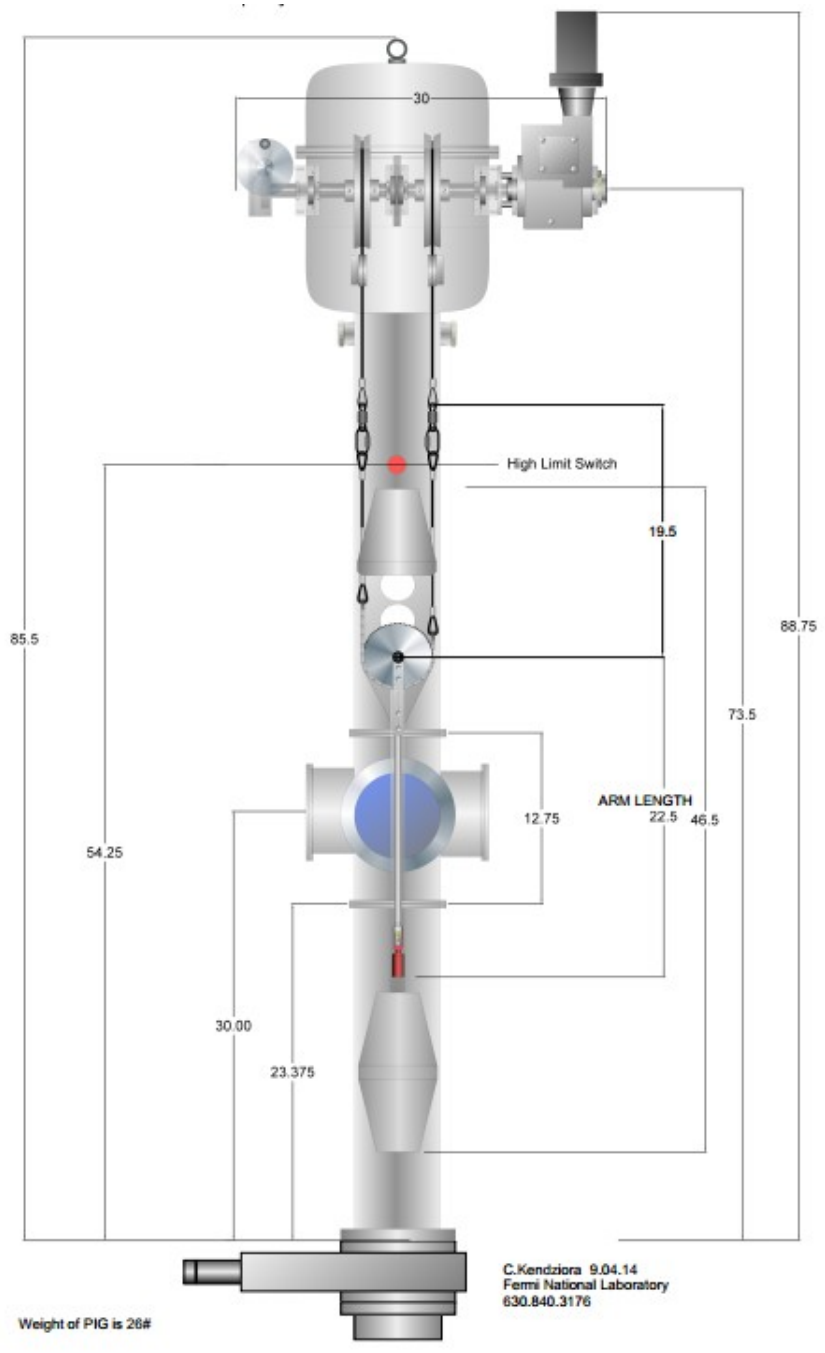
Figure 4.4: Schematic drawing of CALIS with dimensions in inches.
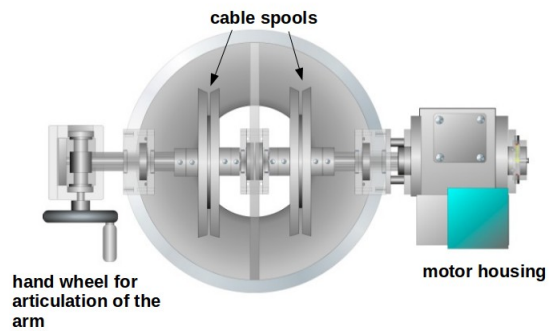
Figure 4.5: Drawing of the upper assembly looking down from above.

Figure 4.6: The source deployment device, known as the PIG. *Left:* The PIG with the source arm de-articulated, in its vertical position. *Right:* The PIG with the source arm articulated to 90° which allows the source to be brought close to the TPC and in general, extends the range of motion.

Figure 4.7: The clamp between the upper and lower assemblies. This clamp can be loosened to perform azimuthal rotation. The ruler, shown here, allows one to measure the rotation angle.

view port to remove the source, another cycle of pump and purge is performed (gate valve is again closed for this process). This is to remove all traces of scintillator from the apparatus for both the safety of humans and the electronic equipment inside CRH. Due to the presence of ^{10}B in the scintillator, this process is especially important since ^{10}B can interact with the moisture in the air to create boric acid.

The PIG is lowered into position next to the TPC cryostat using a stepper motor. The stepper motor is controlled through a LabVIEW interface on a dedicated laptop located inside CRH next to CALIS. The stepper motor has an absolute encoder which records the position of the PIG, even in the event of a power failure. The PIG is connected to the stepper motor through two stainless steel cables which are wound on two spools. By rotating both spools simultaneously, the PIG is lowered through the gate valve, into the organ pipe down into the LSV. Once the PIG is in position, one can rotate one cable spool by using the articulation wheel located on the outside of the upper assembly. This results in the source arm articulating and the PIG lifting fractionally in the vertical direction. Articulation is in the range between $0°$ and $90°$. Once the articulation wheel is engaged (i.e. movement of the wheel is initiated), all vertical motion of the PIG is stopped by a limit switch which cuts the power to the stepper motor. This prevents the PIG from being retracted into the organ pipe with the source arm articulated; motion of the PIG with the source arm extended could result in damage to PMTs or the exterior of the cryostat. For azimuthal rotation of the PIG, one can rotate the upper assembly of CALIS, see Figure 4.7.

4.2 FNAL Testing

Initial testing of CALIS was perfomed at Fermi National Laboratory (FNAL) in Batavia, Illinois during August and September of 2014. The goal of the testing was to determine the stability of the system in terms of source positioning, minimal lateral motion during deployment, and functionality of the safety features. The PIG must traverse a good portion of the height of the WCV, ∼7m, so testing was performed in the Wide Band Lab. The Wide Band Lab has a high bay platform upon which CALIS was mounted and the PIG was lowered to the ground via a hole in the platform. Results of the various tests performed are given below.

4.2.1 Z Position Reliability

It was neccessary to calibrate the relation between stepper motor steps and vertical displacement because the steps are given in arbitrary units. This was done by lowering the PIG from its home position (home position is defined as the position in which the PIG is above the gate valve with the source holder in view through the view port) to the very bottom position where the cables are completely unwound from their spools. Once the PIG reached it maximum position a piece of tape was placed over the bottom of the lower conical section. This gave a consistent spot with which to point a laser ranger to measure the vertical displacement of the PIG. At the maximum position, the distance from the laser ranger (set on the floor of the Wide Band Lab) to the bottom of the piece of tape was measured and recorded. Then the PIG was moved up, towards the home position, stopping at regular intervals and measuring the distance from the bottom of the tape to the laser ranger each time. Once the PIG arrived home, it was again deployed to the same step positions as the first run and the vertical distance was measured. This process was repeated for a total of 31 times; a large number of trials was completed in order to detect any slippage of the cables which could be small for each trial, but would accumulate over time.

The Z-positioning was found to be very accurate with no measurable slipping. All vertical measurements were found to be within ∼2 mm, which agreed with the unevenness of the tape surface.

4.2.2 Lateral Motion during Deployment and Articulation

In order to decrease the lateral motion of the PIG during deployment, the PIG is lowered at a slow speed, 4 mm/s. Due to this slow speed, no measureable lateral motion while deploying was detected. However, when the PIG is in position near the TPC, in order to bring a source close to the cryostat, the source arm must be articulated. The articulation is done manually using a hand wheel to retract a portion of one of the cables. This can cause some friction and if done too fast, would result in the PIG swinging. This swinging could result in the PIG crashing into a PMT within the LSV, which must be avoided. To measure the swinging of the PIG during articulation,

a mock up of the cryostat with a ruler was mounted behind the PIG. The PIG was then filmed while articulation and de-articulation was performed. The videos were analyzed and it was found that the PIG swung ~1.5cm in air and it took about two minutes for the swinging of the PIG to fully stop.

4.2.3 Artiulcation Accuracy and Repeatability

Articulation of the source arm is required to place a radioactive source next to the cryostat. The articulation angle is measured by a protractor attached to the articulation wheel. In order to determine the accuracy of articulation, the PIG was lowered to two Z-positions. At each Z-position, the source arm was articulated to $90°$ as measured by a level placed along its top edge, the articulation angle was recorded, then the arm was de-articulated. Articulation of the arm also results in vertical displacement of the PIG, so the distance that the PIG moved during articulation was also recorded; the distance was measured when the arm was de-articulated, when it was articulated, and again, when it was de-articulated.

After de-articulation, the source arm did not return to its original vertical position. It maintained a small angle of about $2°$, even though the articulation wheel indicated that the arm should be vertical. Further investigation revealed that articulation is very sensitive to any tension which has accumulated in the cable. Therefore, it is neccessary to lower the PIG to its maximum position before placing it in position next to the TPC and articulation for calibration. This releases any accumulated tension in the cable.

4.2.4 Azimuthal Rotation Stability

The upper assembly can be azimuthally rotated to place the source arm next to the cryostat or away from the cryostat into the LSV. The rotation is done by loosening a clamp attached to the base of the upper assembly and manually rotating the upper assembly. A ruler indicates the amount of rotation. In order to determine the stability of azimuthal rotation, the PIG was lowered to a Z-position next to the cryostat mock up, the clamp was loosened, and rotation was performed. Despite the heavy weight of the upper assembly, slow and deliberate azimuthal rotation was achieved. There was no jerking of the assembly and no swinging of the PIG was induced.

4.2.5 Safety Features

CALIS needs to be leak tight, both when the clamp for azimuthal rotation is secure and when it is loose. The leak tightness of CALIS was verified with helium leak testing in both of these cases. The limit switch which prevents the PIG from moving in a vertical direction while the arm is articulated was found to work consistently. Additionally, there is an upper limit switch which stops the PIG from moving too far into the upper assembly (and possibly colliding with the cable spools). This

Figure 4.8: Safety clips, seen here, attached to the source arm as it is removed through the viewport.

upper limit was also found to work consistently.

Another safety feature of CALIS are the safety clips. These are attached to the outside of the lower assembly and connected to each other by stainless steel wire. When removing/inserting the source arm one must attach safety clips to avoid dropping the source arm into the bottom of the lower assembly on top of the gate valve, Figure 4.8. The safety clips must be attached before removing the locking pins from the source arm and more safety clips are attached to each locking pin as it is removed to avoid dropping a locking pin into the bottom of the lower assembly.

4.3 LNGS Testing, Commissioning, and Installation

Once testing at FNAL was concluded, CALIS was disassembled and shipped to Gran Sasso National Laboratory (LNGS) where it arrived in October of 2014. At LNGS, CALIS was once again tested for position reliability and characterization. All tests prior to installation in CRH were performed in Hall C of the underground laboratory where CALIS was mounted on the stairs at the side of OPERA detector, Figure 4.9. Once tests were completed, CALIS was disassembled, cleaned, and installed in CRH.

4.3.1 Position Characterization

The relationship between the physical location of the PIG and the motor step count is non-linear due to the cable being wound on a spool which, as the PIG is raised and lowered, the radius of

Figure 4.9: CALIS mounted atop the stairs next to the OPERA experiment in Hall C.
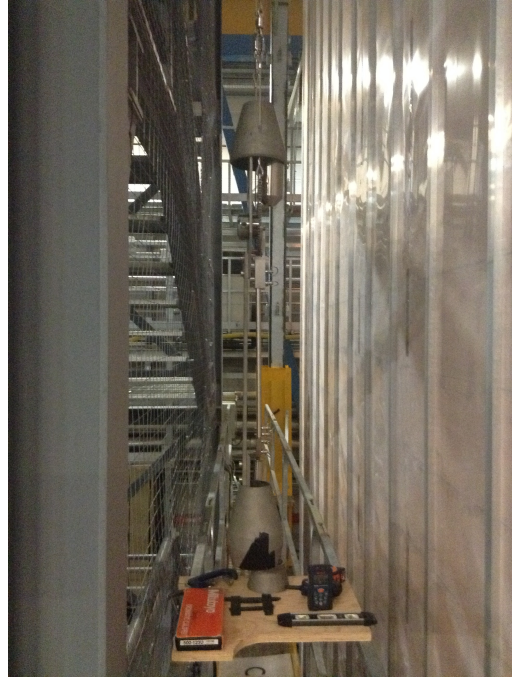
Figure 4.10: Close-up of the PIG next to the OPERA experiment during testing phase at LNGS.

cable on the spools changes. Also, this means that the hand wheel for articulation must be rotated by differing amounts depending on the vertical position of the PIG. The position of the PIG and the articulation of the source arm are not visible to the operator during a calibration campaign, therefore, the Z position and the hand wheel angle as a function of motor step count need to be well characterized.

As a first step, the Z position of the PIG at various motor step counts was again measured similar to the Z positioning test done at FNAL. This was done to verify that nothing was damaged in the shipping of CALIS. The next step was to determine motor step values which would correspond to actual vertical displacement of the PIG inside the LSV, see Figure 4.11. This was done by measuring the distance from the bottom of CALIS to a position that matched the location of the center of the cryostat within the LSV. Measurements were matched by comparing with known values from mechanical drawings of the WCV, LSV, and the TPC. The PIG was sent to various locations along the length of the cryostat. At each location, the motor step count and the Z position was measured (see Figure 4.10). Also, the source arm was articulated (articulation angle recorded), the vertical displacement of the PIG measured, and then the source arm was de-articulated with the Z position of the PIG again measured. This was repeated many times over the course of several days to determine repeatability.
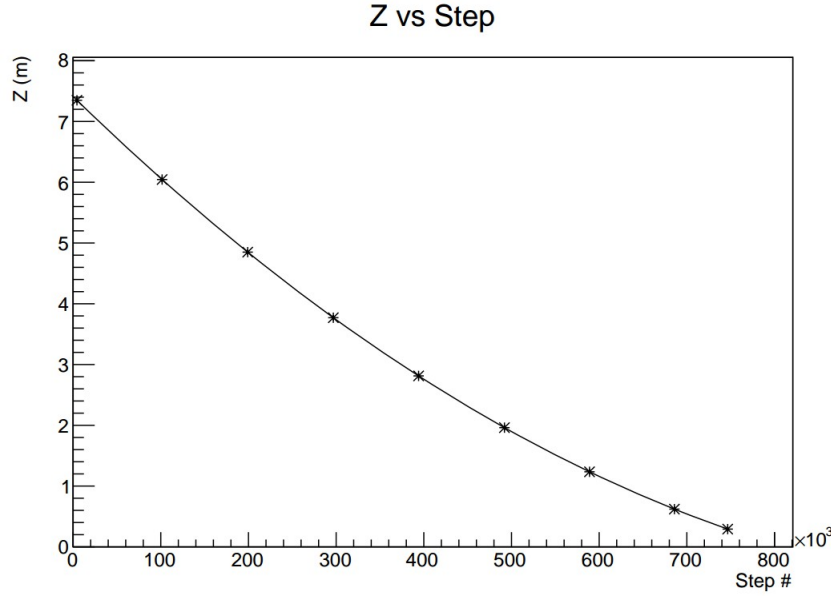
Figure 4.11: Results from the characterization of the Z position (in meters) of the PIG as a function of motor step count. The largest Z position corresponds to when the PIG is in its home position; the PIG is farthest from the laser ranger. Similarly, the smallest Z position is when the PIG is fully deployed, the cables are at their maximum length.

4.3.2 Cleaning and Installation

Once all testing on CALIS was completed, the system was disassembled and thoroughly cleaned in preparation for installation inside CRH. Cleaning of CALIS was performed in CR1, a clean room located next to the WCV. Each component of CALIS was first cleaned with detergent and rinsed with high purity water. Then the pieces were pickled using a solution of 2% glycolic acid and 1% formic acid at a temperature between 80° and 90° C. Again, the components were rinsed with high purity water and then underwent passivation with a 4% solution of citric acid at 60° - 70° C. Finally, the components were rinsed with high purity water and then completely dried with compressed nitrogen. Once all parts were thoroughly dried, CALIS was partially assembled and then the components were double-bagged. The bagging allowed the pieces of CALIS to be transported from CR1, into Hall C, and then into CRH without becoming contaminated. Full assembly was completed inside CRH and CALIS was mounted on the gate valve on October 19, 2014.

Pressure and Leak Tightness Once installed on the gate valve in CRH, CALIS was tested for pressure stability and leak tightness. Prior to opening the gate valve, the "pump and purge" sequence described in Section 4.1 was performed. Then the assembly was given a slight over pressure relative to the pressure at the surface of the scintillator. To ensure the assembly could be rotated azimuthally without losing pressure, the clamp between the upper and lower

assemblies was loosened and the upper assembly was rotated several degrees in each direction. At no point in the rotation was there a pressure loss and the clamp was tightened. Then the gate valve was opened while the pressure inside CALIS was carefully monitored. Again, there was no pressure loss and CALIS was verified to be leak and pressure tight.

Light Tightness Before full operation of CALIS could commence, it was neccessary to verify that CALIS is light tight. In order to do this, the viewport cover was secured and a veto PMT close to the opening of the organ pipe inside the LSV was chosen to monitor any incoming light. The dark rate of the chosen PMT was recorded and the lights within CRH were turned off (except for a red flashlight). As the gate valve was opened, the PMT rate was carefully monitored. There was no increase in the PMT dark rate. Next, the clamp for azimuthal rotation was loosened and the upper assembly was rotated; again, there was no increase in the PMT dark rate. Finally, the lights in CRH were turned on and the upper assembly was rotated. No increase in the PMT dark rate was seen and CALIS was confirmed to be light tight.

Position Verification The PIG's first deployment into the LSV was done without a source. The veto PMTs were turned off to allow the CCD cameras installed inside the LSV to be utilized for Z-position and articulation verification. Also, the cover was left off of the viewport in order to monitor the movement of the PIG and cables. The PIG was lowered into the LSV and it's position monitored by taking pictures with the CCD cameras once it cleared the organ pipe, Figure 4.12. The PIG was lowered to its maximum position and then positioned at it nominal location near the center of the TPC active volume using information gathered from the testing phase. The source arm was articulated and then azimuthally rotated. As the PIG was rotated, the PMT rates were monitored to determine when the source holder was touching the TPC. As the source holder approached the TPC, the PMT rates would gradually increase until the rates leveled and would not increase any more. It was at this point that it was determined that the source holder had touched the TPC and was in position to begin taking data. At each position of the PIG, pictures were taken and the positions were consistent with expectations.

4.4   Calibration Campaigns

Multiple calibration campaigns have been carried out using CALIS. The first campaign occurred just after installation in late October, November 2014. This campaign has been the most extensive to date. Other campaigns have occurred with the most recent being in June 2016. The details of each campaign are given in the following sections.
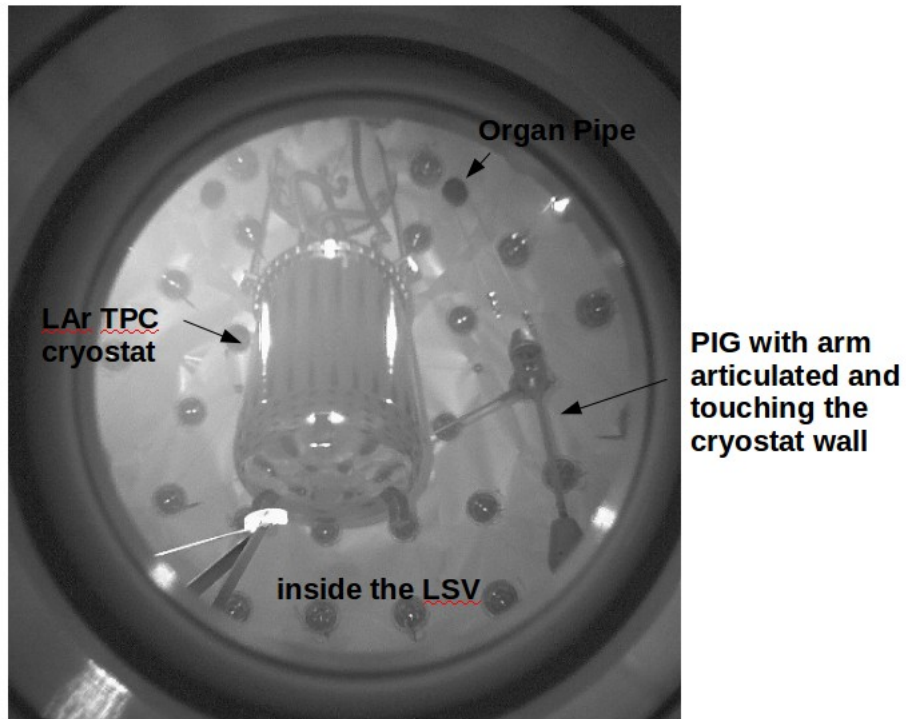
Figure 4.12: A picture of the PIG taken with the CCD cameras located inside the LSV, next to the cryostat.

October, November 2014 This was the first calibration campaign for DarkSide-50. At this time the TPC was filled with AAr and the LSV consisted of less than 0.1% TMB. Three gamma sources were deployed: ^{57}Co, ^{133}Ba, and ^{137}Cs. These sources, along with the internal source, ^{83m}Kr, cover the entire energy spectrum of ^{39}Ar. For each of the gamma sources, the drift field was varied to determine *in-situ* the energy response to drift field. Data was taken at 200 V/cm (the nominal drift field), 150 V/cm, 100 V/cm, and null field. In each case the source was placed next to the cryostat wall, in the center of the active volume of the TPC. A detailed description of the sources and the analyzed data from this campaign can be found in the following chapters and forms the basis for determining a global energy variable for DarkSide-50. Data was also taken above and below the central position as an independent check on the Z position of the source.

In addition to the gamma sources, two AmBe sources were deployed. The first AmBe source deployed had an activity of 2000 n/s and the second AmBe source had an activity of 10 n/s. For the 2000 n/s source, the rate was too high for the source to be placed directely against the cryostat wall. In this case the source had to be rotated away from the cryostat.

February 2015 Before this campaign took place, the concentration of TMB in the LSV was increased to 5%. For this campaign, a 10 n/s AmBe source was deployed. This campaign was primarily used for LSV studies. Data was taken with the source against the cryostat wall and away from the wall to compare the effects of cryostat shadowing for neutron detection.

August 2015 This was the first campaign to be undertaken with argon sourced from underground (UAr) with an external source. ^{22}Na was used with the goal of obtaining a high statistics set β^+ events for studying pulse shape discrimination in the TPC.

December 2015 A campaign with a AmC source occurred in December of 2015. This source was deployed for the purpose of measuring the neutron detection efficiency of the LSV. The source was created to avoid the correlated high energy gamma which accompanies the AmBe decay and would obscure the prompt thermaliztion signal of the neutron. Analysis of this data set is nearing completion and will be published soon.

June 2016 In June 2016, an AmBe source with an activity of 160 n/s was deployed. The goal of this campaign was to give a high statistics data sample of neutron events for the characterization of nuclear recoil pulse shape discrimination which is detailed extensively in [36].

CHAPTER 5
LIGHT YIELD AND SATURATION

The following chapter details light yield calculations for deployed gamma sources and the internal source, ^{83m}Kr, in addition to validation of a saturation correction variable for S1 and S2.

5.0.1 DS-50 Calibration Sources

^{83m}Kr decays in two steps producing first a 32.1 keV and then a 9.4 keV conversion electron. The signal seen in DarkSide-50 is a single peak at $\sim$327.6 pe with a combined energy of 41.5 keV. The two conversion electrons are seen as a single peak due to the timing of their emission. The half-life of ^{83m}Kr is 1.83 hours; it decays via the first electron emission of 32.1 keV, and the subsequent decay to the ground state via the second electron has a half-life of 154 ns, hence their inseparability in data. ^{57}Co has a half-life of 271.8 days. It decays via electron capture producing a 122 keV gamma with an intensity of 85.6% followed by a 14 keV gamma (9.16%), or in 10.68% of cases a 136 keV gamma is emitted to get to a stable state. ^{133}Ba decays via electron capture and has a half-life of 10.51 years. It emits a single gamma at 356 keV with an intensity of 62%. ^{137}Cs has a half-life of 30.17 years and undergoes beta decay to ^{133m}Ba which has a half-life of $\sim$153 sec and then 85.1% of ^{133m}Ba decays to ground state by emitting a gamma of 662 keV. These selected sources span the energy range of interest for electron recoils.

5.1 Light Yield

Light yield is an important variable for the DarkSide-50 TPC as it sets the energy threshold for WIMPs. The light yield is given as the number of detected photoelectrons per unit of energy, typically in keV. Light yield is calibrated by introducing a radioactive source into/near the detector and measuring the amount of light detected at the full absorption peak. DarkSide-50 uses an internal source, ^{83m}Kr mixed with argon, for full volume calibration and is the nominal source used to measure light yield in the TPC. Additional light yield measurements are done with external (to the TPC) gamma sources that cover a higher energy range. Data to be used for light yield measurements are taken at null electric field to allow for as much argon recombination as possible. Background runs, with the source absent, were also taken at null field. Background runs are used for a statistical background subtraction in order to more clearly see the full absorption peak.

For each of the sources, the full absorption peak was fit with a single gaussian function. In the case of ^{57}Co, it was also fitted with a single gaussian, but the fit range started at the very tip of the peak where the 122 keV gamma is expected to be, to reduce the effects from lower energy gammas. For these light yield calculations, only the 122 keV gamma of ^{57}Co is considered; a more
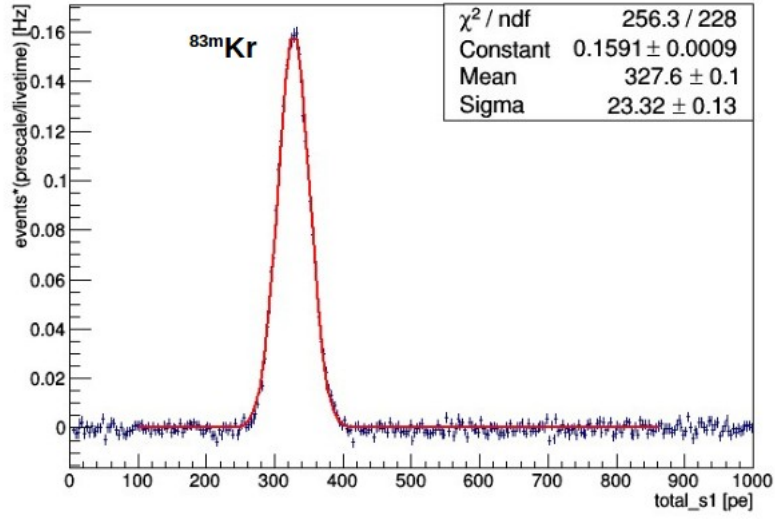
Figure 5.1: S1 distribution for ^{83m}Kr at null field with background statistically subtracted.
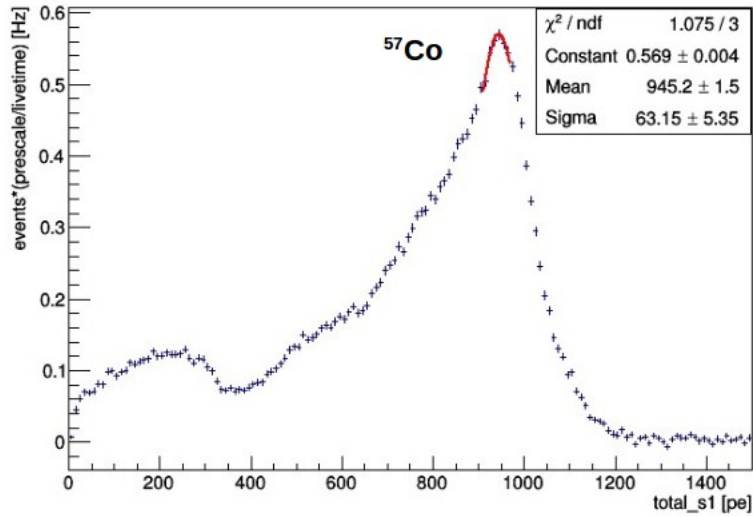
Figure 5.2: S1 distribution for ^{57}Co at null field with background statistically subtracted.

Isotope	Photoelectrons (pe)	Energy (keV)	Light Yield (pe/keV)
^{83m}Kr	327.6 ± 0.1	41.5	7.890 ± 0.002
^{57}Co	945.2 ± 1.5	122	7.750 ± 0.012
^{133}Ba	2869 ± 3.1	356	8.060 ± 0.009
^{137}Cs	5405 ± 3.4	662	8.160 ± 0.005

Table 5.1: Summary of Light Yield Measurements for the TPC at null field. There is an upward trend in the light yield except for ^{57}Co which is attributed to the greater stopping power for lower energy gammas.
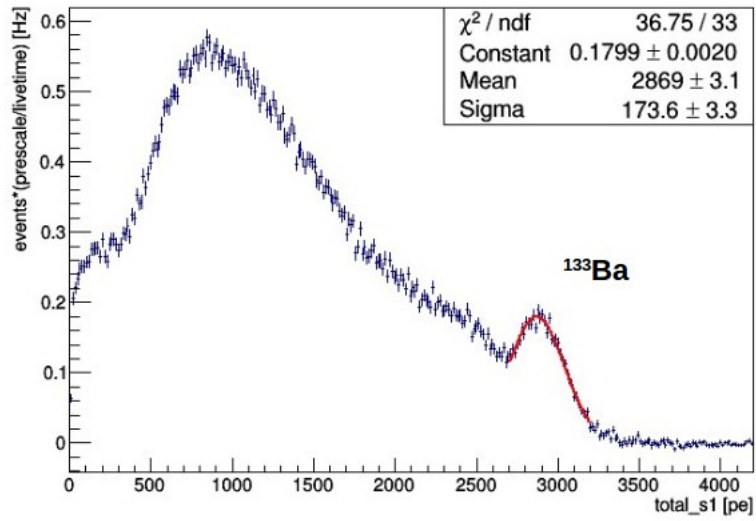
Figure 5.3: S1 distribution for ^{133}Ba at null field with background statistically subtracted.
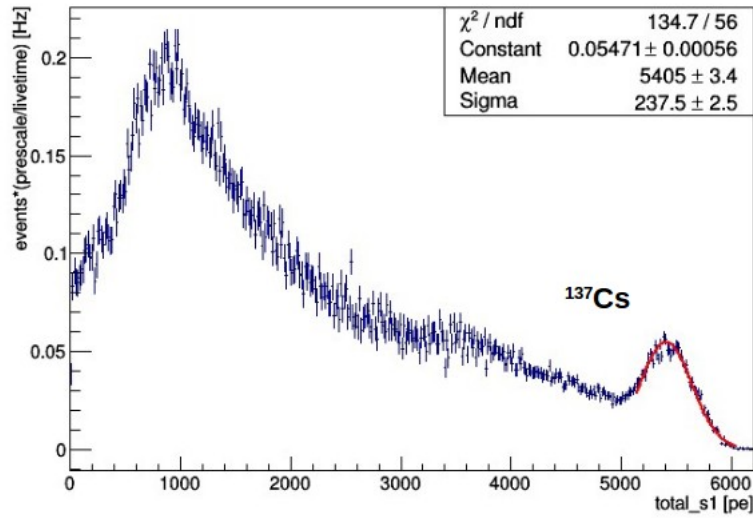
Figure 5.4: S1 distribution for ^{137}Cs at null field with background statistically subtracted.
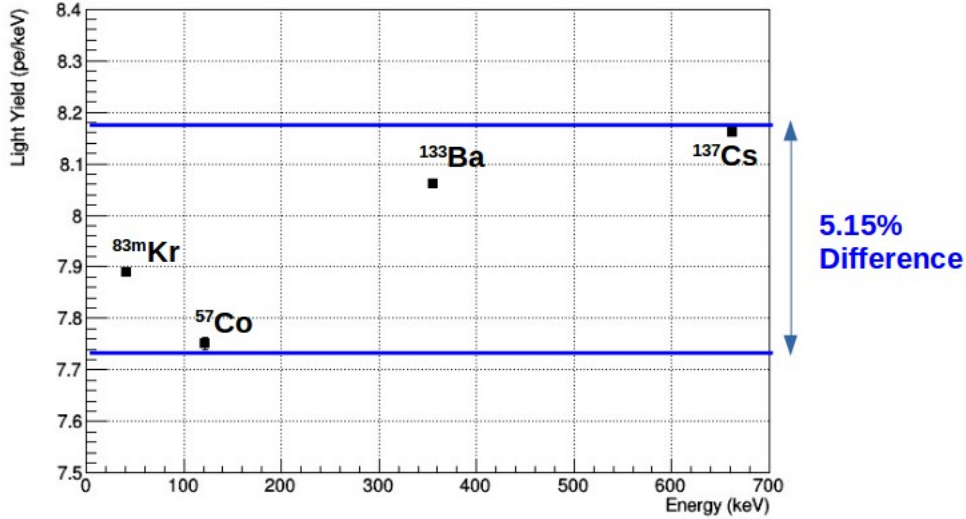
Figure 5.5: Light yield versus energy in DarkSide-50.

in depth study of the relationship between the 122 keV and 136 keV gammas for ^{57}Co is done in the next chapter. See Figures 5.1 through 5.4 for the S1 distributions and Table 5.1 for the light yield results.

The light yield as a function of energy is measured to be within 5% variation between 40 keV and 665 keV, as shown in Fig. 5.5.

5.2 Saturation Correction Variable

DarkSide-50 utilizes two types of digitizers for a total of ten digitizers. Five digitizers are 250 MHz 12 bit V1720 modules (known colloquially as V1720s) and the other five digitizers are 100 MHz 14 bit V1724 modules (V1724s). The V1720s receive the high gain (100 MHz bandwidth) and the V1724s receive the low gain (40 MHz bandwidth) analog signals [37]. For DarkSide-50, saturation effects must be taken into account when for events at higher energies. By using V1724 data, since it receives the low gain signal from the PMTs, one can construct a correction variable to account for ADC saturation. For S1 and S2, when saturation occurs, the number of photoelectrons detected is underestimated. Therefore, when S1 and S2 are corrected for saturation one would expect the number of photoelectrons to increase. A saturation correction variable was created, so that when saturation occurs, the correction from the V1724 data is applied and stored. If saturation does not occur, then the number of photoelectrons detected using the V1720s is stored within this correction variable. For every event detected, the number of pulses of that event is stored. The V1724 saturation correction variable works at the pulse level, i.e. each pulse is examined for saturation where the first pulse is considered S1 and the second pulse is S2.

This section will detail the work done for validating the V1724 saturation correction variable.

40
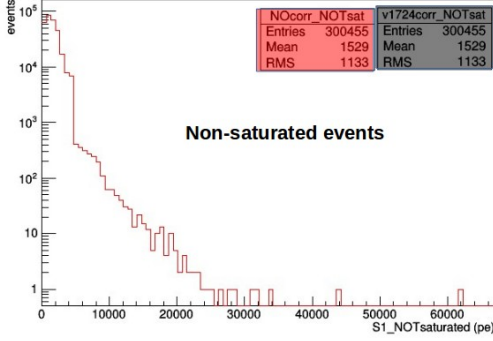
Figure 5.6: ^{137}Cs distribution of non-saturated events with V1724 corrected events in black and non-corrected events in red.
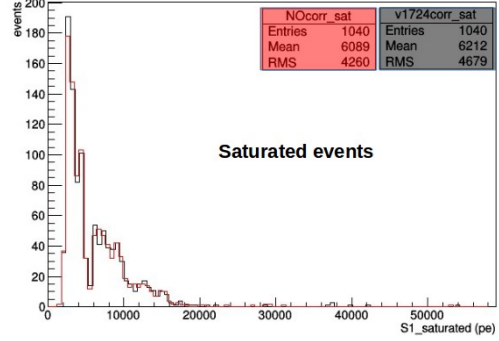
Figure 5.7: ^{137}Cs distribution of saturated events with V1724 corrected events in black and non-corrected events in red.

The goal of this study is to validate the V1724 correction used for saturated events. This is done by comparing non-corrected S1, S2 with corrected S1, S2. For S1, a saturation correction variable exists called S1 extended. We want to compare S1 extended and S1 V1724 corrected to measure how consistent the V1724 correction is with an existing S1 saturation correction variable. The same is done for S2 by comparing V1724 corrected S2 with the Paris groups ring S2 top variable.

5.2.1   S1

By looking at ^{137}Cs data taken in AAr, one expects the greatest amount of saturation to be seen since it is the highest energy source. For this data set, we look at DarkSide-50's nominal drift field of 200 V/cm since we will be considering S2 as well. Also, we considered data taken with UAr at 200 V/cm.

First, we must compare non-saturated S1 events in ^{137}Cs with and without the V1724 correction. From Fig. 5.6, one can see from the distributions that applying the V1724 correction shows no measurable difference in the mean, as expected. When comparing saturated events only, with and without the V1724 correction, there is a small upward shift in the mean (2%) when the correction is applied, Fig. 5.7.

Other collaborators have investigated solutions to the saturation problem. One such collaborator from FNAL developed a variable called S1 extended in order to account for S1 saturation. When validating the V1724 correction, a comparison was done between the existing S1 extended variable and the V1724 correction variable. The goal was to determine if the V1724 correction matched with the S1 extended variable ($S1_{ext}$). S1 extended is calculated as follows: if S1 is not saturated then S1 extended = S1 (also denoted as $S1_{noCorr}$). If S1 is saturated then

$$S1_{ext} = \frac{S1_{late}}{(1 - f90_{nonSat})} \tag{5.1}$$
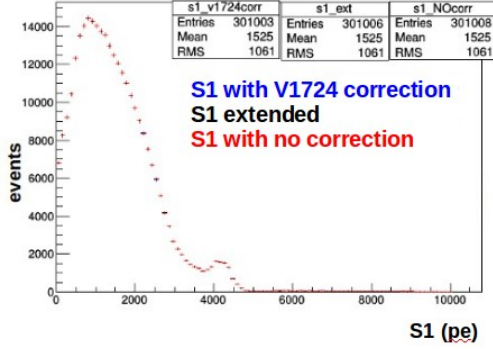
Figure 5.8: ^{137}Cs distribution of all events with S1 extended corrected events in black, S1 V1724 corrected in blue, and S1 with no correction applied in red.
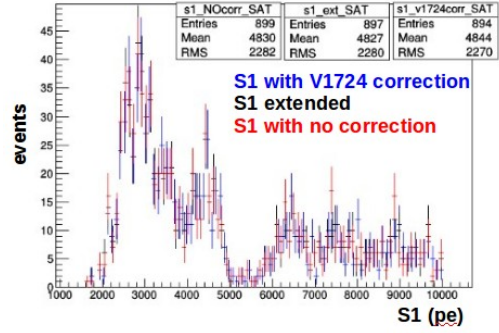
Figure 5.9: ^{137}Cs distributions of saturated events with S1 extended corrected events in black, S1 V1724 corrected in blue, and S1 with no correction applied in red.

where

$$S1_{late} = S1 \cdot (1 - f90) \tag{5.2}$$

and $f90_{nonSat}$ is the sum of prompt light for non-saturated channels divided by the sum of the total light for non-saturated channels. When calculating S1 extended, the assumption is made that when saturation occurs in S1, only one PMT channel will saturate and that channel is the maximum channel for the event. For this series of distributions, the ^{137}Cs data is confined to the range from 0 pe to 10000 pe for ease of comparison. Figures 5.8 and 5.9 show all three versions of S1: S1 with no correction (red), S1 with V1724 correction (blue), and S1 extended (black) for all S1 events and for saturated events only, respectively. Large saturation effects are not present in S1. The means of the distributions stay about the same no matter which correction is applied or if a correction is applied.

To see how the corrections directly compare, one can look at the differences of the corrections, Eq. 5.3 for saturated events only and at the fractional difference, Eq. 5.4 between S1 V1724 corrected and S1 extended.

$$\text{Difference of Correction} = \frac{(S1_{V1724corr} - S1_{noCorr}) - (S1_{ext} - S1_{noCorr})}{S1_{V1724corr} - S1_{NOcorr}} \tag{5.3}$$

$$\text{Fractional Difference with } S1_{ext} = \frac{S1_{V1724corr} - S1_{ext}}{S1_{V1724corr}} \tag{5.4}$$

$$\text{Fractional Difference with } S1_{noCorr} = \frac{S1_{V1724corr} - S1_{noCorr}}{S1_{V1724corr}} \tag{5.5}$$

Figures 5.10 and 5.11 show that on average the V1724 correction is more dominant and that the corrections agree within 0.8%, respectively. When one looks at the fractional difference between S1
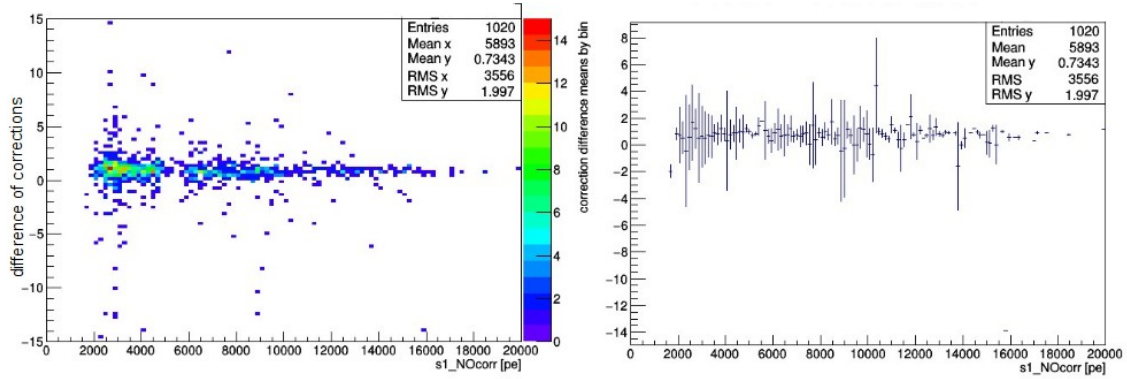
Figure 5.10: ^{137}Cs saturated events only looking at the differences in the corrections as a function of S1 with no correction (left). The right plot shows the mean of each bin of the left plot where the error bars represent the standard deviation in each bin.
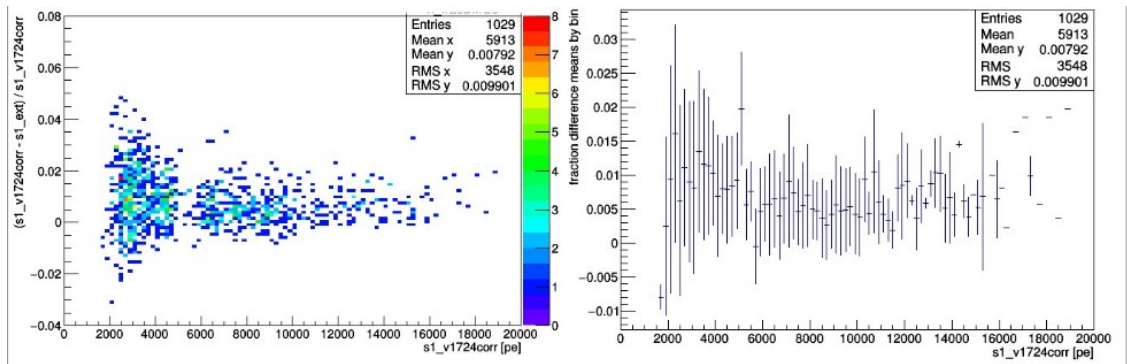
Figure 5.11: ^{137}Cs saturated events only looking at the fractional difference between S1 with V1724 correction and S1 extended (left). The right plot shows the mean of each bin of the left plot where the error bars represent the standard deviation in each bin.
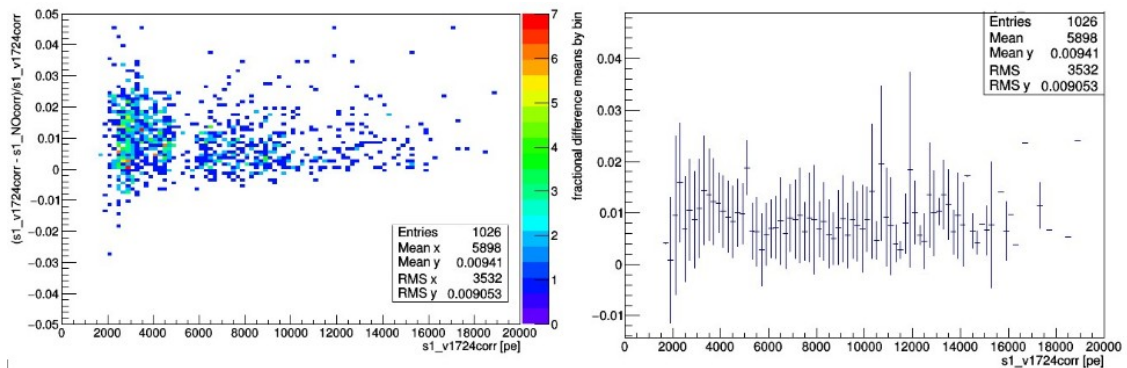
Figure 5.12: Fractional difference with no correction (Eq. 5.5) of ^{137}Cs saturated events. The right plot shows the mean of each bin of the left plot where the error bars represent the standard deviation in each bin.

43
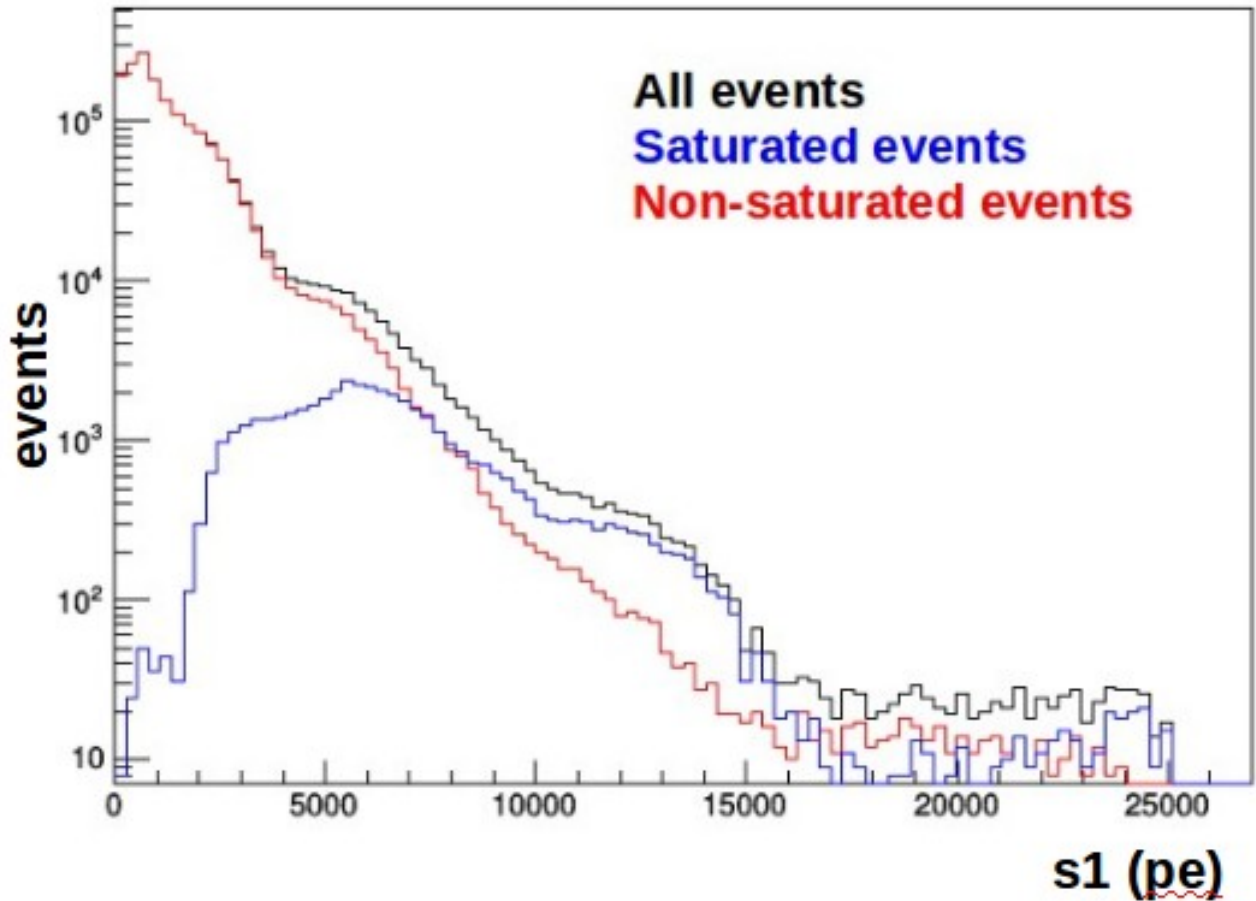
Figure 5.13: UAr spectrum at 200 V/cm for all events, saturated events, and non-saturated events.

V1724 corrected and S1 with no correction (Eq. 5.5), it is shown that the V1724 correction creates an upward shift in S1 that is flat across energy, see Fig. 5.12.

One can also look at UAr data at 200 V/cm to understand the relationship between the corrections. Looking at UAr data increases the energy range, allowing one to get a broader view of how the corrections effect the data. In Fig. 5.13, saturation becomes apparent $\sim$4000 pe and then begins to dominate the UAr spectrum $\sim$7500 pe.

In Figures 5.14, 5.15, and 5.16, the right hand plots show the mean of each bin from the left hand plot with the ^{137}Cs data overlaid in red. UAr data shows an upward turn of events at low S1 ($<$ 1000 pe) that is not present in ^{137}Cs. These events in UAr are the result of events being either very close the top PMTs or the bottom PMTs. Being that close to the PMTs results in saturation even at low S1. There are no saturated events with S1 $<$ 1000 pe in ^{137}Cs due to its location close to the detector equitorial plane where UAr is present throughout the volume of the TPC.

For S1, saturation effects are small; no matter which correction is applied the means of the
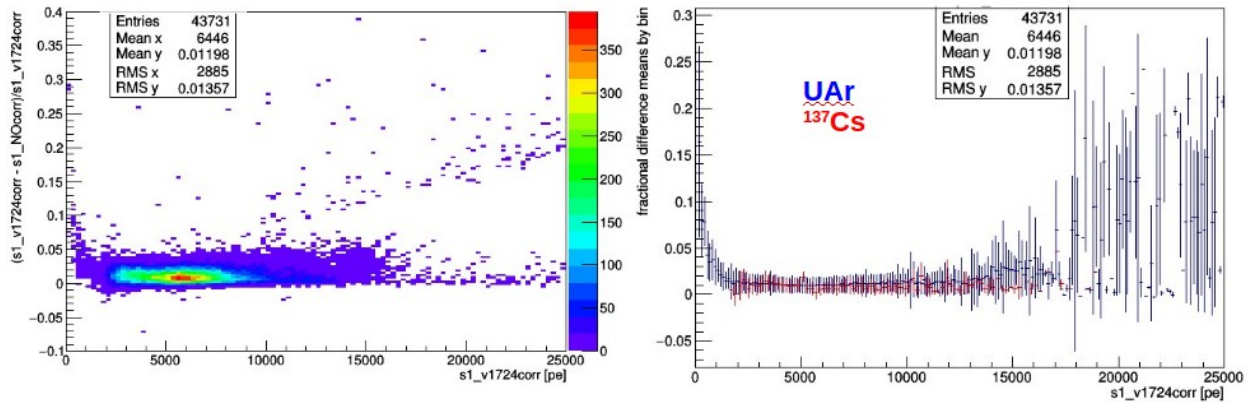
Figure 5.14: Fractional difference (Eq. 5.5) vs. S1 with V1724 correction. The V1724 correction is a 1.2% correction which is consistent with the ^{137}Cs data (1% correction).
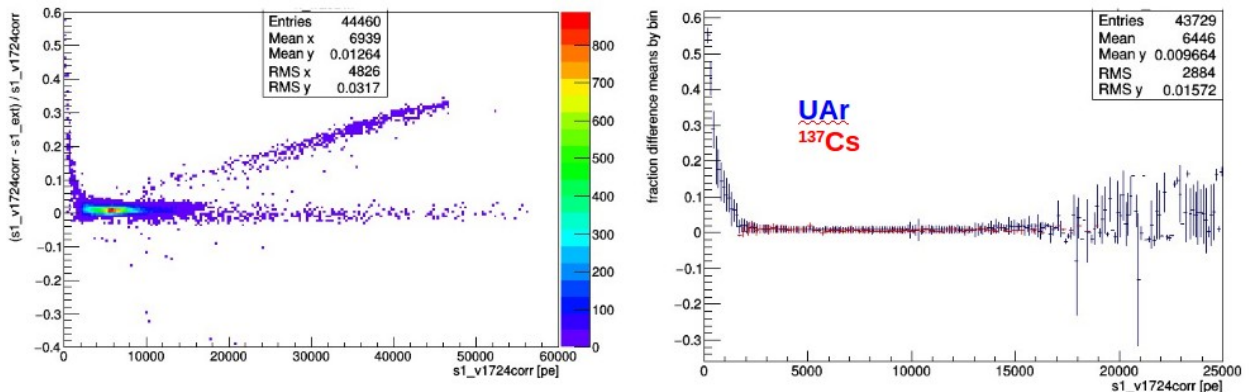
Figure 5.15: Fractional difference (Eq. 5.4) vs. S1 with V1724 correction. On average, the corrections V1724 and S1 extended agree within 1% (consisitent with ^{137}Cs where the corrections agreed within 0.8%).
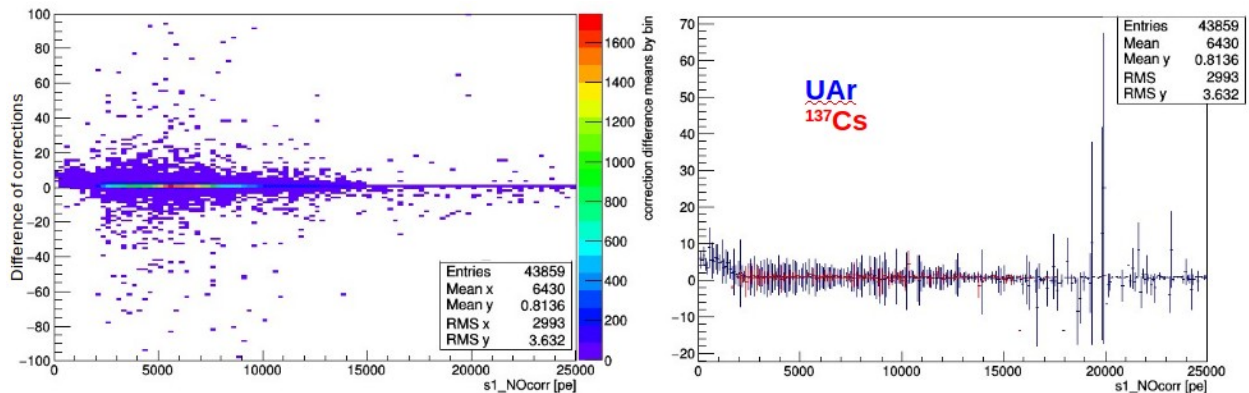
Figure 5.16: Difference of corrections (Eq. 5.3) vs. S1 with no correction. The V1724 correction is more corrective than S1 extended.
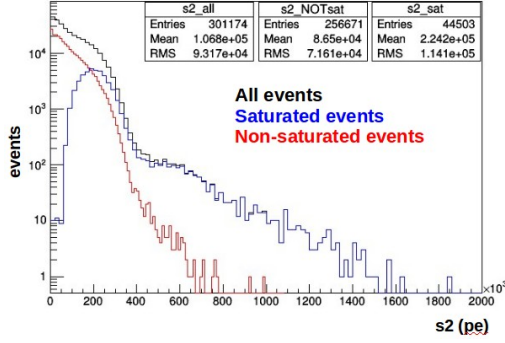
Figure 5.17: S2 events for ^{137}Cs. Saturated events are in blue and non-saturated events are in red. The black line is saturated and non-saturated events together.
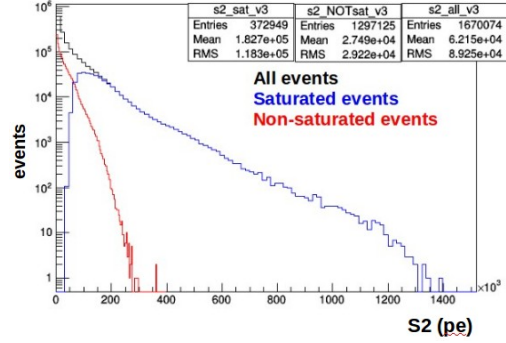
Figure 5.18: UAr S2 events.
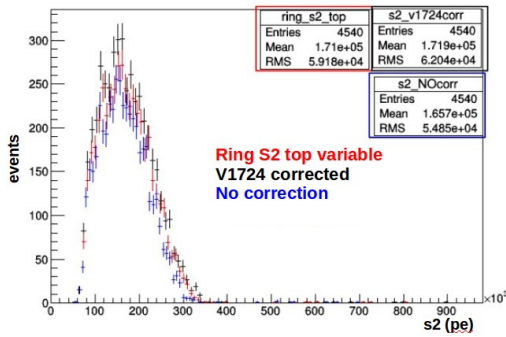
Figure 5.19: Saturated S2 events for ^{137}Cs with radius < 4 cm. The ring S2 top variable is red, V1724 corrected S2 is blue, and black is non-corrected events.
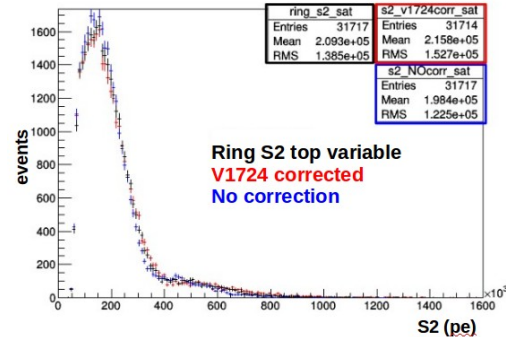
Figure 5.20: Saturated S2 events for UAr with radius < 4 cm. The ring S2 top variable is black, V1724 corrected S2 is red, and blue is non-corrected events.

distributions for UAr and ^{137}Cs remain stable. The V1724 correction is a 1.2% correction in S1. The correction gives an overall upward shift in the mean. S1 extended and V1724 correction differ by 1% with the V1724 correction having a greater effect than S1 extended.

5.2.2 S2

For the purpose of this study, we are only considering the secondary pulse as S2. As will be discussed in the next chapter, ^{137}Cs generates multiple scatters. But here, we are only looking at the first secondary pulse for both ^{137}Cs and for UAr. Similar to what was done for S1, the first step in looking at saturation for S2 is by comparing saturated and non-saturated events. Fig. 5.17 shows that saturated events dominate the spectrum above ~400,000 pe for ^{137}Cs and for UAr saturation completely dominates the spectrum above ~250,000 pe. Saturation plays a larger role in S2.

In an effort to study saturation, collaborators from Université Paris Diderot (known colloquially
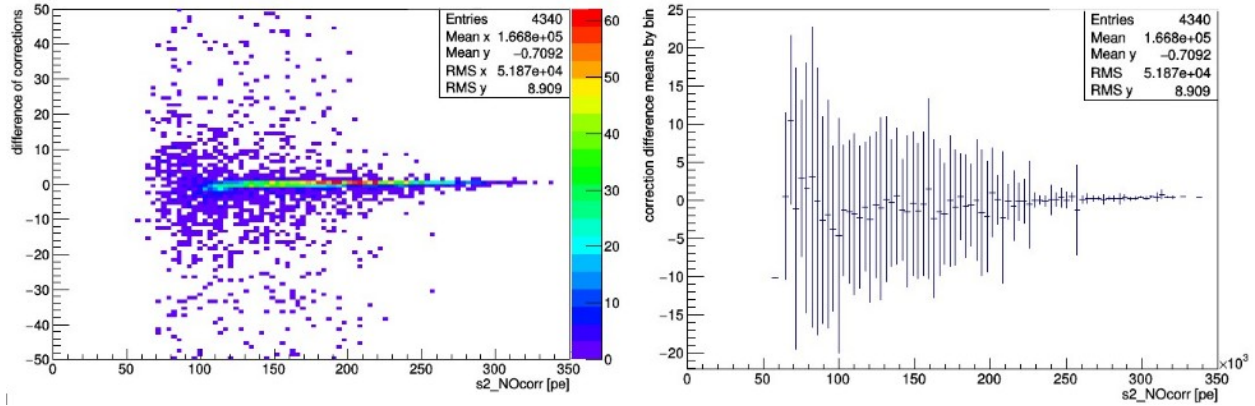
Figure 5.21: Difference in corrections for ^{137}Cs saturated S2 events with radii < 4 cm. The ring S2 top variable correction is larger than the V1724 correction.
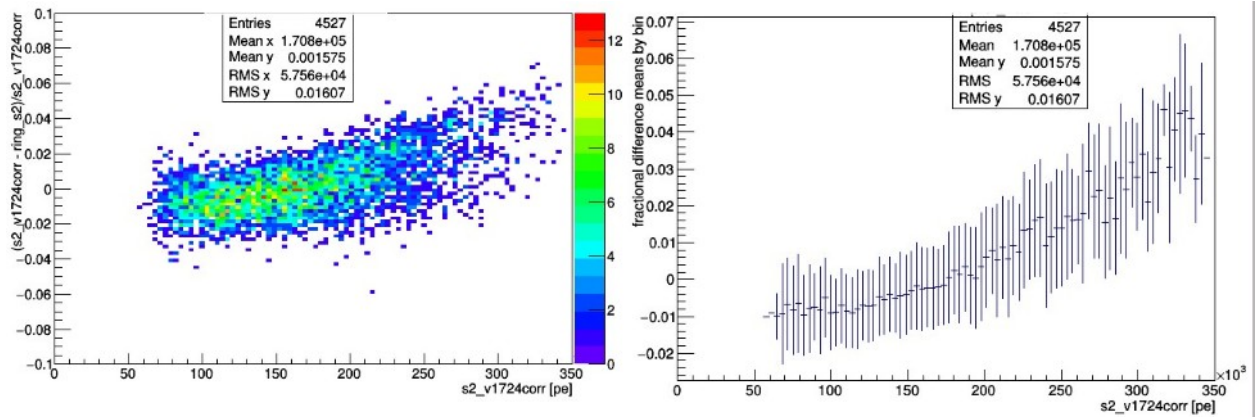
Figure 5.22: ^{137}Cs S2 saturated events with radii < 4 cm fractional difference between V1724 correction and ring S2 top variable.

as the Paris group), developed an S2 variable to avoid the saturation effect; it is known as the ring S2 top variable. The ring S2 top variable was developed by selecting events in the center of the detector (radius < 4 cm) to avoid saturation at the edge and to avoid radial corrections. Events were located in the center of the detector, while the S2 signal used to fill the variable was from the top PMTs on the edge of the detector only. As with S1 extended, one can compare the two different methods for dealing with S2 saturation, Fig. 5.19 and Fig. 5.20. There is a significant shift in the mean when either the V1724 correction is applied or the ring S2 top variable is used.

For ^{137}Cs S2 saturated events, on average, the ring S2 top variable is correcting more than the V1724 correction, Fig. 5.21. The S2 corrections agree within 0.2%; however, for low S2 the ring S2 top variable is the dominant correction. As S2 energy increases, the V1724 correction becomes more dominant, see Fig. 5.22. Fig. 5.23 shows that the V1724 correction for S2 is 2.7%, on average. The correction is not flat with energy for S2 events; as S2 increases the correction goes up to 10%.
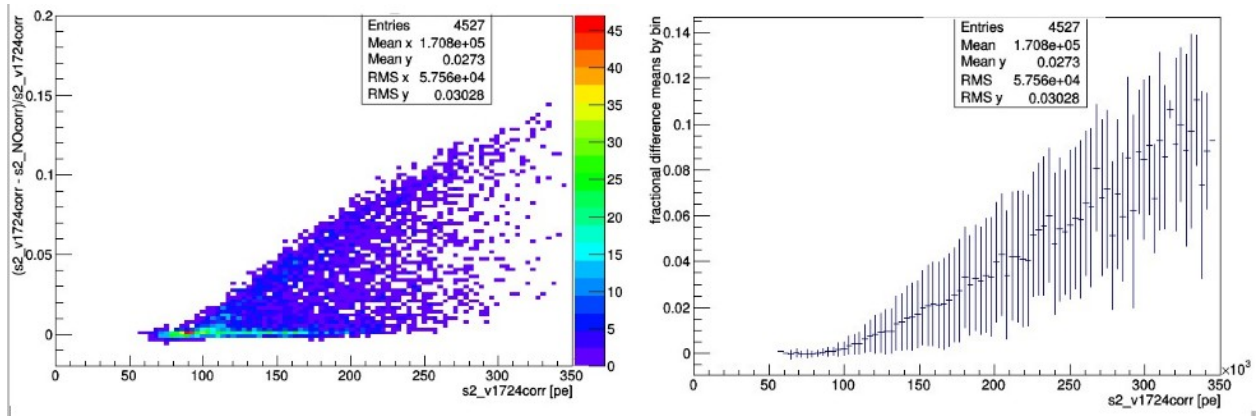
Figure 5.23: ^{137}Cs saturated events with radii < 4 cm fractional difference between V1724 correction and no correction.
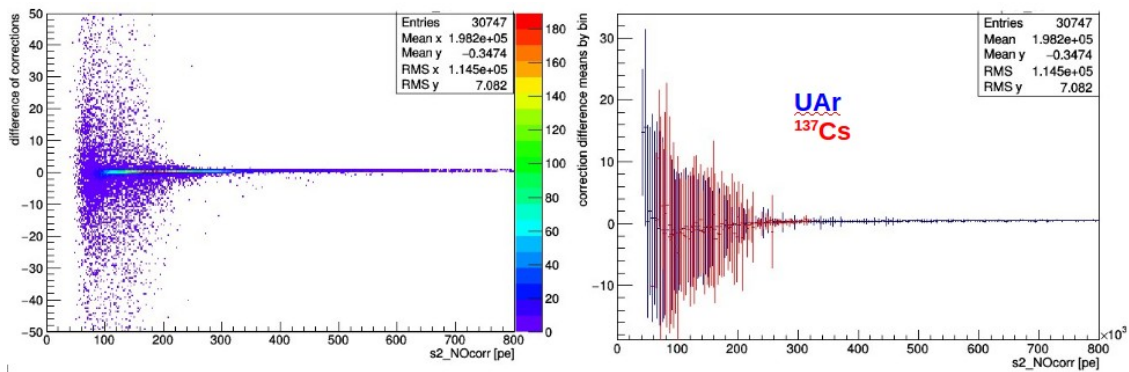
Figure 5.24: UAr S2 saturated events with radii < 4 cm difference of corrections between V1724 correction and the ring S2 top variable.
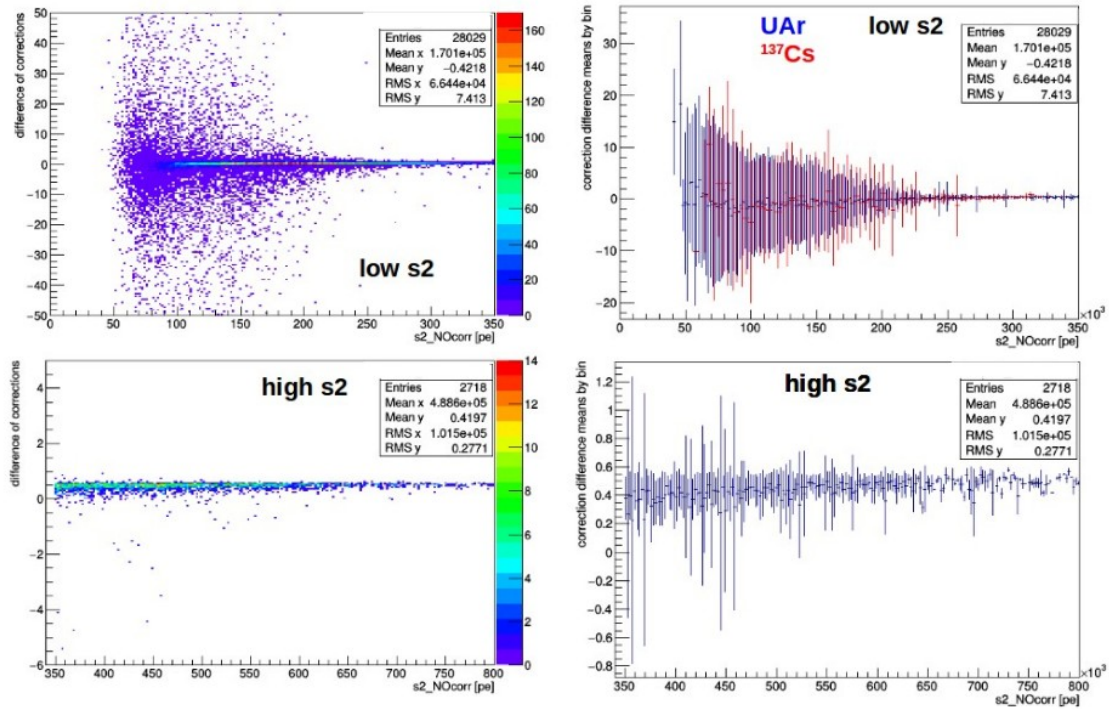
Figure 5.25: Difference of Corrections: Top left and right plots are low (< 350000 pe) S2 saturated events for UAr, bottom left and right plots are high (>350000 pe) S2 saturated events for UAr with ^{137}Cs overlaid on the top right plot.
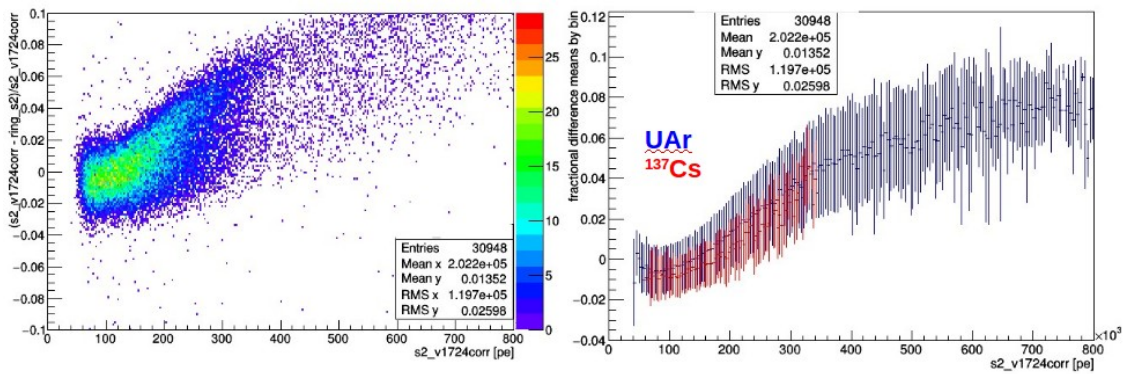
Figure 5.26: Fractional difference between the V1724 correction and ring S2 top events for UAr S2 saturated events with radii < 4 cm.
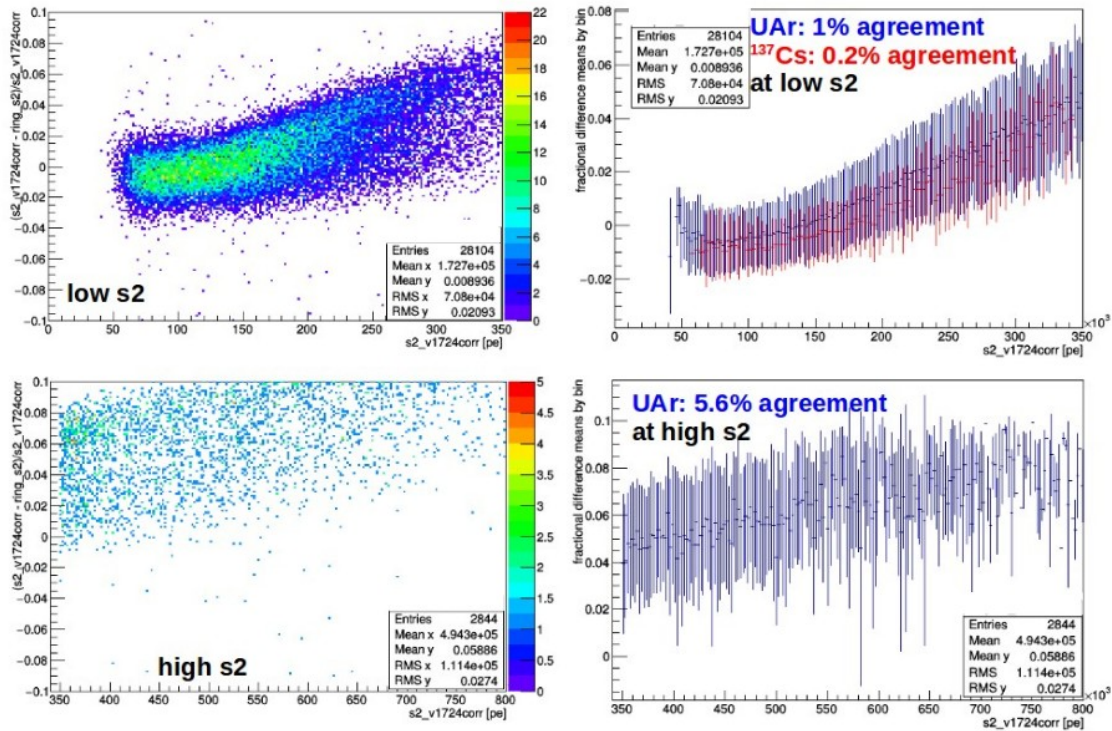
Figure 5.27: Fractional difference between the V1724 correction and ring S2 top events for UAr S2 saturated events. Top left and right plots are low (< 350000 pe) S2 saturated events for UAr, bottom left and right plots are high (>350000 pe) S2 saturated events for UAr with ^{137}Cs overlaid on the top right plot.
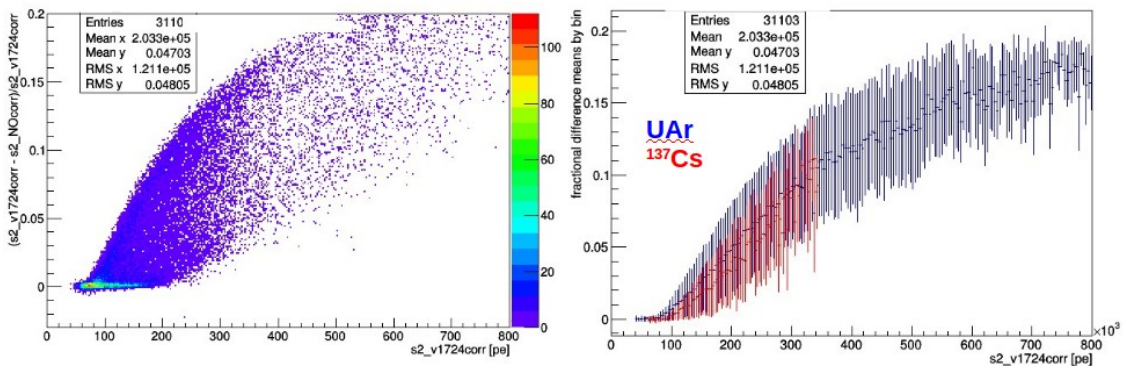
Figure 5.28: Fractional difference between the V1724 correction and non-corrected events for UAr S2 saturated events with radii < 4 cm.
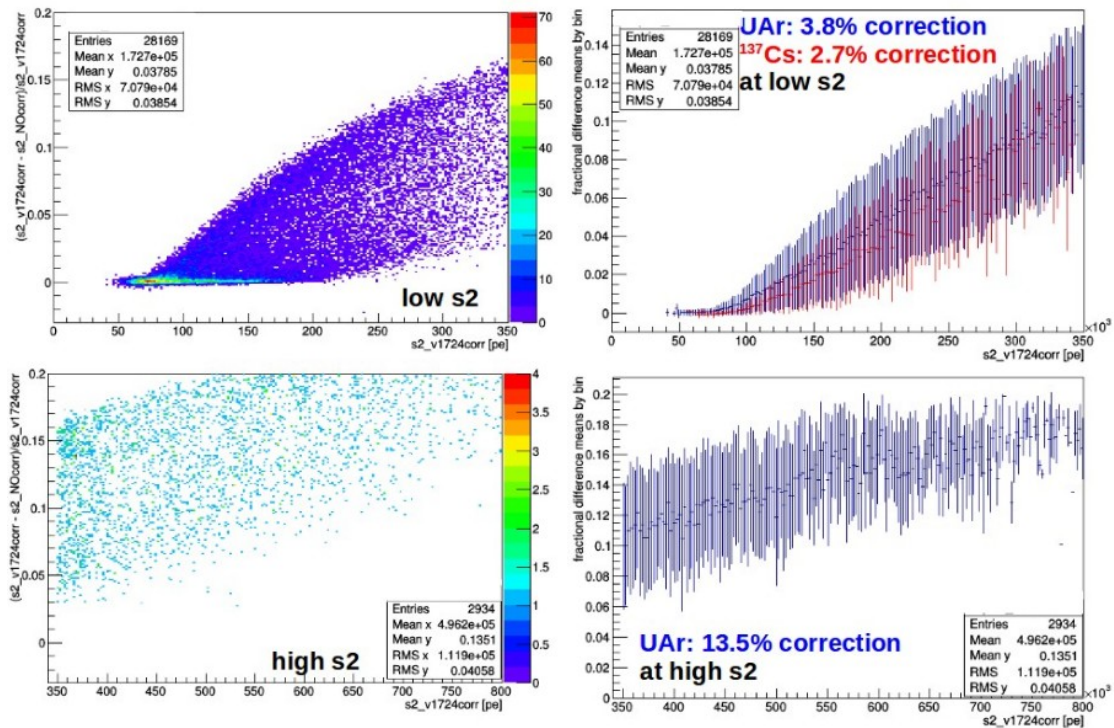
Figure 5.29: Fractional difference between the V1724 correction and non-corrected events for UAr S2 saturated events. Top left and right plots are low (< 350000 pe) S2 saturated events for UAr, bottom left and right plots are high (>350000 pe) S2 saturated events for UAr with ^{137}Cs overlaid on the top right plot.

Since the UAr spectrum goes up to 800×10^3 pe, one can split the spectrum in half and examine how the corrections change for low S2 $(< 350 \times 10^3)$ and for high S2 $(> 350 \times 10^3)$. For the full spectrum of UAr, on average, the ring S2 top variable is more corrective than the V1724 correction (Fig. 5.24). However, when you look at low S2 vs high S2, the ring S2 top variable is only more corrective at low S2. As S2 energy increases, the V1724 correction becomes more corrective which is consistent with ^{137}Cs (Fig. 5.25). The two corrections (V1724 and ring S2 top) agree within 1.4%, Fig. 5.26. At low S2, the correction agree within 1% and at high S2 they have a 5.6% agreement, Fig. 5.27. The V1724 correction is, on average, a 4.8% correction, but the amount of correction is strongly dependent on the energy of S2, see Fig. 5.28. Fig. 5.29 shows that at low S2, the V1724 correction is a 3.8% correction, but for high S2 can be a 13.5% correction (average) with a range up to 20%.

Overall, saturation effects are minimal in S1 and when the V1724 correction is applied there is an upward shift in the energy. For S2, saturation effects are more predominant and require a saturation correction in order to accumulate as much of the signal as possible. A correction for S2 is heavily dependent on the energy of S2, the V1724 correction can be as low as 3.8% for UAr (2.7% for ^{137}Cs), but can range up to 20% as S2 increases in UAr. In summary, the V1724 correction variable is an apt correction to apply to S1 and S2 as it is more corrective than S1 extended and, in general, more corrective than the ring S2 top variable.

The V1724 correction variable is validated and significant, especially for correcting S2. It will be utilized in the global energy variable construction, as it affects the energy calibration of the deployed sources in DarkSide-50.

CHAPTER 6
CONSTRUCTING A GLOBAL ENERGY VARIABLE

It is expected that WIMP interactions will deposit only a small fraction of energy in the LAr TPC and have a rate that falls off exponentially with respect to energy. Understanding the energy scale is important in WIMP detectors as it allows one to accurately reconstruct the event energy which correlates directly to understanding quantitatively the WIMP sensitivity. In this chapter, we focus on developing a combined energy variable based on the primary scintillation, S1, and the electroluminescence, S2, signals.

6.1   Energy Transfer Rehash

Following from Section 3.2, when a particle interacts in noble gases, it produces excited (excitons) and ionized (ions) atoms along with elastic recoils that eventually thermalize producing heat. Excitons can be produced directly along the interaction track and at the interaction site or through recombination of the ionized atoms. The excitons will then decay through the formation of an excited dimer, producing UV photons. The total number of photons, N_{ph}, produced can be written as

$$N_{ph} = aN_{ex} + brN_i. \tag{6.1}$$

where a, b are the efficiencies for direct excitons and recombined ions to produce scintillation photons (for argon a $\sim$ b $\sim$ 1, [28]) and r is the fraction of ions that recombine. In general, r depends on the electric field. In the presence of an electric field, some of the ions will escape recombination. The amount of charge that survives recombination (the number of photons produced by ionization), n_e, is defined as

$$n_e \equiv (1 - r)N_i. \tag{6.2}$$

In the event of full recombination, $r = 1$, one can define $W_{ph} \equiv E/N_{ph}$ or as in Eq. 3.3; this is the average energy required to produce a single scintillation photon either from excitation or ionization. Then it follows that Eq. 6.1 becomes

$$\frac{E}{W_{ph}} = N_{ex} + N_i \tag{6.3}$$

which can be rearranged as

$$E = W_{ph} \left[N_{ex} + N_i + rN_i - rN_i \right]$$

$$= W_{ph} \left[\left(\frac{N_{ex}}{N_i} + r \right) N_i + (1-r)N_i \right]$$

$$= W_{ph}(n_\gamma + n_e) \tag{6.4}$$

$$= \frac{W}{1 + N_{ex}/N_i} (n_\gamma + n_e)$$

where the definition of W_{ph} from Eq. 3.3 has been substituted in (remembering that W is the average energy required to produce an electron ion pair) and

$$n_\gamma \equiv (N_{ex}/N_i + r) N_i \tag{6.5}$$

is the number of photons produced both by direct excitations and recombining electrons. For liquid argon, $N_{ex}/N_i \sim 0.21$ [28]. Eq. 6.4 directly shows the fundamental property of the model; the energy is calculated by taking into account both n_e and n_γ. It is insensitive to the number of electrons that do recombine - each one will decrease n_e while, on average, increasing n_γ by the same amount. With Eq. 6.4 it is possible to compare single and multiple scatter events. Using an energy variable that is dependent only on the number of excitons can lead to underestimating the energy of multi-scatter events since recombination is a function of energy. A reliable estimator for the energy of a multiple scatter events is crucial for liquid noble detectors as these detectors frequently use γ-ray sources for calibrations. γ-rays above 100 keV frequently undergo multiple interactions since the radiation length is of the order of a centimeter.

With Eq. 6.4 one can construct a global energy variable which is independent from recombination effects due to both multiple scatters and the applied electric field. Defining

$$\epsilon_1 \equiv S1/n_\gamma \tag{6.6}$$

$$\epsilon_2 \equiv S2/n_e \tag{6.7}$$

as exciton and charge gain, respectively, where S1 and S2 are the primary and secondary scintillation signals, Eq. 6.4 then becomes (with $f \equiv N_{ex}/N_i$)

$$E = \frac{W}{1+f} \left[\frac{S1}{\epsilon_1} + \frac{S2}{\epsilon_2} \right]. \tag{6.8}$$

6.2 Event Selection and Corrections

As dicussed in previous sections (Sec. 4.4 and 5.0.1), DarkSide-50 uses ^{83m}Kr, ^{57}Co, ^{133}Ba, and ^{137}Cs deployed in atmospheric argon (AAr) for electron recoil calibrations (see Table 6.1 for a

Source	Decay Process	Half-Life	Energy (keV)	Intensity
^{83m}Kr	internal conversion	1.83 h	9.4, 32.1	100, 1.12
^{57}Co	γ emission	271.74 d	122, 136	85.6, 10.68
^{133}Ba	γ emission	10.52 y	356	62.05
^{137}Cs	γ emission	30.04 y	662	85.1

Table 6.1: Properties of the calibration sources: both internal (^{83m}Kr) and external (^{57}Co, ^{133}Ba, and ^{137}Cs) sources.

Drift Field	Min drift time (μs)	Max drift time (μs)
200 V/cm	10	363.3
150 V/cm	12.44	451.86
100 V/cm	17.42	632.98
50 V/cm	33.49	1216.5

Table 6.2: Maximum and minimum drift times required for events for each of the different drift times. An event must have a drift time between these bounds in order to pass.

summary of all the calibration sources used for this analysis with their respective decay processes and energies). For multiple scatter events, it is expected to have a single S1 since it is not possible to resolve in time two interactions of the photon with DarkSide-50's electronics. However, it is expected to have multiple pulses for electroluminescence. Since the drift velocity is of the order of 1 mm/μs, the time between two S2 signals can be as long as $\sim$ 60 μs. Total S2 is then the sum of all secondary pulses that match the requirements stated below.

For S1, an integration time window of 7 μs is used to identify the value of the pulse and S2 uses a 30 μs integration window. However, for multiple scatter events such as those used in this analysis, the corresponding pulse for S1 or S2 can exceed the usual fixed integration window which leads to an underestimation of the size of the signals. For this analysis, a different metric had to be used. Instead of using a fixed integration window, the size of each pulse is defined as the integral from the start of the pulse until its end as determined by the pulse finder algorithm.

Applied Cuts: Basic event quality cuts are applied; each event must pass all of the following:

1. Number of channels (PMTs) present = 38. Removes events in which one or more of the front-end boards in the DAQ were not working properly.

2. Baseline is found. Removes events which have large fluctuation in electronic noise.

3. Livetime + Inhibit time $\geq 1.35 \times 10^{-3}$ sec. Removes re-trigger on residual signal of previous event.

4. Livetime < 1 sec (for a single event).

5. Number of pulses > 1 (in order to account for multiple scatters in addition to single scatters)

6. S1 starts within correct trigger window

7. Total f90 > 0.05 (event not triggered on S2)

8. Drift time within bounds for respective drift fields (See Table 6.2). Removes events close to the top or bottom PMTs and accounts for events in the volume of the TPC.

Additionally for S2, the secondary pulse must have an f90 < 0.04 and the number of photoelectrons must be > 30. For ^{83m}Kr, the data used is from the February 2015 campaign to make use of the 50 V/cm drift field. This data was taken without the use of the V1724 digitizers; therefore, no V1724 correction is applied. In lieu of this correction and since ^{83m}Kr are not multi-scatter events, the regular S1 and S2 saturation cuts were applied. Also, the single scatter cut was applied: there must be only two pulses in the event or in the case of three pulses, the third pulse must be an S3 (S2 echo). To be considered an S2 echo, the time difference between the 2nd and 3rd pulse must be within 372 μs to 400 μs because it is a reflection (echo) of S2 from the bottom PMT ring.

Corrections Due to saturation effects present in S1 and S2, the two signals each utilized the V1724 correction variable discussed in Sec. 5.2. In addition to the V1724 correction, S1 requires a correction in z. Since it is not possible to resolve multiple S1s, the top/bottom asymmetry (TBA) correction is used; TBA gives an average z position for the event. For S2, each secondary pulse is corrected for its x, y position and drift time.

6.3   Fitting Full-Absorption Energy Peaks

In order to extract excitation and ionization yields for use in the energy variable analysis (discussed in the following section, Sec. 6.5), the full-absorption peak must be fitted as the energy variable relies on a mono-energetic value of S1 and S2. The full-absorption peaks for ^{83m}Kr, ^{133}Ba, and ^{137}Cs were each fit with a gaussian plus first degree polynomial for S1. The purpose of the addition of the first degree polynomial was to encapsulate the fact that the peaks were sitting on top of underlying data. For S2, events were selected that corresponded to its S1 counterpart in/near the full-absorption peak. This was done by requiring that an S2's S1 counterpart had to have a value between the mean $\pm 1.5\sigma$ in order for the S2 to be counted. The mean and σ were taken from the fit of the S1 full absorption peak. The S2 distribution was fit using a single gaussian function.

For ^{57}Co, the fitting of the full-absorption peak was modified in order to account for the 136 keV γ. In the decay of ^{57}Co, 122 keV and 136 keV γs are emitted. Therefore, to fit S1 a sum of two gaussians (one for each γ) was used as the fit function. Similar to what was done in [22] for the fit, the means of the gaussians were fixed to the ratio of energies and the intensities of the two γs were fixed to the number of events under each peak (see Eq. 6.9 and Eq. 6.10). In selecting S2 events in/near the full-absorption peaks for ^{57}Co, a different metric was chosen to account for the

excess of compton scattering seen in the spectrum. In this case, the lower bound was chosen to be the weighted mean - 0.25σ and the upper bound was the weighted mean + 1.8σ. These bounds were chosen to roughly coincide with the bounds from the S1 fit. The S2 distribution was fit with the sum of two gaussian functions due to the presence of the 122 keV and 136 keV γs. A note on how the choice of these bounds effects the S2 is discussed in Sec. 6.4.

$$\frac{N122(\text{events under 122 keV peak})}{N136(\text{events under 136 keV peak})} = \frac{122 \text{ keV } \gamma \text{ intensity}}{136 \text{ keV } \gamma \text{ intensity}} \tag{6.9}$$

$$\frac{\text{Mean of 122 keV peak}}{\text{Mean of 136 keV peak}} = \frac{\text{Energy of 122 keV } \gamma}{\text{Energy of 136 keV } \gamma} \tag{6.10}$$

The mean S1 value is determined with a weighted mean where the weight is the number of events under each peak, since the S1 distribution was fit with the sum of two gaussians and it resulted in values for both the 122 keV γ and the 136 keV γ. The same is done for the S2 mean. See Eq. 6.11:

$$\text{weighted S1 mean} = \frac{(\text{Nevents}_{122} * \text{mean}_{122}) + (\text{Nevents}_{136} * \text{mean}_{136})}{\text{Nevents}_{122} + \text{Nevents}_{136}} \tag{6.11}$$

Drift Field	S1 mean [pe]	S1 N events	S1 σ
200 V/cm	790 ± 6.9, 897 ± 14	9.5 ± 0.8, 1.0 ± 0.067	70.0 ± 6.5, 110 ± 30
150 V/cm	818 ± 17, 929 ± 22	10.0 ± 0.9, 1.017 ± 0.084	68.6 ± 5.3, 100 ± 30
100 V/cm	880.0 ± 2.3, 979 ± 31	9.0 ± 0.3, 1.0 ± 0.066	60.0 ± 6.5, 80 ± 46
Null	1007.2 ± 1.8, 1122 ± 3.4	11.8 ± 0.2, 0.808 ± 0.081	44.7 ± 5.7, 55.0 ± 8.0

Table 6.3: Summary of ^{57}Co S1 values from the fits at different drift fields; the values are given for the 122 keV γ and the 136 keV γ respectively.

Drift Field	S2 mean [pe]	S2 N events
200 V/cm	$3.251 \times 10^4 \pm 120$, $4.218 \times 10^4 \pm 390$	0.1255 ± 0.0044, 0.083 ± 0.003
150 V/cm	$2.857 \times 10^4 \pm 90$, $3.759 \times 10^4 \pm 270$	0.1457 ± 0.0040, 0.097 ± 0.003
100 V/cm	$2.446 \times 10^4 \pm 130$, $3.248 \times 10^4 \pm 390$	0.1732 ± 0.0069, 0.098 ± 0.005

Table 6.4: Summary of ^{57}Co S2 values from the fits at different drift fields; the values are given for the 122 keV γ and the 136 keV γ respectively.

Source	S1 mean [pe]	S1 σ	S2 mean [pe]
^{83m}Kr	302.9 ± 0.6	20.5 ± 0.7	10350 ± 10
^{133}Ba	2407 ± 7.9	97 ± 8	127100 ± 500
^{137}Cs	4297 ± 5.0	139 ± 4	293300 ± 500

Table 6.5: Summary of ^{83m}Kr, ^{133}Ba, and ^{137}Cs S1 and S2 values at 200 V/cm.

Source	S1 mean [pe]	S1 σ	S2 mean [pe]
^{133}Ba	2510 ± 3	89 ± 4	111900 ± 200
^{137}Cs	4502 ± 5	133 ± 4	264900 ± 500

Table 6.6: Summary of ^{133}Ba and ^{137}Cs S1 and S2 values at 150 V/cm.

Source	S1 mean [pe]	S1 σ	S2 mean [pe]
^{83m}Kr	314 ± 1	21 ± 1	7130 ± 10
^{133}Ba	2637 ± 4	78 ± 5	94370 ± 300
^{137}Cs	4860 ± 3	134 ± 2	215000 ± 300
^{83m}Kr @ 50 V/cm	322.3 ± 0.6	21.0 ± 0.7	5520 ± 5

Table 6.7: Summary of ^{83m}Kr, ^{133}Ba, and ^{137}Cs S1 and S2 values at 100 V/cm. The S1 and S2 values for ^{83m}Kr at 50 V/cm are in the last line of the table.

Source	S1 mean [pe]
^{83m}Kr	337.4 ± 0.8
^{133}Ba	3027 ± 1
^{137}Cs	5629 ± 1

Table 6.8: Summary of ^{83m}Kr, ^{133}Ba, and ^{137}Cs S1 values at null field.

The results of the fits of S1 and S2 can be found in Figures 6.1, 6.2, 6.3, and 6.4 with a summary of the of the S1 and S2 values in Tables 6.3, 6.4, 6.5, 6.6, and 6.8. The values referenced in the aforementioned tables are only those pertinent to the calculation of the global energy variable through the fitting of their respective Doke plots, explained in the following section. The null field fits are included for completeness. Due to the null field data lacking a S2, they are not used in the extraction of the excitation and ionization fields. ^{57}Co, ^{133}Ba, and ^{137}Cs each have data taken at 200 V/cm, 150 V/cm, 100 V/cm, and null fields. For S1 and S2, the source data underwent a statistical background subtraction to make the full-absorption peaks more clear and easier to fit. ^{83m}Kr did not undergo a statistical background subtraction due to the source being internal to the

TPC and because of a lack of background data taken at the time of the campaign run. The lack of background data was not an oversight as the ^{83m}Kr full-absorption peak is easily seen on top of any backgrounds and all studies can be completed without a statistical background subtraction. ^{83m}Kr drift fields are 200 V/cm, 100 V/cm, 50 V/cm, and null.

6.4   A Note on Systematic Uncertainty in S2

S2 events are chosen to have an energy in the vicinity of the full-absorption peak by requiring that each S2 have a S1 counterpart within the mean $\pm$ 1.5σ of the S1 fit. This value was used for all sources at all drift fields except for ^{57}Co. To understand how the choice of the bounds effected the S2 mean, a study was done whereby the bounds were symmetrically varied for ^{83m}Kr, ^{133}Ba, and ^{137}Cs. The bounds chosen were mean $\pm$ 0.5σ, mean $\pm$ 1.0σ, mean $\pm$ 1.5σ, and mean $\pm$ 2.0σ. For ^{57}Co, the bounds were asymmetrically varied; the upper bound was kept constant while the lower bound varied and then the lower bound was kept constant while the upper bound varied. Upper bounds chosen for ^{57}Co with the lower bound kept constant at mean - 0.25σ were: mean + 1.5σ, mean + 1.8σ, mean + 2.2σ, and mean + 2.5σ. Lower bounds chosen with the upper bound kept constant at mean + 1.8σ were: mean - 0.0σ, mean - 0.25σ, mean - 1.0σ, and mean - 1.5σ. In every case, the resulting S2 distribution was fit and the mean was extracted. The results of the varying bounds for the 200 V/cm drift field can be found in Figures 6.5 and 6.6. The other drift fields can be found in Appendix A. A summary of the means of the fits for each source at 200 V/cm for all sigma bound variations can be found in Table 6.9 and for ^{57}Co all drift fields and all sigma bound variations can be found in Tables 6.10 and 6.11. Summaries for 150 V/cm, 100 V/cm, and 50 V/cm are found in Tables A.1 and A.2. In these tables, the headers for each column denote the low and high S1 sigma bounds used to select S2 events.

The selection of which bounds to use has no adverse affect on S2; it does not matter what bounds are chosen, the means of S2 remain consistent even at different drift fields. There is no noticeable shift in the spectra in the positive or negative direction. The only noticeable difference in the spectra from the choice of the bounds is the number of events that end up in the S2 distribution.

Source	$\pm 0.5\sigma$	$\pm 1.0\sigma$	$\pm 1.5\sigma$	$\pm 2.0\sigma$
^{83m}Kr	10410 ± 20	10400 ± 10	10350 ± 10	10310 ± 10
^{133}Ba	127400 ± 600	128500 ± 500	127100 ± 500	126100 ± 500
^{137}Cs	296300 ± 700	294600 ± 600	293300 ± 500	291600 ± 500

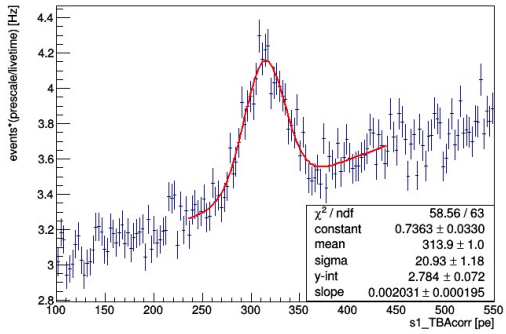Table 6.9: Summary of ^{83m}Kr, ^{133}Ba, and ^{137}Cs S2 means at 200 V/cm for the various S1 sigma bounds used to select S2 events.
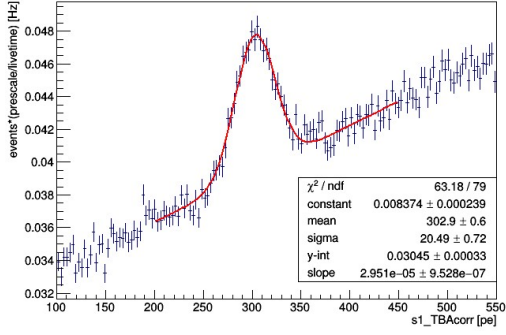
(a) ⁸³ᵐKr S1 at 200 V/cm.
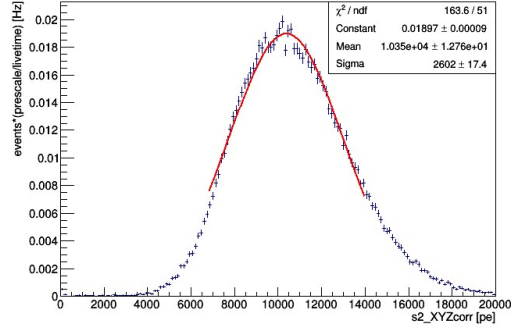
(b) ⁸³ᵐKr S2 at 200 V/cm.

(c) ⁸³ᵐKr S1 at 100 V/cm.
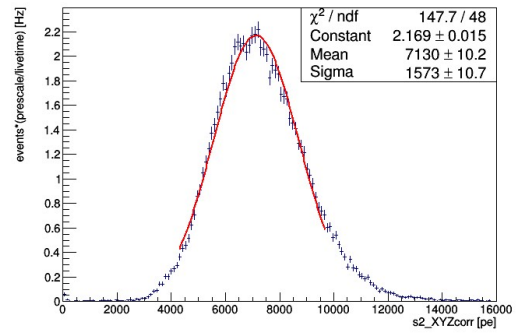
(d) ⁸³ᵐKr S2 at 100 V/cm.
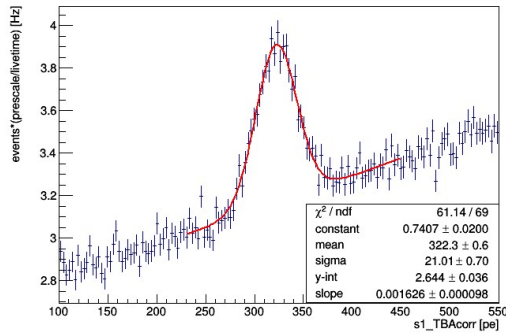
(e) ⁸³ᵐKr S1 at 50 V/cm.
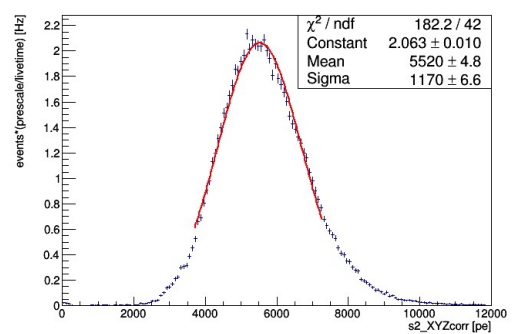
(f) ⁸³ᵐKr S2 at 50 V/cm.
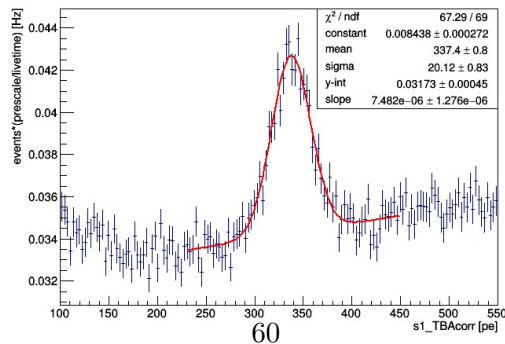
(g) ⁸³ᵐKr S1 at null field.

Figure 6.1: ⁸³ᵐKr fitted distributions for S1 and S2 for all drift fields.
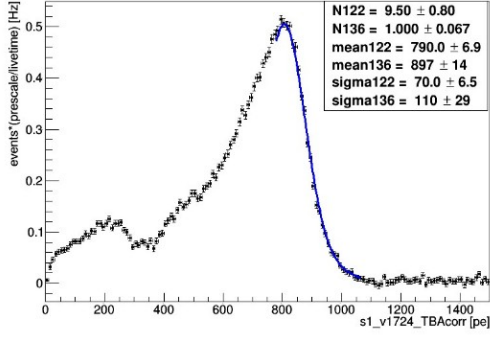
(a) ^{57}Co S1 at 200 V/cm.
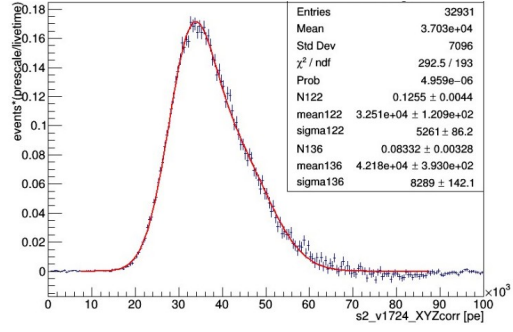
(b) ^{57}Co S2 at 200 V/cm.
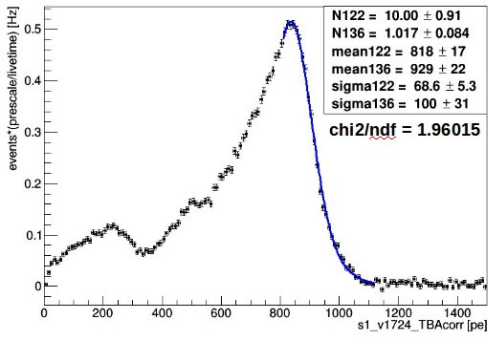
(c) ^{57}Co S1 at 150 V/cm.
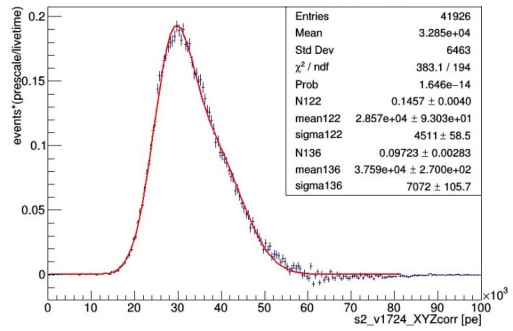
(d) ^{57}Co S2 at 150 V/cm.
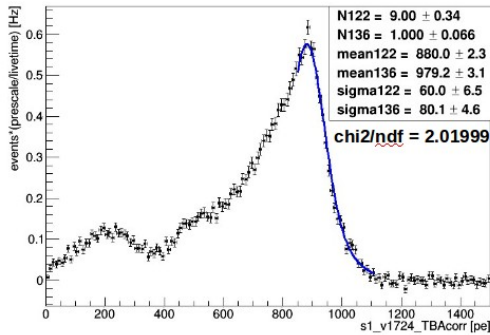
(e) ^{57}Co S1 at 100 V/cm.

(f) ^{57}Co S2 at 100 V/cm.

61
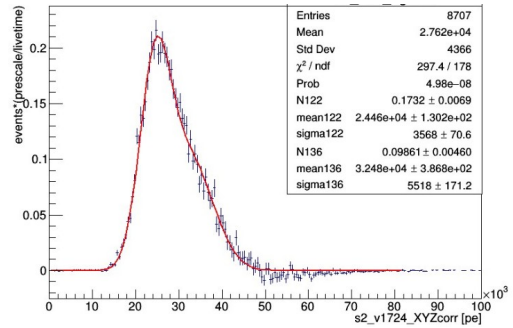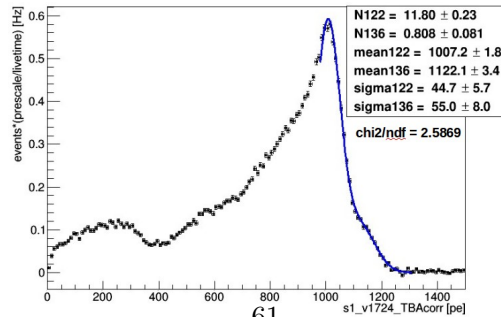
(g) ^{57}Co S1 at null field.

Figure 6.2: ^{57}Co fitted distributions for S1 and S2 for all drift fields.
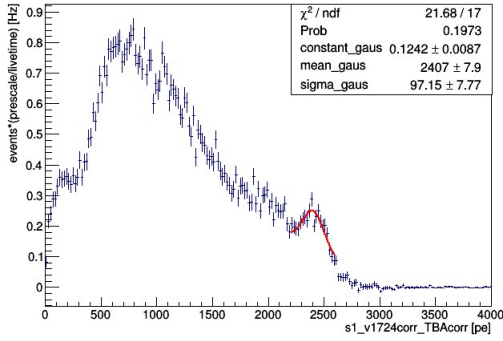
(a) ^{133}Ba S1 at 200 V/cm.
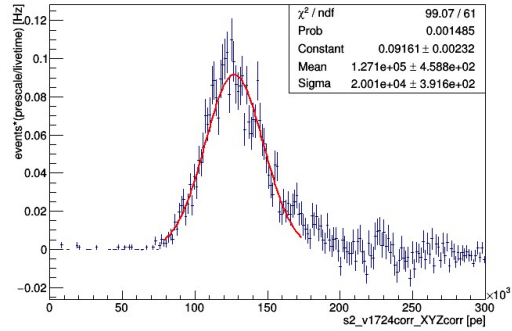
(b) ^{133}Ba S2 at 200 V/cm.
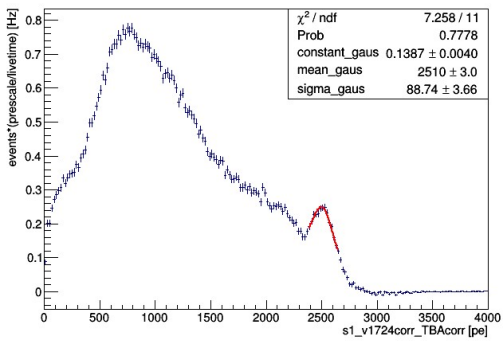
(c) ^{133}Ba S1 at 150 V/cm.
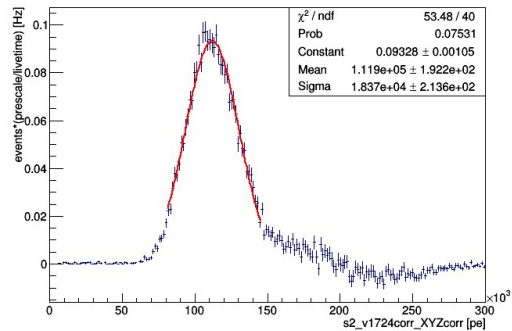
(d) ^{133}Ba S2 at 150 V/cm.
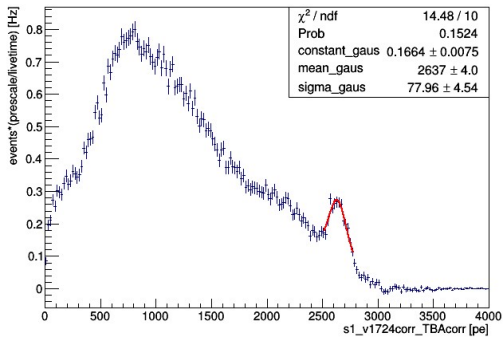
(e) ^{133}Ba S1 at 100 V/cm.
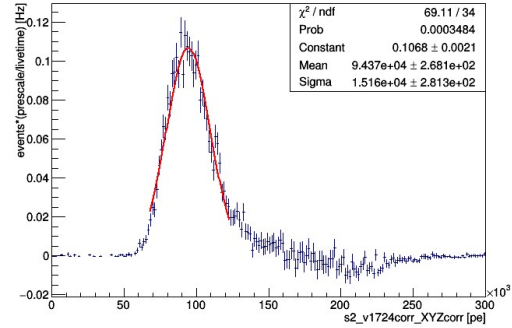
(f) ^{133}Ba S2 at 100 V/cm.
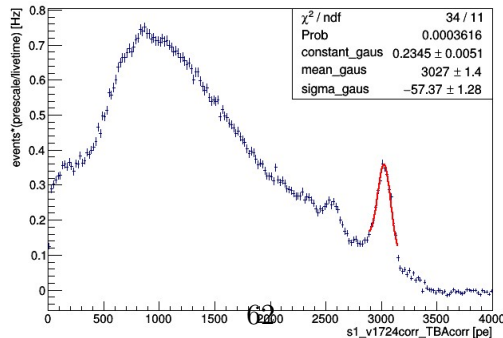
(g) ^{133}Ba S1 at null field.

Figure 6.3: ^{133}Ba fitted distributions for S1 and S2 for all drift fields.
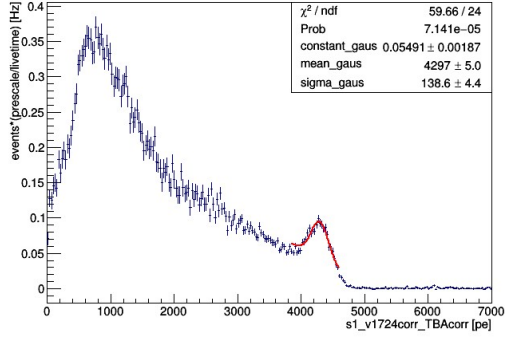
(a) ^{137}Cs S1 at 200 V/cm.
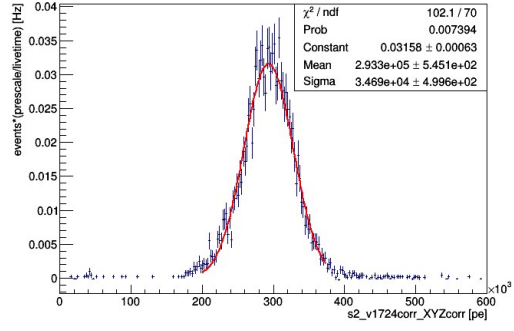
(b) ^{137}Cs S2 at 200 V/cm.
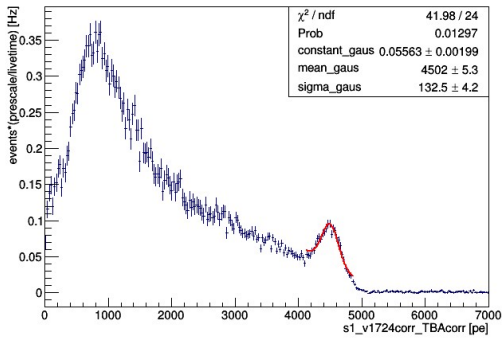
(c) ^{137}Cs S1 at 150 V/cm.
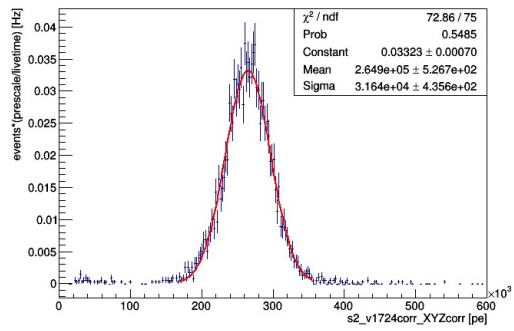
(d) ^{137}Cs S2 at 150 V/cm.
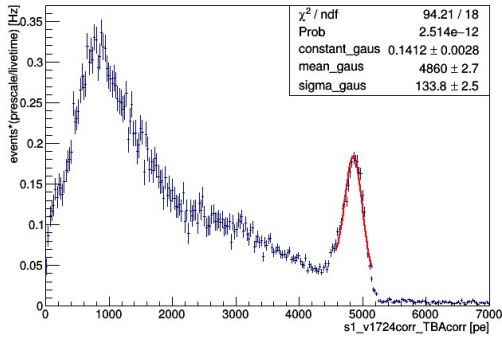
(e) ^{137}Cs S1 at 100 V/cm.
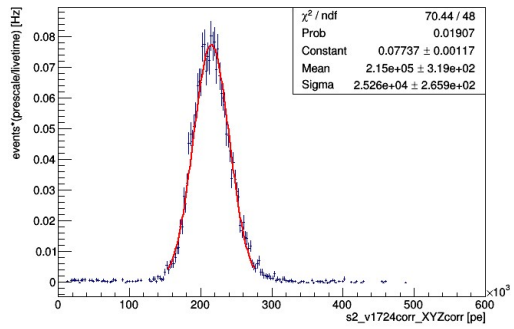
(f) ^{137}Cs S2 at 100 V/cm.
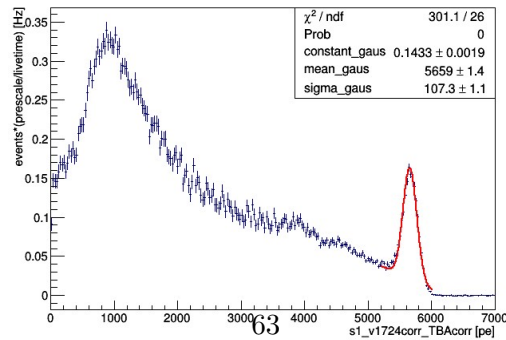
(g) ^{57}Cs S1 at null field.

Figure 6.4: ^{137}Cs fitted distributions for S1 and S2 for all drift fields.
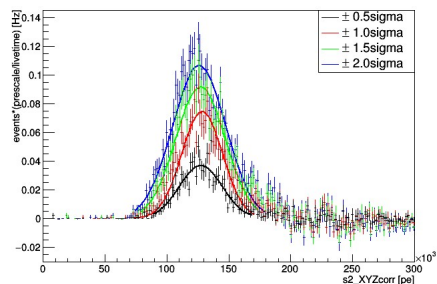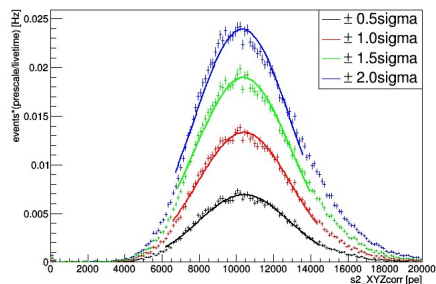
(a) ^{83m}Kr S2 at 200 V/cm with varied $\pm\sigma$ bounds.

(b) ^{133}Ba S2 at 200 V/cm with varied $\pm\sigma$ bounds.
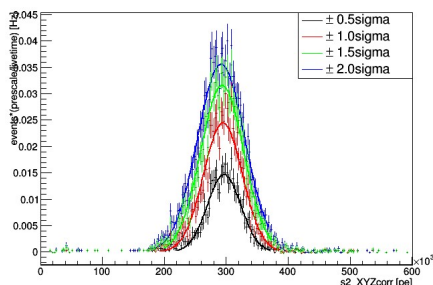
(c) ^{137}Cs S2 at 200 V/cm with varied $\pm\sigma$ bounds.

Figure 6.5: ^{83m}Kr, ^{133}Ba, and ^{137}Cs fitted S2 distributions with varied $\pm\sigma$ bounds: $\pm$ 0.5 σ, $\pm$ 1.0σ, $\pm$ 1.5σ, and $\pm$ 2.0σ.
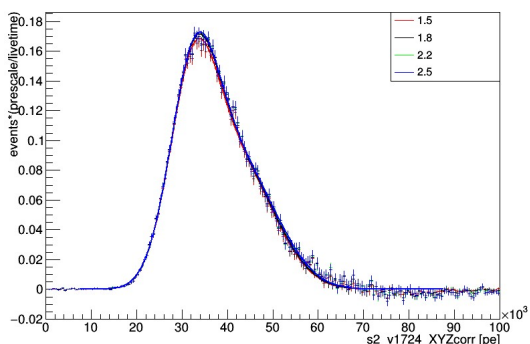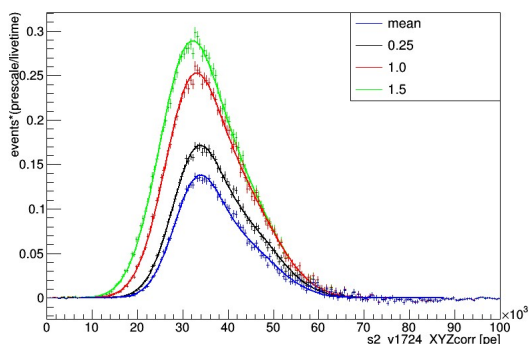
(a) ^{57}Co S2 at 200 V/cm with varied lower σ bounds, upper bound constant at mean $+$ 1.8σ.

(b) ^{57}Co S2 at 200 V/cm with varied upper σ bounds, lower bound constant at mean $-$ 0.25σ.

Figure 6.6: ^{57}Co S2 at 200 V/cm with varied bounds. Lower bound variations: mean $-$ 0.0σ, mean $-$ 0.25σ, mean $-$ 1.0σ, and mean $-$ 1.5σ with upper bound kept constant at mean $+$ 1.8σ. Upper bounds variations: mean $+$ 1.5σ, mean $+$ 1.8σ, mean $+$ 2.2σ, and mean $+$ 2.5σ with lower bound kept constant at mean $-$ 0.25σ.

Drift Field	-0.0σ	-0.25σ	-1.0σ	-1.5σ
200 V/cm	36300 ± 200	36400 ± 200	35300 ± 200	34300 ± 300
150 V/cm	32200 ± 200	32200 ± 100	31200 ± 100	30300 ± 200
100 V/cm	27300 ± 200	27400 ± 200	26900 ± 200	26400 ± 200

Table 6.10: Summary of ^{57}Co S2 means at each of the drift fields when the low bound on σ is varied with keeping the high bound constant at $+1.8\sigma$.

Drift Field	$+1.5\sigma$	$+1.8\sigma$	$+2.2\sigma$	$+2.5\sigma$
200 V/cm	36300 ± 200	36400 ± 200	36400 ± 200	36500 ± 200
150 V/cm	32100 ± 100	32200 ± 100	32200 ± 100	32300 ± 100
100 V/cm	27300 ± 200	27400 ± 200	27400 ± 200	27400 ± 200

Table 6.11: Summary of ^{57}Co S2 means at each of the drift fields when the high bound on σ is varied with keeping the low bound constant at -0.25σ.

6.5 Extraction of Excitation and Ionization Yields

After fitting the full-absorption peak in S1 and the resulting peak for S2, one can extract the excitation and ionization yields for DarkSide-50 by constructing Doke [28] plots for the various sources. Mean values of S1 and S2 are calculated for each source and drift field and these data points are then scaled by their source energy, in order to compare all the sources together. If the model for deposition of energy, discussed in Sec. 6.1, holds then the data obtained for different drift fields at a specific source energy should line up in the S2/E vs S1/E plane. A linear fit is performed in this plane for each of the different sources according to

$$\frac{S2}{E} = \frac{\epsilon_2(1+f)}{W} - \frac{\epsilon_2}{\epsilon_1}\frac{S1}{E}. \tag{6.12}$$

which is a rearrangement of Eq. 6.8. From the fit of the Doke plots, one extracts ϵ_1 and ϵ_2. Figure 6.7 shows an example of the results of the fit for ^{133}Ba with the results of all sources summarized in Table 6.12. The individual Doke plots for ^{83m}Kr, ^{57}Co, and ^{137}Cs can be found in Appendix B.

In Fig.6.8, one can see that the sources do not line up as expected. It seems that the Doke model presented is, perhaps, too simple to account for all variations in DarkSide-50. Null field data is especially problematic as the points are too far out of alignment with other drift fields for them to even be fit. One possible explanation for the null field results, proposed by M.Wada in [38], is that there is quenching of the energy in electron recoils which for this study was not considered. Strictly from the fits of S2/E vs S1/E, the ϵ_1 from ^{57}Co, ^{133}Ba, and ^{137}Cs are consistent with each other. One should keep in mind that ^{83m}Kr is an internal source, while the others are external to
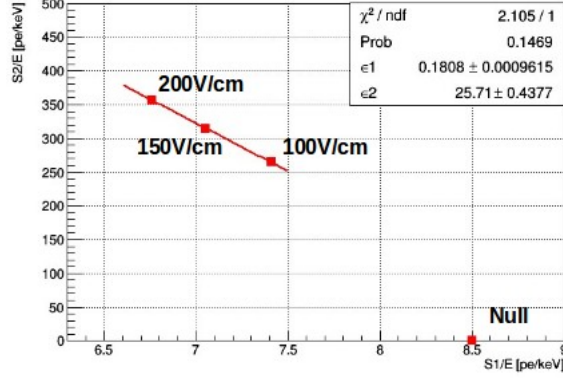
Figure 6.7: Doke plot (S2/E vs S1/E) for ^{133}Ba.

Source	ϵ_1 [pe/exc]	ϵ_2 [pe/e]
^{83m}Kr	0.160 ± 0.002	41 ± 4
^{57}Co	0.190 ± 0.004	18 ± 1
^{133}Ba	0.1800 ± 0.001	25.7 ± 0.4
^{137}Cs	0.1900 ± 0.0001	26.28 ± 0.02

Table 6.12: Summary of ϵ_1 and ϵ_2 for all sources extracted from the fits of S2/E vs S1/E.

the TPC. In addition, events from external sources are close to the wall of the TPC around the equatorial plane, while ^{83m}Kr events are uniformly distributed throughout the volume and thus, close to the PMTs as well. For ϵ_2, ^{133}Ba and ^{137}Cs are consistent, with ϵ_2 from ^{57}Co not too far off, but none agree within statistical errors. To define a global energy variable one obtains average ϵ_1 and ϵ_2 values from the fits:

$$\epsilon_1 = 0.18 \pm 0.01 \tag{6.13}$$

$$\epsilon_2 = 27 \pm 9. \tag{6.14}$$
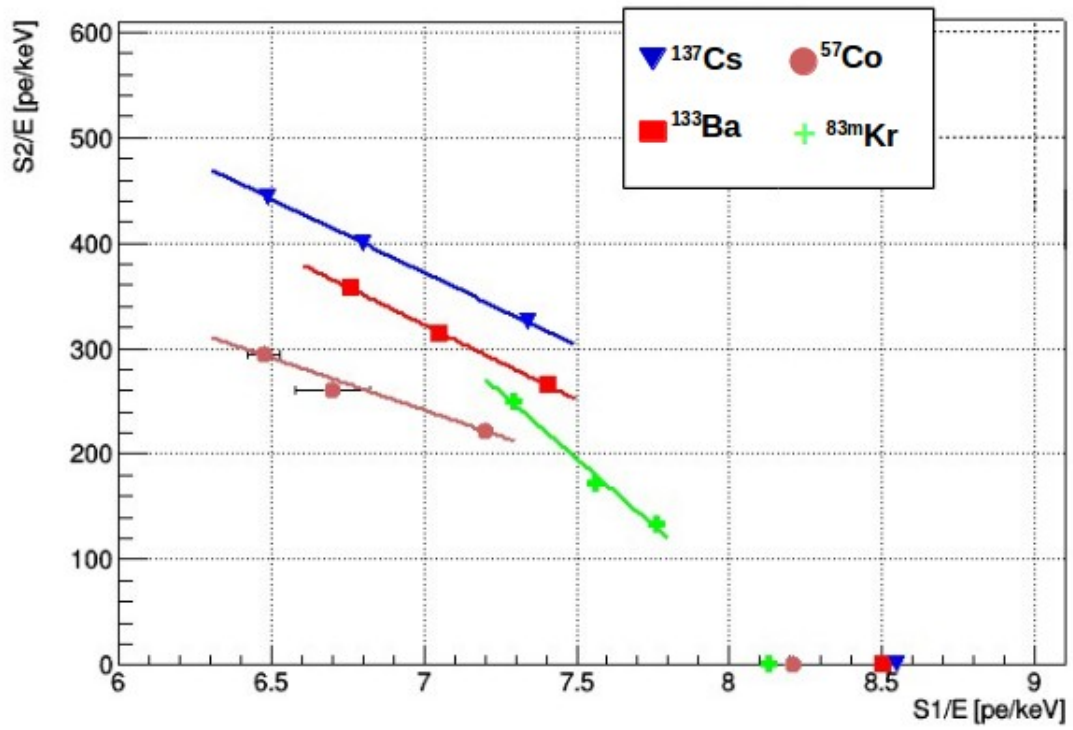
Figure 6.8: Doke plot with all sources and all drift fields. Data at null field are also shown, but they are not included in the fit.

CHAPTER 7
^{39}AR BETA SPECTRUM

In the early days of DarkSide-50, the TPC was filled with atmospheric argon while waiting for underground argon to be purified. The main drawback of using atmospheric argon is the presence of ^{39}Ar with an activity of 1 Bq/kg. However, the presence of ^{39}Ar provides a unique opportunity to investigate it's beta spectrum which has not been studied in literature with experimental data. In the next section, a brief introduction to the theory of the beta spectrum is presented followed by fitting the ^{39}Ar data present in DarkSide-50 with the theoretical prediction from the beta spectrum.

7.1 Theory of β Decay

Following from [39], one begins with the statistical beta spectrum derived from energy-momentum conservation. Suppose there is a nucleus at rest that then decays into three parts: an electron, an anti-neutrino, and the remaining nucleus. The total momentum must be converted. Thus:

$$0 = \vec{P} + \vec{p} + \vec{q} \tag{7.1}$$

where $\vec{P}$ is the recoil momentum of the nucleus and $\vec{p}$ and $\vec{q}$ are the momenta for the electron and the anti-neutrino, respectively. We assume that the electron and anti-neutrino share their energy 'statistically' and therefore can define $d\lambda/\lambda$ as the fraction of decays in which momenta in the ranges $d\vec{p}$, $d\vec{q}$ are attained:

$$\frac{d\lambda}{\lambda} = \frac{d\vec{p}d\vec{q}}{\iint d\vec{p}d\vec{q}} \tag{7.2}$$

After a change of coordinates and integrating over all neutrino and electron directions, one obtains

$$\frac{d\lambda}{\lambda} = \frac{qKp^2dp}{\int_0^{p0} qKp^2dp} \tag{7.3}$$

where p_0 is the maximum electron momentum attained when the neutrino has vanishing momentum and K (the neutrino energy)$\rightarrow \mu c^2$. Following another change in variable, p dp = W dW, the fraction of decays $d\lambda/\lambda$ in which electron energy is attained in the range dW is:

$$\frac{d\lambda}{dW} = \frac{\lambda}{f_0} W \sqrt{W^2 - m^2c^4}(W_0 - W)\sqrt{(W_0 - W)^2 - \mu^2c^4}/(mc^2)^5 \tag{7.4}$$

where W is the total energy of the electron, W_0 is the end-point energy of the electron, m is the rest mass of the electron, μ is the rest mass of the neutrino and f_0 is the dimensionless integral from

68

Eq. 7.3. However, due to the charge carried by the electron and the nucleus, one must consider the Coulomb force due to the positive charge on the nucleus which affects the energy distribution. Consider the spatial density $|\Psi_c|^2$ of electrons in motion, in which the electron emerges at a point r = 0 with nuclear charge, +Ze and attains a final momentum only outside of the range of the electrostatic force at r = ∞. Compare this with a free particle density $|\Psi_0|^2$ in a state in which the momentum exists unchanged. Now, assume that the electron waves are excited in proportion to the density at the nucleus and we can define the electron density ratio F(Z,W) = $|\Psi_c(0)/\Psi_0|^2$. F(Z,W) represents the correction to the statistical distribution due to the electrostatic force and the finite size of the nucleus. Therefore, one can rewrite Eq. 7.4 as (also setting μ to zero)

$$\frac{d\lambda}{dW} = (\lambda/f_0)\, W(W_0 - W)^2 \sqrt{W^2 - m^2c^4} F(Z,W)/(mc^2)^5 \tag{7.5}$$

To take into account relativistic effects, one can use solution of Dirac equation for F(Z,W) giving

$$F(Z,W) = 2(1 + \gamma_0)(2pR/\hbar)^{-2(1-\gamma_0)} e^{\pi\nu} \frac{|\Gamma(\gamma_0 + i\nu)|^2}{(\Gamma(2\gamma_0 + 1))^2} \tag{7.6}$$

where $\gamma_0 = \sqrt{1 - (\alpha Z)^2}$ and R is the radius at which Ψ_c is evaluated. In the low Z approximation, $(\alpha Z)^2 \ll 1, \gamma_0 \approx 1$. Then $|\Gamma(\gamma_0 + i\nu)|^2| \to |\Gamma(1 + i\nu)|^2 = (i\nu)!(-i\nu)! = \pi\nu/\sinh(\pi\nu)$ and $\nu = \alpha Z$. That simplifies the Fermi correction to

$$F(Z,W) = \frac{\pi\alpha Z e^{\pi\alpha Z}}{\sinh(\pi\alpha Z)}. \tag{7.7}$$

One must consider the correction due to the forbiddeness of the decay, S($\pm$Z,W). The explicit form of the correction due to the forbiddeness of the decay (hereafter known as the shape factor) can be found in [40]. For ^{39}Ar, we can use the low Z approximation such that the shape factor becomes

$$S(Z,W) = p_e^2 + (W_0 - W)^2 \tag{7.8}$$

where p_e is the electron momentum. The full beta spectrum can then be represented in three parts: the statistical spectrum, the Fermi correction and the shape factor:

$$d\lambda = A\lambda W(W_0 - W)^2 \sqrt{W^2 - m^2c^4} F(Z,W) S(\pm Z,W) dW \tag{7.9}$$

where A is an overall constant/amplitude encompassing the dimensionless integral f_0 and λ is the decay constant.

7.2 ^{39}Ar Fit

In order to fit the ^{39}Ar spectrum, we needed substitutions to Eq. 7.9. Namely, for ease of reading W_0, the end-point energy, becomes Q and $W = T + m$ where T is the kinetic energy. We also introduce two free parameters a and b. The fit of the ^{39}Ar beta spectrum for DarkSide-50 is given as the

$$\text{forbidden spectrum(T,a,b)} \cdot \text{detector resolution(T, light yield, fano factor)}$$

where the

$$\text{forbidden spectrum(T,a,b)} = \text{statistical(T)} \cdot \text{Fermi Correction} \cdot \text{shape factor(T,a,b)}.$$

The three pieces of the beta spectrum for the fit are then written as

$$\text{Statistical} = A\lambda(Q - T - m)^2\sqrt{(T + m)^2 - m^2}(T + m)$$
$$\text{Fermi Correction} = \frac{\pi\alpha Z e^{\pi\alpha Z}}{\sinh\pi\alpha Z} \tag{7.10}$$
$$\text{Shape Factor} = a\left[(T + m)^2 - m^2\right] + b(Q - T - m)^2$$

and the detector resolution is a gaussian function of the form

$$\text{detector resolution} = \frac{e^{-(npe-T)^2/2\sigma^2}}{\sigma\sqrt{2\pi}} \tag{7.11}$$

where npe = energy $\cdot$ light yield and σ = fano factor $\cdot \sqrt{npe}$.

The data used for the fit were taken during the calibration campaign in October/November 2014 with the 200 V/cm drift field and with null field. This data was taken during the time when DarkSide-50 was filled with atmospheric argon therefore containing a large statistical sample of ^{39}Ar β decay events. A statistical background subtraction was done using data taken after DarkSide-50 had been filled with underground argon (argon depleted in ^{39}Ar, 1400 times smaller ^{39}Ar decay rate). The results are found in Figures 7.1 and 7.2.

The fano factor for each drift field is the same within statistical errors. However, the light yield differs between the two drift fields as expected. The light yield at null field, 8.316 ± 0.002, is on par with what other calibration points have shown, such as Krypton (see [26]), at 8.3pe/keV. The theoretical beta spectrum (from the fit) agrees well with the ^{39}Ar data obtained from DarkSide-50 at higher energies (above ~ 250 keV), while it underestimates what the data shows at lower energies. This discrepancy could be attributed to some time varying background present during atmospheric argon running while being absent during underground argon runs taken later and used for statistical background subtraction. Another possibility may be variation in the detector response at low energies (below ~ 37 keV) not accounted for with the fit. The source of this
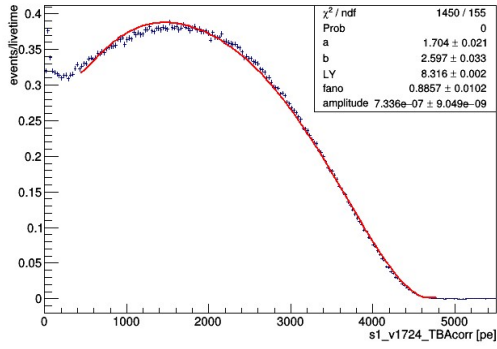
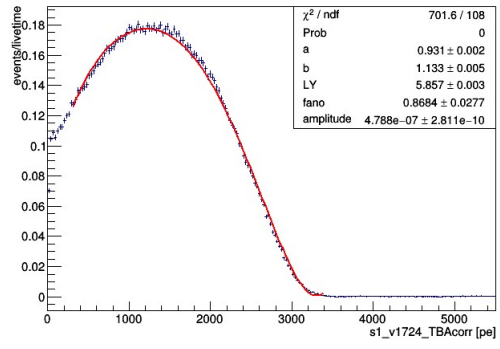Figure 7.1: ^{39}Ar spectrum at null field.

Figure 7.2: ^{39}Ar spectrum at 200 V/cm.

discrepancy is still under investigation.

CHAPTER 8
ENERGY SPECTRA

Utilizing the global energy variable developed in Ch. 6, one can take the average ϵ_1 and ϵ_2 values, Equations 6.13 and 6.14, and define the global energy variable as

$$E = \frac{W}{1+f} \left[\frac{S1}{0.179} + \frac{S2}{27.73} \right].$$
(8.1)

Then, one can plot the energy spectra for the various sources used for calibration. For all drift fields, for each source, the energy was calculated according to Eq. 8.1, where S1 and S2 were directly input from the data with their respective corrections. The results can be found in Fig. 8.1. The spectra for each drift field line up as expected from the model. The dashed line in each plot represents the position of the true source energy. From the plots, it is seen that the position of the true source energy is slightly off from the center of each peak: for ^{83m}Kr there is an 8% shift to lower energy, for ^{57}Co there is an 3.3% and 4.4% shift towards lower energy for the 122 keV and 136 keV γs respectively, and for ^{137}Cs there is a 2.7% shift to higher energy. This is an indicator that the Doke model is a good first approximation, but requires further refinement to reproduce the DarkSide-50 data in detail.

An energy spectrum was calculated for the ^{39}Ar beta spectrum as an independent check on the global energy variable. Since the ϵ_1 and ϵ_2 in the global energy variable were derived from the use of the calibration sources, ^{39}Ar offered a way to test the goodness of the global energy variable and also the fit of the beta spectrum. The detector resolution part of the fit of the energy spectrum for ^{39}Ar was modified such that Eq. 7.11 became

$$\text{detector resolution} = \frac{e^{-(energy-T)^2/2\sigma^2}}{\sigma\sqrt{2\pi}}$$
(8.2)

where σ = fano factor $\cdot \sqrt{npe}$ and npe = energy·light yield. The small change takes into account the fact that we are now fitting an energy spectrum instead of an S1 spectrum. S1 and S2 were taken from atmospheric argon data taken at 200 V/cm. Fig. 8.2a shows the results of the energy calculation and the fit when using the averaged ϵ_1, ϵ_2 from all of the calibration sources. Figures 8.2b, 8.2c, 8.2d show the results of the energy calculation and fit of the ^{39}Ar spectrum when using different combinations of the ϵ_1 and ϵ_2 values. The combinations of the ϵ values are, respectively: averaged $\epsilon_{1,2}$ for all sources, averaged ϵ_1, ϵ_2 values from ^{83m}Kr only, averaged $\epsilon_{1,2}$ for ^{133}Ba and ^{137}Cs only, and averaged ϵ_1, ϵ_2 values for the three external sources only. Table 8.1 summarizes the fit parameters. Overall, the energy spectrum shape matches that of the ^{39}Ar S1 spectrum, but with deficiencies. At low energy, the fit becomes unreliable and underestimates the energy seen in the detector. This effect at low energy can also be seen in Figures 7.1 and 7.2; the choice of the
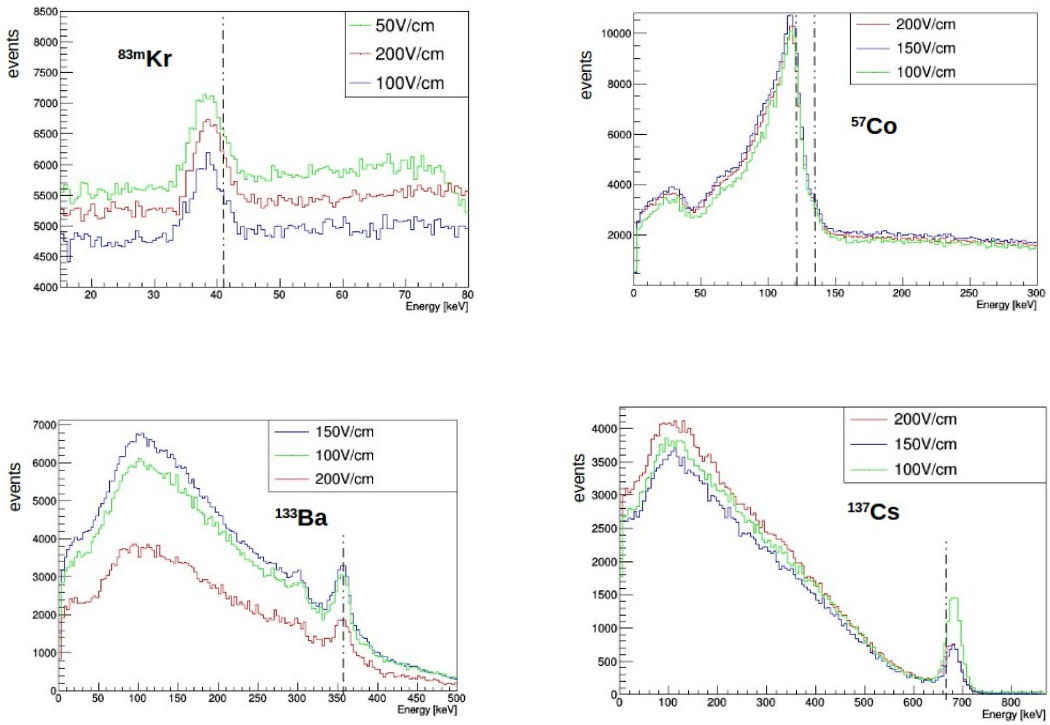
Figure 8.1: Energy spectra of all calibration sources at different drift fields. The dashed line represents the source energy of each source.

ϵ_1,ϵ_2 values used	a	b	Light Yield [pe/keV]	fano factor
^{83m}Kr	0.915 ± 0.02	1.66 ± 0.03	2.8 ± 0.5	0.18 ± 0.02
^{133}Ba,^{137}Cs	0.93 ± 0.02	1.59 ± 0.03	4 ± 1	0.74 ± 0.09
^{57}Co, ^{133}Ba, ^{137}Cs	0.97 ± 0.02	1.46 ± 0.03	5.5 ± 0.7	0.93 ± 0.06
All Sources	0.93 ± 0.02	1.59 ± 0.03	4.4 ± 1.2	0.68 ± 0.09

Table 8.1: Summary of the parameters extracted from the fit of the ^{39}Ar energy spectrum when using different combinations of ϵ_1 and ϵ_2 values.

low bound of the fit is very sensitive to the goodness of the fit. If the low bound on the fit is set too low (below ~ 300 pe for S1 spectra and below 10 keV for energy spectra or above 20 keV for energy spectra), then the fit will not converge. The parameters a, b, and fano factor for the fit of ^{39}Ar energy spectrum are comparable to those found with the fitted S1 spectrum at 200 V/cm. The light yield extracted from the fit, 4.4 ± 1.2 pe/keV, is lower than expected but still comparable with that extracted from the fitted S1 spectrum at 200 V/cm, 5.857 ± 0.003 pe/keV. Both light yields at 200 V/cm are lower than that taken from the null field fit, 8.316 ± 0.002 pe/keV, however, this is expected since electrons escape from recombining when a drift field is applied which lowers the expected energy. When comparing the ^{39}Ar fitted energy spectra, the light yields from the combination of ϵs for ^{133}Ba/^{137}Cs, ^{57}Co/^{133}Ba/^{137}Cs, and from all four sources agree within 1σ. When ϵ_1 and ϵ_2 from ^{83m}Kr are solely used in the energy variable calculation, the light yield and fano factors are severely underestimated when compared to the other ϵ combinations. From this, the global energy variable shows a greater accuracy in predicting the energy values when the full complement of sources (which span the electron recoil energy range) are used. The energy variable developed shows good predictive power for the light yield and energy in the higher range (above ~ 300 keV), while it underestimates the energy at the low (below ~ 70 keV) end of the spectrum. This trend is also observed when reconstructing the energy spectra for the calibration sources where ^{83m}Kr shows the biggest shift in energy from the true source energy at 8%, towards lower energy, while the higher energy sources' energy shift is less.
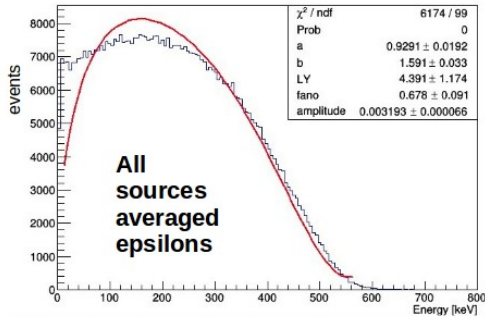
(a) Energy spectrum calculated from the global energy variable for ^{39}Ar at 200 V/cm using the average of ϵ_1 and ϵ_2 from all the sources.
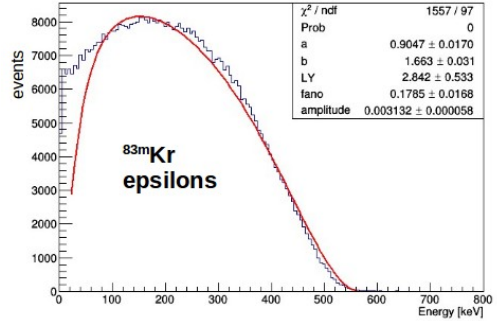
(b) ^{39}Ar energy spectrum calculated with the global energy variable at 200 V/cm using the average of the ^{83m}Kr ϵ_1 and ϵ_2 only.
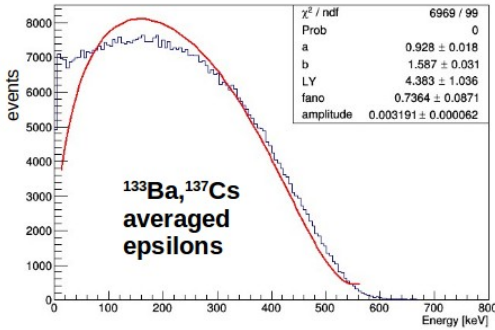
(c) ^{39}Ar energy spectrum calculated with the global energy variable at 200 V/cm using the average of the ^{133}Ba and ^{137}Cs ϵ_1 and ϵ_2.
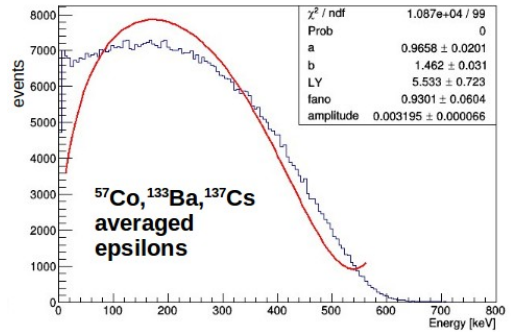
(d) ^{39}Ar energy spectrum calculated with the global energy variable at 200 V/cm using the average of the ^{57}Co, ^{133}Ba, and ^{137}Cs ϵ_1 and ϵ_2.

CHAPTER 9
DARKSIDE CURRENT STATUS

DarkSide-50 is currently taking data and focusing on a blind analysis. The results of the blind analysis will be published in the coming months. The blind analysis will benefit from improved nuclear recoil calibrations as well as a better understanding of the intrinsic backgrounds and detector response. The analysis has been planned to include 3 live years of WIMP search data allowing it to achieve an order of magnitude greater sensitivity.

9.1 DarkSide-20k

The next step in the DarkSide program is DarkSide-20k. DarkSide-20k will build on the foundation of DarkSide-50; it will be a 30 tonne (20 tonne fiducial) liquid argon TPC inside an active veto system modeled after DarkSide-50. All components of the detector are being designed for ultra-low backgrounds; they must be made from materials of the highest radiopurity. Included in the development of detector components is the switch from traditional PMTs to silicon photomultipliers (SiPMs). The SiPMs give a higher effective quantum efficiency, a greater reliability for use at low temperatures, and higher radiopurity than PMTs. The TPC cryostat will be constructed of ultra-low radioactivity titanium rather than the stainless steel used in DarkSide-50. It will be filled with depleted argon (DAr). Although the level of ^{39}Ar in UAr was significantly reduced (1400 times lower, [35]) relative to AAr, for the exposure planned for DarkSide-20k the argon will need to be further purified. In order to obtain the quantity and purification needed for DarkSide-20k, dedicated operations have been initiated and are described in the following section.

9.1.1 Urania and Aria

The Urania project is designed to procure the amount of UAr needed for DarkSide-20k in a timely fashion given that it took six years to produce the 155 kg needed for DarkSide-50. The first step in obtaining the required 30 tonnes of DAr is to increase the production rate of UAr. UAr will be obtained from the Kinder Morgan Doe Canyon facility in Cortez, CO at production rate of 100 kg/day.

Urania was founded thanks to the strong relationship established between the DarkSide Collaboration and the Kinder Morgan and Air Products corporations. The relationship was developed after the DarkSide Collaboration provided Kinder Morgan with a gas analysis of the UAr and it was found to contain helium. The relationship with Air Products was established to allow them to extract the helium. 6% of the gas stream returned to Kinder Morgan by Air Products after helium extraction is fed to the Urania plant for DarkSide. This gas stream has two significant advantages
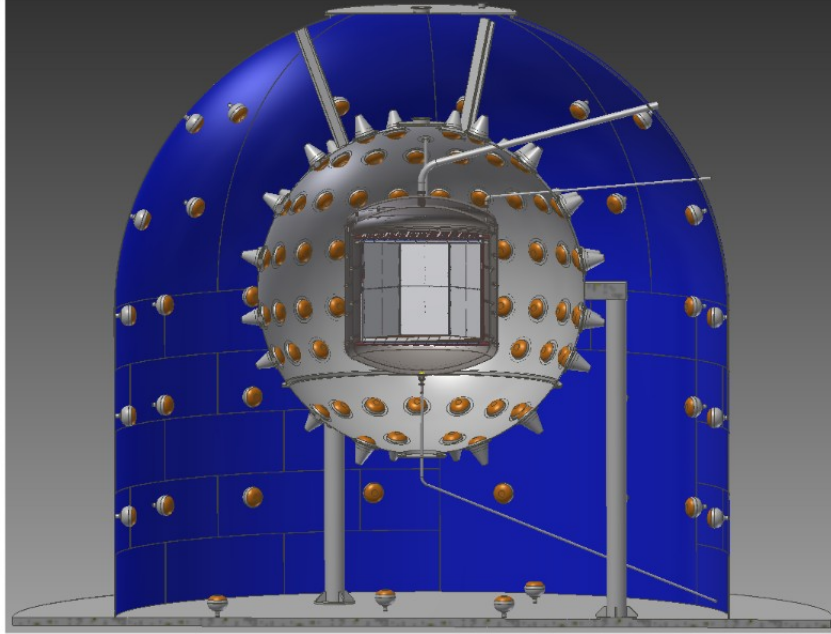
Figure 9.1: Cross-section of DarkSide-20k with the cryostat in the center surrounded by the LSV and WCV similar to those from DarkSide-50.

over the gas used for DarkSide-50: (1) the gas is devoid of any traces of water vapor and (2) there are only trace amounts of helium left; these features simplify the process of UAr extraction by the Urania plant. From the Urania plant at Kinder Morgan, the extracted UAr will be shipped to the Aria project in Sardinia, Italy.

The Aria project is designed to chemically purify the UAr for use in LAr detectors. It consists of two 350 m tall cryogenic distillation columns constructed in underground shafts at the Seruci mine campus of CarboSulcis, a mining company owned by the Regione Autonoma della Sardegna. Construction of the first distillation column began in September 2015. The distillation columns will be able to process UAr at a rate of order 1 t/day while removing traces of chemical impurities such as N_2, O_2, and Kr with a separation power of 10^3 per pass. Each pass of UAr through the columns is expected to reduce ^{39}Ar by a factor of ten [41].

With an exposure of 100 t yr, DarkSide-20k will be able to search for WIMPs in the energy range 30 keV$_{nr}$ to 200 keV$_{nr}$ (with WIMP mass in the tens of GeV/c^2 to hundreds of TeV/c^2) and will obtain a sensitivity of 10^{-47} cm^2 for a WIMP mass of 100 GeV/c^2 [41]. The final step for the DarkSide program will be in the form of Argo, a 200 tonne DAr TPC which will reach a sensitivity of 10^{-48} cm^2 (see Fig. 9.2). Beyond that level is the limit imposed by coherent neutrino-nucleus scattering, an irreducible background, which means that a background free WIMP search may not be possible.
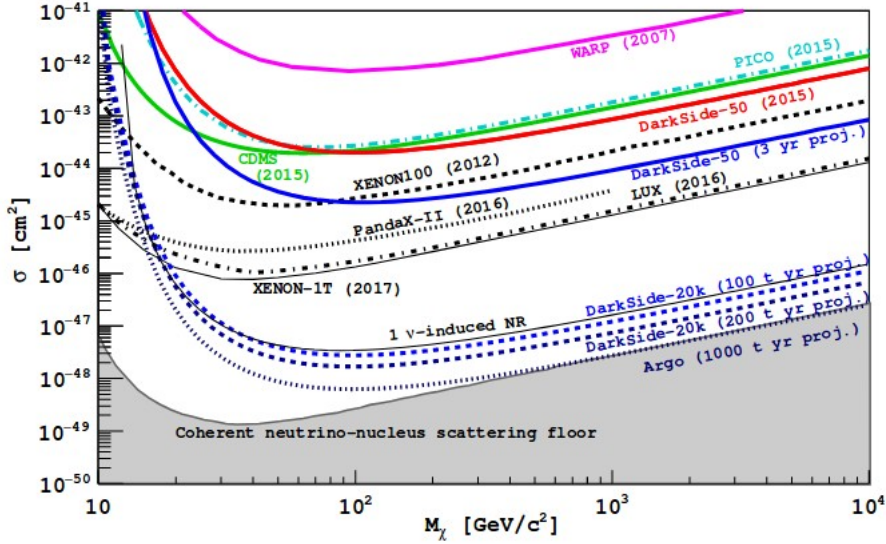
Figure 9.2: Current results of Dark Matter experiments with the projected sensitivities from DarkSide-50 (3 live years), DarkSide-20k, and Argo [41].

9.2 Conclusions

This work presents CALIS, a system for inserting calibration sources near the TPC, from its design and testing to its installation and commissioning. CALIS has been used successfully in numerous calibration campaigns for both the TPC and the LSV. Using the data from the campaigns, the response of the detector to electron recoils has been thoroughly investigated. Light yield measurements have been obtained from the various sources showing a 5% variation across an energy range from 40 keV to 665 keV. The development of the global energy variable has provided a way for the energy response of the detector to be calculated regardless of drift field and independent of the event being single-sited or a multiple scatter. The Doke model, from which the global energy variable is derived, is a good first approximation of DarkSide-50's energy response; ongoing analysis of the recombination effects in LAr are being pursued in the DarkSide collaboration with the goal of better understanding the effects at null field and low energies. Also, the theoretical beta decay spectrum of ^{39}Ar has been tested by fitting ^{39}Ar decays in atmospheric argon data. The fit performed at null field and 200 V/cm shows excellent agreement above $\sim$300 keV, although further investigations at low energy are required to account for the excess of events observed in the lower energy range (below $\sim$70 keV). In the energy range between $\sim$70 keV and $\sim$300 keV, the fit overestimated the event energies. The most promising results in calculating event energy based on S1 and S2, come from using the full complement of calibration sources available to reconstruct the electron recoil event energy. The global energy variable yields a more accurate prediction of the energy scale in the DarkSide-50 TPC. An understanding of how the detector responds to a wide

range of event energies, especially those within the WIMP search region, will play an important role in the estimation of backgrounds for DarkSide-50 and in turn help in the identification of a WIMP signal, should one be detected.

APPENDIX A
VARYING THE SIGMA BOUNDS

Results of varying the $\pm\sigma$ bounds for other drift fields.
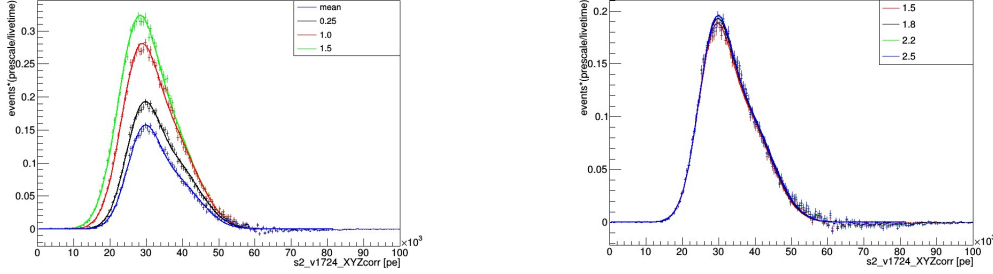
(a) ^{57}Co S2 at 150 V/cm with varied lower σ (b) ^{57}Co S2 at 150 V/cm with varied upper σ
bounds, upper bound constant at mean + 1.8σ. bounds, lower bound constant at mean - 0.25σ.

Figure A.1: ^{57}Co S2 at 150 V/cm with varied bounds. Lower bound variations: mean - 0.0σ, mean - 0.25σ, mean - 1.0σ, and mean - 1.5σ with upper bound kept constant at mean + 1.8σ. Upper bounds variations: mean + 1.5σ, mean + 1.8σ, mean + 2.2σ, and mean + 2.5σ with lower bound kept constant at mean - 0.25σ.

(a) ^{133}Ba S2 at 150 V/cm with varied $\pm\sigma$ bounds. (b) ^{137}Cs S2 at 150 V/cm with varied $\pm\sigma$ bounds.

Figure A.2: ^{133}Ba and ^{137}Cs S2 at 150 V/cm with varied bounds.

Source	$\pm0.5\sigma$	$\pm1.0\sigma$	$\pm1.5\sigma$	$\pm2.0\sigma$
^{133}Ba	113500 ± 200	113100 ± 200	111900 ± 200	111400 ± 200
^{137}Cs	268200 ± 700	265500 ± 600	264900 ± 500	263300 ± 500

Table A.1: Summary of ^{133}Ba and ^{137}Cs S2 means at 150 V/cm for the various S1 sigma bounds used to select S2 events.

(a) ^{57}Co S2 at 100 V/cm with varied lower σ bounds, upper bound constant at mean + 1.8σ.

(b) ^{57}Co S2 at 100 V/cm with varied upper σ bounds, lower bound constant at mean - 0.25σ.

Figure A.3: ^{57}Co S2 at 100 V/cm with varied bounds. Lower bound variations: mean - 0.0σ, mean - 0.25σ, mean - 1.0σ, and mean - 1.5σ with upper bound kept constant at mean + 1.8σ. Upper bounds variations: mean + 1.5σ, mean + 1.8σ, mean + 2.2σ, and mean + 2.5σ with lower bound kept constant at mean - 0.25σ.

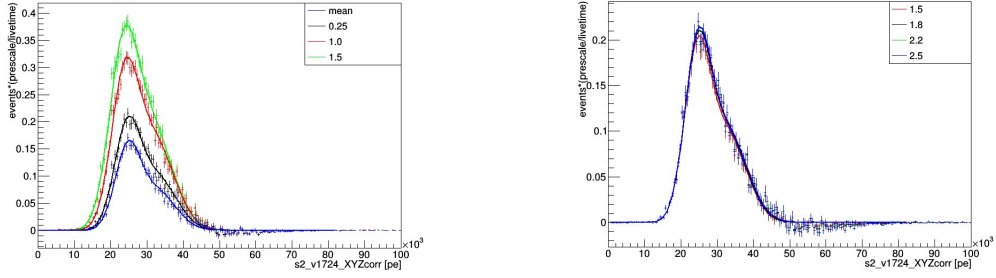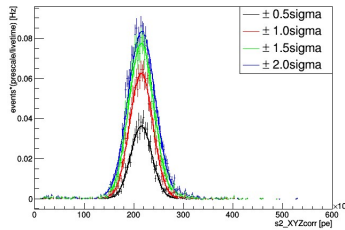(a) ^{83m}Kr S2 at 100 V/cm with varied $\pm\sigma$ bounds.

(b) ^{133}Ba S2 at 100 V/cm with varied $\pm\sigma$ bounds.

(c) ^{57}Cs S2 at 100 V/cm with varied $\pm\sigma$ bounds.

Figure A.4: ^{83m}Kr, ^{133}Ba, and ^{137}Cs fitted S2 distributions at 100 V/cm with varied $\pm\sigma$ bounds: $\pm$ 0.5 σ, $\pm$ 1.0σ, $\pm$ 1.5σ, and $\pm$ 2.0σ.
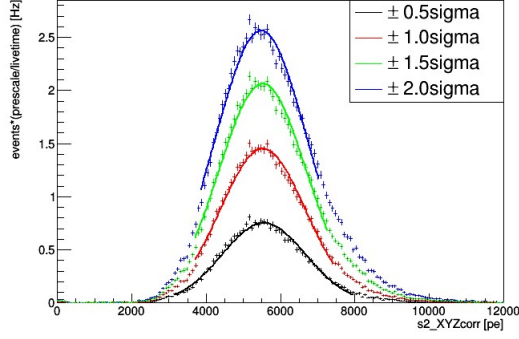
81

Figure A.5: $^{83\text{m}}$Kr at 50 V/cm with varied $\pm\sigma$ bounds: $\pm$ 0.5 σ, $\pm$ 1.0σ, $\pm$ 1.5σ, and $\pm$ 2.0σ.

Source	$\pm0.5\sigma$	$\pm1.0\sigma$	$\pm1.5\sigma$	$\pm2.0\sigma$
$^{83\text{m}}$Kr	7150 ± 10	7130 ± 10	7130 ± 10	7100 ± 10
^{133}Ba	95600 ± 300	95200 ± 300	94400 ± 300	93600 ± 300
^{137}Cs	215200 ± 400	215100 ± 300	21500 ± 300	215800 ± 300
$^{83\text{m}}$Kr @ 50 V/cm	5553 ± 7	5524 ± 6	5520 ± 5	5480 ± 6

Table A.2: Summary of $^{83\text{m}}$Kr, ^{133}Ba, and ^{137}Cs S2 means at 100 V/cm for the various S1 sigma bounds used to select S2 events. The last line is for $^{83\text{m}}$Kr at 50 V/cm.

APPENDIX B
DOKE PLOTS

Doke plots for other sources: ^{83m}Kr, ^{57}Co, and ^{137}Cs.
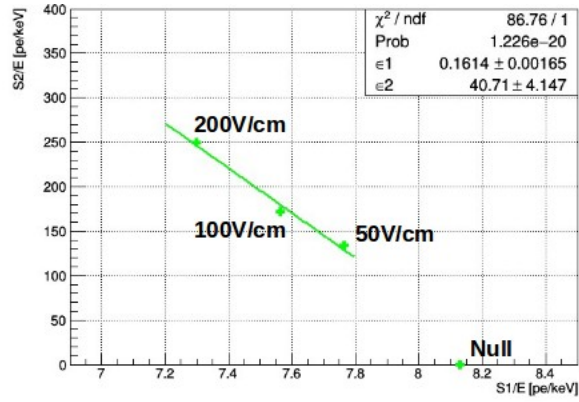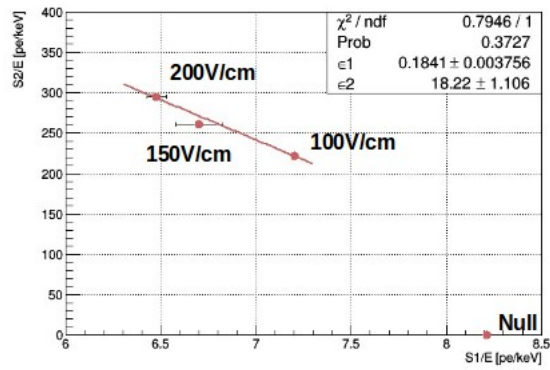

Figure B.1: Doke plot (S2/E vs S1/E) for ^{83m}Kr.

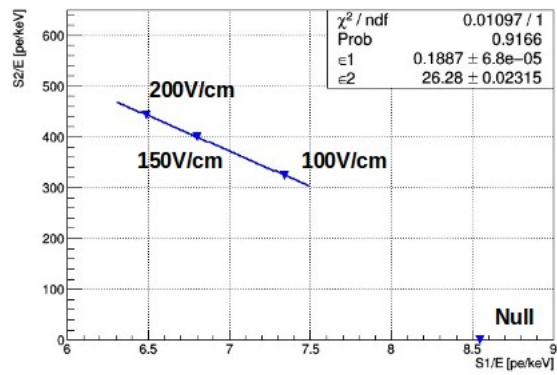Figure B.2: Doke plot (S2/E vs S1/E) for ^{57}Co.

Figure B.3: Doke plot (S2/E vs S1/E) for ^{137}Cs.

BIBLIOGRAPHY

[1] F. Zwicky. Die rotverschiebung von extragalaktischen nebeln. *Helv. Phys.*, Acta 6:110–127, 1933.

[2] D. Clowe et al. A direct empirical proof of the existence of dark matter. *The Astrophysical Journal Letters*, 648:109–113, September 2006.

[3] Vera C. Rubin, Jr. W. Kent Ford, and Norbert Thonnard. Rotational properties of 21 sc galaxies with a large range of luminosities and radii, from ngc 4605 (r = 4 kpc) to ugc 2885 (r = 122 kpc). *The Astrophysical Journal*, 238:471–487, June 1980.

[4] Vera C. Rubin and Jr. W. Kent Ford. Rotation of the andromeda nebula from a spectroscopic survey of emission regions. *The Astrophysical Journal*, 159, February 1970.

[5] H. Babcock. The rotation of the andromeda nebula. *Lick Observatory bulletin*, 49, 1939.

[6] G. Steigman. Primordial nucleosynthesis in the precision cosmology era. *Annual Review of Nuclear and Particle Science*, 57:463–471, December 2007.

[7] R. Cooke et al. Precision measures of the primordial abundance of deuterium. *The Astrophysical Journal*, 781, January 2014.

[8] P. Ade et al. (Planck Collaboration). Planck 2015 results. xiii cosmological parameters. *Astronomy and Astrophysics A*, June 2016.

[9] G. Bertone and D. Merritt. Dark matter dynamics and indirect detection. *Modern Physics Letters A*, 20:1021–1036, 2005.

[10] Jonathan L. Feng. Dark matter candidates from particle physics and methods of detection. *Annual Review of Astronomy and Astrophysics*, 48(1):495–545, 2010.

[11] G. Bertone, D. Hooper, and J. Silk. Particle dark matter: evidence, candidates and constraints. *Physics Reports*, 405:279–390, 2005.

[12] L. Baudis. Wimp dark matter direct-detection searches in noble gases. *Physics of the Dark Universe*, 4:50–59, 2014.

[13] M.C. Smith et al. The rave survey: Constraining the local galactic escape speed. *Mon. Not. Roy. Astrom. Soc.*, 379:755–772, 2007.

[14] T. Marrodn Undagoitia and L. Raunch. Dark matter direct-detection experiments. *Journal of Physics G: Nuclear and Particle Physics*, 43:013001, 2016.

[15] L. Baudis. Direct dark matter detection: The next decade. *Physics of the Dark Universe*, 1:94–108, 2012.

[16] R. Bernabei et al. Dama/libra results and perspectives. *Bled Workshops Phys.*, 17:1–7, 2016.

[17] R. Agnese et al. Search for low-mass weakly interacting massive particles with supercdms. *Phys. Rev. Lett.*, 112:241302, 2014.

[18] F. Petricca et al. New results on low-mass dark matter from the cresst-ii experiment. *Journal of Physics: Conference Series*, 718:042044, 2016.

[19] Barbosa de Souza et al. First search for a dark matter annual modulation signal with nai(tl) in the southern hemisphere by dm-ice17. *Phys. Rev. D*, 95:032006, February 2017.

[20] E. et al. (XENON Collaboration) Aprile. First dark matter search results from the xenon1t experiment. *Phys. Rev. Lett.*, 119:181301, Oct 2017.

[21] Alex Wright. The darkside program at lngs. 2011.

[22] T. Alexander et al. Light yield in darkside-10: a prototype two-phase argon tpc for dark matter searches. *Astroparticle Physics*, 49:44–51, September 2013.

[23] P. Agnes et al. (DarkSide Collaboration). The veto system of the darkside-50 experiment. *Journal of Instrumentation*, 11, March 2016.

[24] G. Bellini et al. Cosmic-muon flux and annual modulation in borexino at 3800 m water-equivalent depth. *JCAP*, 2012, May 2012.

[25] Alex Wright, Pablo Mosteiro, Ben Loer, and Frank Calaprice. A highly efficient neutron veto for dark matter experiments. *NIM*, 644:18–26, July 2011.

[26] P. Agnes et al. (DarkSide Collaboration). First results from the darkside-50 dark matter experiment at laboratori nazionali del gran sasso. *Physics Letters B*, 743:456–466, 2015.

[27] T. Doke et al. Let dependence of scintillation yields in liquid argon. *Nuclear Instruments and Methods in Physics Research*, A269:291–296, 1988.

[28] T. Doke et al. Absolute scintillation yields in liquid argon and xenon for various particles. *Japanese Journal of Applied Physics*, 41:1538–1545, 2002.

[29] Tadayoshi Doke, Kimiaki Masuda, and Eido Shibamura. Estimation of absolute photon yields in liquid argon and xenon for relativistic (1 mev) electrons. *Nuclear Instruments and Methods of Physics Research*, A291:617–620, 1990.

[30] M. Miyajima, T. Takahashi, S. Konno, T. Hamada, S. Kubota, H. Shibamura, and T. Doke. Average energy expended per ion pair in liquid argon. *Physical Review A*, 9, March 1974.

[31] A. Hitachi, T. Takahashi, N. Funayama, K. Masuda, J. Kikuchi, and T. Doke. Effect of ionization density on the time dependence of luminescence from liquid argon and xenon. *Physical Review B*, 27, May 1983.

[32] D. Gastler, E. Kearns, A. Hime, L.C. Stonehill, S. Seibert, J. Klein, W.H. Lippincott, D.N. McKinsey, and J.A. Nikkel. Measurement of scintiallation efficiency for nuclear recoils in liquid argon. *Physical Review C*, 85, June 2012.

[33] H.H. Loosli. A dating method with ^{39}ar. *Earth and Planetary Science Letters*, 63:51–62, April 1983.

[34] J. Xu et al. A study of the trace ^{39}ar content in argon from deep underground sources. *Astroparticle Physics*, 66:53–60, 2015.

[35] P. Agnes et al. (DarkSide collaboration). Results from the first use of low radioactivity argon in a dark matter search. *Phys. Rev. D*, 93, April 2016.

[36] Erin Edkins Ludert. Detailed characterization of nuclear recoil pulse shape discrimination in the darkside-50 direct dark matter experiment. 2017.

[37] P. Agnes et al. The Electronics, Trigger and Data Acquisition System for the Liquid Argon Time Projection Chamber of the DarkSide-50 Search for Dark Matter. 2017.

[38] Masayuki Wada. Update on energy variable. *DocDB. 2045*, June 2017.

[39] E.J. Konopinski. *The Theory of Beta Radioactivity*. Clarendon Press, Oxford, 1966.

[40] G. Keefer and A. Piepke. Beta spectra for ^{39}ar, ^{85}kr, and ^{210}bi. *University of Alabama, Tuscaloosa*, 2004.

[41] C. E. Aalseth et al. DarkSide-20k: A 20 Tonne Two-Phase LAr TPC for Direct Dark Matter Detection at LNGS. 2017.